Investigation of new generator technologies for offshore wind turbines

Mohammed Ali Benhamida

Normandie Université

THESE

Pour obtenir le diplôme de doctorat

Spécialité Génie Électrique

Préparée au sein du « Groupe de Recherche en Électrotechnique et Automatique du Havre (EA 3220)»

Investigation de nouvelles technologies de générateurs pour les éoliennes offshore

Présentée et soutenue par
Mohammed Ali BENHAMIDA

Thèse soutenue publiquement le 30/05/2018 devant le jury composé de		
M[me] / Christine DE JOUETTE	Ingénieur-docteur, EDF Energies Nouvelles	Encadrante
Mr / Noureddine TAKORABET	Professeur des universités, Université de Lorraine	Rapporteur
M[me] / Elena LOMONOVA	Professeur des universités, Université d'Eindhoven	Rapporteur
Mr / Jean Claude VANNIER	Professeur des universités, SUPELEC, Paris Sud	Examinateur
Mr / Boumedyene NEDJAR	Ingénieur-docteur, Adwen France SAS	Encadrant
Mr / Georges BARAKAT	Professeur des universités, Université du Havre	Directeur de thèse
Mr / Yacine AMARA	Professeur des universités, Université du Havre	Examinateur

Thèse dirigée par Georges BARAKAT, laboratoire GREAH

UNIVERSITÉ LE HAVRE

ED PSIME

GREAH

Acknowledgment

The work presented in this thesis was carried out at the research group in electrical engineering of Le Havre (GREAH) at Le Havre university and at Adwenoffshore France an offshore wind turbine manufacturer and supplier. It has been funded by Adwenoffshore and the National Association of Research and Technology (ANRT) under the convention number 2014/0750.

I want to express my gratitude to Prof. Jean Claude VANNIER, professor at supelec, Paris Sud university, who accepted to examine this work and to chair the thesis jury. I am also very honored that Prof. Elena LOMONOVA, professor at the University of Eindhoven, and Prof. Noureddine TAKORABET, professor at the university of Lorraine, for examining my work and being in the thesis jury. I would also like to thank Dr. Christine DE JOUETTE, marine energies project director at EDF Energies Nouvelles, Dr. Boumedyene NEDJAR electrical Engineer at Adwenoffshore and Prof. Yacine AMARA for being in the thesis jury.

I would like to express my sincere gratitude to my advisor Prof. BARAKAT for the continuous support of my Ph.D study and related research, for his patience, motivation, and immense knowledge. His guidance helped me in all the time of research and writing of this thesis. I could not have imagined having a better advisor and mentor for my Ph.D study.

Besides my advisor, I would like to thank the rest of my thesis committee: Prof. AMARA, Dr. NEDJAR, Dr. DEGLAIRE and Dr. DEJOUETTE, for their insightful comments and encouragement, but also for the hard question which encouraged me to widen my research from various perspectives.

I thank my fellow labmates, company colleagues and friends for the stimulating discussions for the sleepless nights we were working together before deadlines, and for all the fun we have had in the last four years. In particular, I am grateful to Adel, Mouheb, Hamza, Amina, Habiba, Nabih and espacially Athena.

Last but not the least, I would like to thank my family for supporting me throughout writing this thesis and my life in general.

Contents

Contents iii

List of Figures v

List of Tables ix

General Introduction . . . 1

1 Stat of the art: offshore wind turbine generator 3

Introduction . . . 3

1.1 Renewable energy as an alternative Energy . . . 3

1.2 Overview on the global wind power . . . 5

1.3 Onshore and offshore wind turbines . . . 8

1.4 Manufactures of wind turbines . . . 9

1.5 Wind turbine technology . . . 11

1.6 Electrical machines used in indirect drive train . . . 12

1.6.1 Asynchronous generator . . . 13

1.6.1.1 Squirrel cage asynchronous generator . . . 13

1.6.1.2 Wound rotor asynchronous generator . . . 14

1.7 Electrical machines used in direct drive train . . . 14

1.7.1 Synchronous machines . . . 15

1.7.1.1 Wound rotor synchronous machine . . . 16

1.7.1.2 Permanent magnet synchronous machine . . . 16

1.8 Toward large wind turbines . . . 18

1.9 Problematic . . . 21

Conclusion . . . 21

2 Multi-physics modeling of electrical machines 23

Introduction . . . 23

2.1 Magnetic modeling of electrical machines . . . 25

2.2 Taking into consideration the non-linearity of soft magnetic materials . . . 27

2.2.1 Electromagnetic torque computation . . . 30

2.3 Thermal modeling of electrical machines . . . 30

2.3.1 Convection heat coefficient computation . . . 33

2.3.2 Slot's equivalent conduction coefficient . . . 36

2.4 Non-linear thermal behavior of copper . . . 37

2.5 Air-gap modeling . . . 38

2.6 Model validation . . . 43

2.6.1 Magnetic model validation . . . 43

2.6.2 Machine A results . . . 44
2.6.3 Machine B results . . . 45
2.6.4 Thermal model validation . . . 47
Conclusion . . . 49

3 Optimal design of the studied structures 51
Introduction . . . 51
3.1 General mathematical definitions . . . 51
3.2 Benchmark functions for optimization algorithm . . . 53
3.3 Type of optimization algorithms . . . 54
3.3.1 Deterministic optimization algorithm . . . 54
3.3.2 Stochastic algorithms . . . 54
3.3.2.1 Particle swarm PSO . . . 54
3.3.2.2 Genetic algorithms GA . . . 55
3.4 Multi-objectives constrained optimization . . . 57
3.4.1 Transformation of the problem into mono-objective . . . 57
3.4.2 Pareto-based approaches . . . 58
3.5 Solving the constrained problem . . . 58
3.6 Previous work on electrical machine optimization . . . 58
3.7 Results and discussion . . . 61
3.7.1 Simulation and results for the concentrated flux machine . . . 63
3.7.1.1 15 MW optimization results . . . 65
3.7.1.2 8 MW optimization results . . . 67
3.7.1.3 5 MW optimization results . . . 70
3.7.2 Simulation and results for the surface mounted permanent magnet machine . . . 72
3.7.2.1 15 MW optimization results . . . 74
3.7.2.2 8 MW optimization results . . . 76
3.7.2.3 5 MW optimization results . . . 79
Conslusion . . . 82

4 Magnetically geared or direct drive topology ? 83
Introduction . . . 83
4.1 Mechanical gears used in wind energy : generalities . . . 83
4.2 Magnetic gears . . . 85
4.3 Simulation and results discussion . . . 88
4.3.1 Magnetic gear . . . 88
4.3.2 Direct drive topology . . . 95
Conslusion . . . 107
General Conclusion . . . 108

A Scientific papers 109

Bibliography 111

List of Figures

1.1 Overall share of renewable energy [9] . . . 4
1.2 Levelised Cost of electricity 2010-2016 [9] . . . 4
1.3 Cumulative power capacity in the European Union by technology 2005-2016[14] . . . 5
1.4 annual new installed capacity by region from 2008 to 2016 Global [13] . . . 5
1.5 Approximate Incremental Wind Penetration [15] . . . 6
1.6 Trends in Renewable Energy in the European Union[14] . . . 7
1.7 Electricity production from wind power [14] . . . 8
1.8 The global offshore wind capacity in 2015 and 2015 by region . . . 9
1.9 Wind turbine manufactures capacity [20] . . . 10
1.10 Offshore wind turbine manufactures capacity [21] . . . 11
1.11 Geared topology . . . 12
1.12 Planetary helical gearbox . . . 13
1.13 Direct drive topology[29] . . . 14
1.14 Enercon E126 wind turbine concept[29] . . . 15
1.15 Segmented generator concept by Siemens [31] . . . 15
1.16 Synchronous generator . . . 17
1.17 Different topologies of permanent synchronous machine . . . 17
1.18 Cumulative number of offshore wind turbine by size [42] . . . 18
1.19 Average offshore wind turbine rated capacity [MW] [21] . . . 18
1.20 top five suppliers by MW of wind turbines greater than 5 Mw in 2016 [21] 19

2.1 Accuracy and computation time dependency on the modeling method . . . 24
2.2 Representation of an elementary block . . . 25
2.3 Equivalent reluctant circuit of a magnet . . . 25
2.4 Illustration of flux tube . . . 26
2.5 M330-30A B(H) characteristics . . . 28
2.6 Algorithm's simplified diagram . . . 29
2.7 Illustration of thermal flux tube . . . 31
2.8 Representation of an elementary block for transient thermal computation . 31
2.9 Nusselt number dependency on Taylor modified number . . . 35
2.10 A way to represent the slot for thermal computation . . . 36
2.11 Copper resistivity dependency on the temperature . . . 37
2.12 Algorithm's simplified diagram for thermal computation . . . 38
2.13 Scalar potential interpolation in the sliding surface . . . 41
2.14 Flux density interpolation in the sliding surface . . . 42
2.15 Studied machine for magnetic model validation . . . 43
2.16 Flux through the phases at no-load . . . 44

2.17 Magnetic flux densities comparison . . . 44
2.18 Electromagnetic torque . . . 44
2.19 Results obtained by reluctance network . . . 45
2.20 Magnetic flux densities comparison . . . 45
2.21 Electromagnetic torque . . . 46
2.22 Magnetic flux densities comparison . . . 46
2.23 Results obtained by reluctance network . . . 46
2.24 Supply circuit . . . 48
2.25 Material used fo measurment . . . 48
2.26 Temperature evolution through the time . . . 48

3.1 Example of local and global minima . . . 52
3.2 Example of optimization test function . . . 53
3.3 General scheme of genetic algorithms . . . 55
3.4 General scheme of optimization process . . . 62
3.5 View of concentrated flux machine and main geometric parameters . . . 64
3.6 Pareto optimality using NDFeB ($B_r = 1.2$[T]) . . . 65
3.7 Results validation (15MW) . . . 65
3.8 Optimized machines parameters . . . 67
3.9 Pareto optimality using NDFeB ($B_r = 1.2$[T]) . . . 67
3.10 Results validation (8MW) . . . 68
3.11 Optimized machines parameters . . . 69
3.12 Pareto optimality using NDFeB ($B_r = 1.2$[T]) . . . 70
3.13 Results validation (5MW) . . . 70
3.14 Optimized machines parameters . . . 72
3.15 . . . 73
3.16 Pareto optimality using NDFeB ($B_r = 1.2$[T]) . . . 74
3.17 Results validation (15MW) . . . 74
3.18 Optimized machines parameters . . . 76
3.19 Pareto optimality using NDFeB ($B_r = 1.2$[T]) . . . 76
3.20 Results validation (5MW) . . . 77
3.21 Optimized machines parameters . . . 78
3.22 Pareto optimality using NDFeB ($B_r = 1.2$[T]) . . . 79
3.23 Results validation (5MW) . . . 79
3.24 Optimized machines parameters . . . 81

4.1 Main components of the total number of failures for wind turbine subsystems 84
4.2 Publication related to mechanical gear failures . . . 85
4.3 Planetary gearbox illustration [141] . . . 85
4.4 Topology proposed in [144] . . . 86
4.5 Publication related to magnetic gear design . . . 87
4.6 Main parameter of the studied magnetic gear . . . 88
4.7 Best individual for each generation evolution (ratio 1:5) . . . 90
4.8 Validation of the obtained results (ratio 1:5) . . . 90
4.9 Fourier analyses . . . 91
4.10 Best individual for each generation evolution (ratio 1:10) . . . 91
4.11 Validation of the obtained results (ratio 1:10) . . . 92
4.12 Fourier analyses (ratio 1:10) . . . 92

4.13 Best individual for each generation evolution (ratio 1:20) 93
4.14 Validation of the obtained results (ratio 1:20) 93
4.15 Fourier analyses (ratio 1:20) 94
4.16 Comparison of root mean square values of magnetic flux densities for different ratios 95
4.17 Studied structure 97
4.18 Pareto optimality for different poles number 98
4.19 Poles number influence on optimization results 100
4.20 No-load root mean square value of normal magnetic field density 101
4.21 Validation of the obtained results 102
4.22 Class insulation influence on Pareto optimality 103
4.23 Insulation class influence on optimization results 105
4.24 Validation of the obtained results 106

List of Tables

1.1 Offshore wind farms . . . 19
1.2 Large wind turbine data . . . 20

2.1 Allowed hottest spot for each insulation class . . . 30
2.2 Physical and geometrical parameters for the studied generators . . . 43
2.3 Thermal simulation conditions . . . 47

3.1 Thermal proprieties used for the optimization . . . 63
3.2 Optimization parameters (15 MW) . . . 65
3.3 Comparison between FEM and the developed model results . . . 66
3.4 Active parts masses [kg] . . . 66
3.5 Optimization parameters (8 MW) . . . 67
3.6 Comparison between FEM and the developed model results . . . 68
3.7 Active parts masses [kg] . . . 68
3.8 Optimization parameters (5 MW) . . . 70
3.9 Comparison between FEM and the developed model results . . . 71
3.10 Active parts masses [kg] . . . 71
3.11 Optimization parameters (15 MW) . . . 74
3.12 Comparison between FEM and the developed model results . . . 75
3.13 Active parts masses [kg] . . . 75
3.14 Optimization parameters (8 MW) . . . 76
3.15 Comparison between FEM and the developed model results . . . 77
3.16 Active parts masses [kg] . . . 77
3.17 Optimization parameters (5 MW) . . . 79
3.18 Comparison between FEM and the developed model results . . . 80
3.19 Active parts masses [kg] . . . 80

4.1 Magnetic gear prototypes . . . 87
4.2 Fixed parameters during optimization . . . 88
4.3 Optimizations variables and their ranges . . . 89
4.4 Poles number in elementary unit for each gear ratio . . . 89
4.5 Comparison between FEM and the developed model results (ratio 1:5) . . . 91
4.6 Best solution parameters (ratio 1:5) . . . 91
4.7 Comparison between FEM and the developed model results (ratio 1:10) . . . 93
4.8 Best solution parameters (ratio 1:10) . . . 93
4.9 Comparison between FEM and the developed model results (ratio 1:20) . . . 94
4.10 Best solution parameters (ratio 1:20) . . . 94
4.11 Fixed parameter during poles influence optimization . . . 97

4.12 Optimizations variables and their ranges 97
4.13 Comparison between FEM and the developed model results 103
4.14 Comparison between FEM and the developed model results 106

General Introduction

Through the expansion of wind energy in the world wide and especially in Europe, many challenges still exist and new ones appeared, which wind turbine manufactures need to overcame. Overall cost of energy reduction through the minimization of failures rates, downtimes and turbine mass are large objectives for these manufacturers. Adwen (Known previously as Areva wind) entered the wind market with their AD-5 and AD-8 wind turbines and takes these problematical seriously in order to offer a competing product in offshore wind turbine. This PhD aims to investigate a large domain of solution through optimal multi-physics design thanks to the industrial found (Cifre 2014/0750) which regroups Adwen France and GREAH laboratory together. Therefore, an optimal examination of the integration in wind energy conversion chain of permanent magnet synchronous machine in concentrated flux and surface mounted structure will be analyzed, while beside this analysis permanent magnet gears will be studied too. Which defines the PhD problematic by giving the optimal solution sub domains and by providing a continuity to the laboratory research works, where optimal design of different topologies of permanent magnet generators is, was and will be carried on in [1, 2, 3, 4, 5, 6]. In order to achieve these goals, the PhD will be divided into four chapter as follow:

The first chapter treats the state of the art of wind power, where its implementation as an alternative energy will be discussed followed by an overview on the global wind power for onshore and offshore sites. After that a look at market share for manufacturers will be given with their respective technologies, which includes different drive and electrical machine structures; such as direct or indirect drive and synchronous or asynchronous machines. This will be succeeded by non-exhaustive list of multi-megawatt wind turbine and offshore wind farms. Finally this first chapter will be ended by a conclusion.

The second chapter explains the multi-physics modeling of electrical machines, where first the magnetic model will be proposed through the use of reluctance network with consideration of non-linear behavior of iron. Second thermal modeling will be achieved with the help of lumped model , with a close look at thermal coefficient computation such as; convection coefficient in airgap and equivalent slot's conductivity. Third, magnetic results obtained from the proposed model for two permanent magnet structures will be validated by comparing them with commercial software using finite elements method. Finally, thermal results will be compared with measurements followed by a conclusion.

The third chapter treats optimal design process of electrical machines. In order to achieve it, an introduction to optimization through general mathematical expressions will be given followed by examples of typical problems met during optimization process through benchmark functions. After that, a brief introduction of optimization algorithms will be given in mono-objective and multi-objectives with consideration of constraints. This will be succeeded by an optimal design for three different power and for two selected permanent magnet machine using the developed models, where a comparison between performance will be carried on.

The final chapter investigates the integration of magnetic gear in wind energy conversion chain through an optimal design using the developed model in the second chapter. In parallel the integration of direct drive permanent magnet machine will be discussed

too through the same third chapter optimization procedure. Finally conclusion and comparison between the magnetic gear or direct drive integration will be discussed.

A final discussion on the obtained results, future works in the GREAH lab related to this PhD and perspectives will closure this report

Chapter 1

Stat of the art: offshore wind turbine generator

Introduction

Pushed by the energy crisis of 1970, the renewable energy sector became a major area of interest for both industrialized countries (China, US, Germany . . .) and private companies [7, 8]. At the universal scale, the Paris agreement in November 2016, which aims to hold the increase in the global average temperature below 2[°C], started to affect the renewable energy targets by creating new global challenges. Moreover, other interlinked areas were impacted by this greatly step towards green power such as environment, economy, and technical development, dealing with the collection of the energy, the cost of the conversion systems (Design, installation, maintenance, and supervision), and the conception of an optimal efficient systems. Therefore, many solutions were proposed to ensure a reliable decarbonized energy sector, that derived from natural processes, at the same time, secure and with affordable costs; through a seamless and successful energy transition.

1.1 Renewable energy as an alternative Energy

As it can be seen from Fig. 1.1, the conventional energy consumption, which remained steady for many years, is the most common type of energy converted to final power in the world on 2015 with almost 78.5 % of the total final energy consumption[9]. Afterward, we can notice that the renewable energy (including: traditional and modern biomass, geothermal, solar heat, hydropower, biofuels for transport, wind and solar) totaled 19.3% showing slight growth of approximately 0.3% from 2013 as a results of the its strong cost reductions over recent years [10]. In contrast, renewable energy is estimated to reach a pick at 30% of the global power generation by the end of 2016; which is enough to produce approximately the quarter of the world's electricity. Although, all the governments and industrial efforts the oil, coal and natural gas remains the world's dominant fuels.

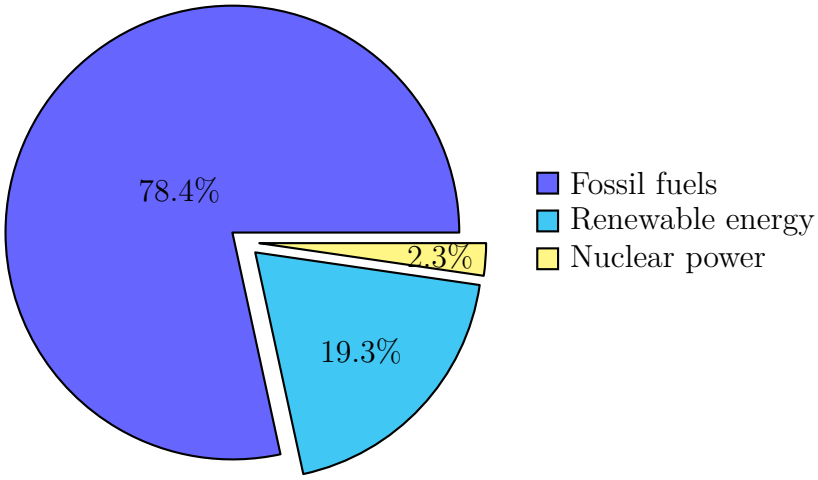

Fig. 1.1: Overall share of renewable energy [9]

Nevertheless, the renewable energies are progressing significantly with the reduction in costs that is a normal consequence of the ever-increasing awareness of the importance of such kind of energy (policy development, supporting mechanisms). Although many countries try to widen geographical support of some renewable energies, to meet the rapid rise on the electricity demand and moderate the cost of energy COE, Wind energy seems to be the most competitive way to clean energy generation, as seen in Fig. 1.2. In contrast, solar power faces limitation since its linked to region's specifications. In addition, hydropower energy is considered to be fully developed ([11]). To sum up, the number of the wind power's markets is increasing all over the world, because wind offers the least-cost option for the new power generation capacity, as can be seen from the bar chart, provided by the international renewable energy[12, 10].In addition, the statistics shows that the biggest companies that that invest in renewable energy concentrate on the wind power with 54 % for power purchased[9].

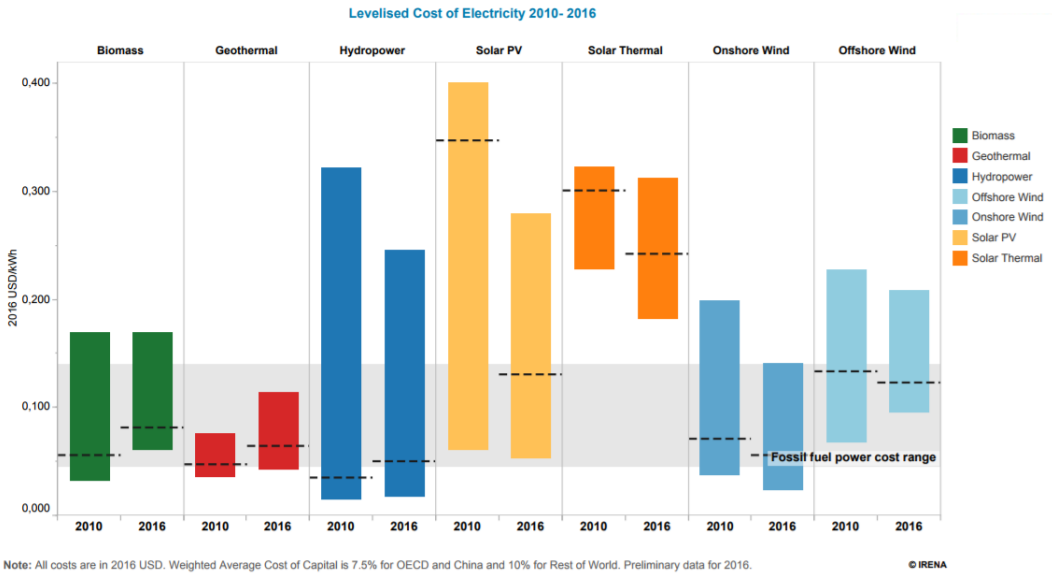

Fig. 1.2: Levelised Cost of electricity 2010-2016 [9]

By the end of 2016, the global installed wind capacity reached 487 GW as estimated by the industry's premiere global report Global Wind Market Report of 2017 [13]. Led by Asia as the largest regional market since 2008, with 27.72 GW on 2016 nearly the half of the global installations wind energy. Then, in the second rank, the European union wind power has overtaken the coal as the second largest form of power generation capacity, with 12.49 GW additional wind capacity both installed, and grid-connected on 2016 [13]. Therefore, in the same year, the wind power accounted for 51 [%] of total power capacity installations in Europe, as can be seen in Fig. 1.3.

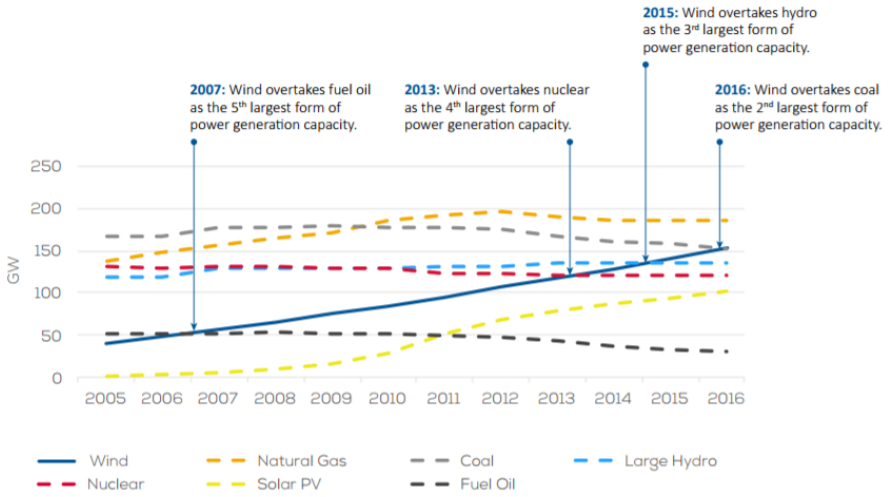

Fig. 1.3: Cumulative power capacity in the European Union by technology 2005-2016[14]

1.2 Overview on the global wind power

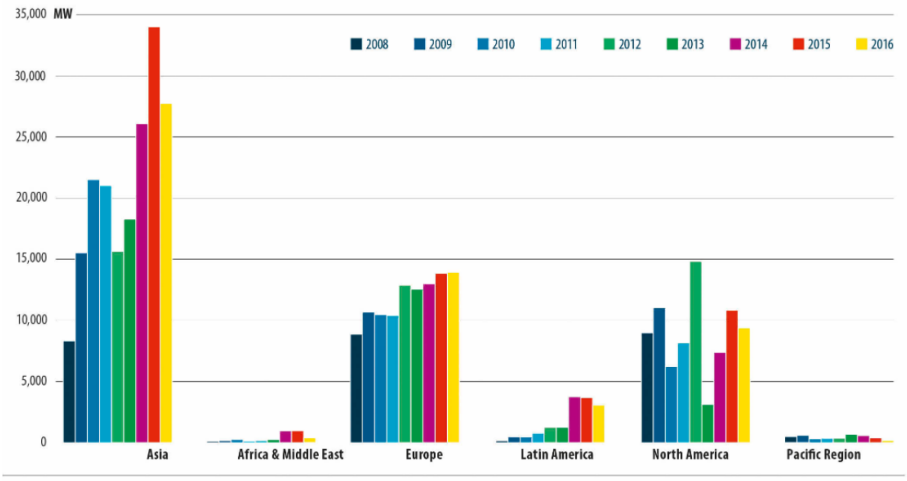

	2008	2009	2010	2011	2012	2013	2014	2015	2016
Asia	8,320	15,507	21,481	20,981	15,624	18,252	26,058	33,962	27,721
Africa & Middle East	96	251	153	8	131	240	934	953	418
Europe	8,851	10,660	10,466	10,393	12,862	12,524	12,988	13,831	13,926
Latin America	128	471	459	771	1,248	1,240	3,744	3,678	3,079
North America	8,969	11,008	6,208	8,137	14,807	3,112	7,382	10,829	9,359
Pacific Region	482	578	294	345	358	655	568	381	140
	28,854	**38,475**	**39,061**	**40,635**	**45,030**	**36,023**	**51,674**	**63,634**	**54,642**

Source: GWEC

Fig. 1.4: annual new installed capacity by region from 2008 to 2016 Global [13]

Asia as can be seen in Fig. 1.4, it is clear that although slight marked reduction on the annul installed capacity in Asia by the end of 2016, it has been the largest developer of wind installation since 8 years ago. China, the huge market globally, which accounted for 42.8[%] of the new wind installations in the world, remained its lead with more than 86[%] of the Asian market. However, India, Japan, and south Kora made some favorable signs on the horizon. By the supporting the research on the wind systems technologies (Smart control technology of wind turbine, key technologies of intelligent operation and maintenance of large scale wind farm) China is expected to expand its cumulative wind energy.

Europe Europe, with the second spot in the world annual installed capacity of wind energy now, showed gradual fluctuation from 2008. However, nearly 96[%] of this capacity were implemented on the European Union EU, specifically Germany added more than 39[%] (5.44 GW) in the European wind capacity, which allowed it to reached more than 50 GW cumulative capacity, followed by Spain (23.07 GW), UK (14.54 GW) and France (12.06 GW), as illustrated in Fig. 1.6. Hence, Germany joined the international competition with Chine and USA, countries with cumulative wind power rate of more than 50 GW, as the first European leader in term of new installations and cumulative capacity.

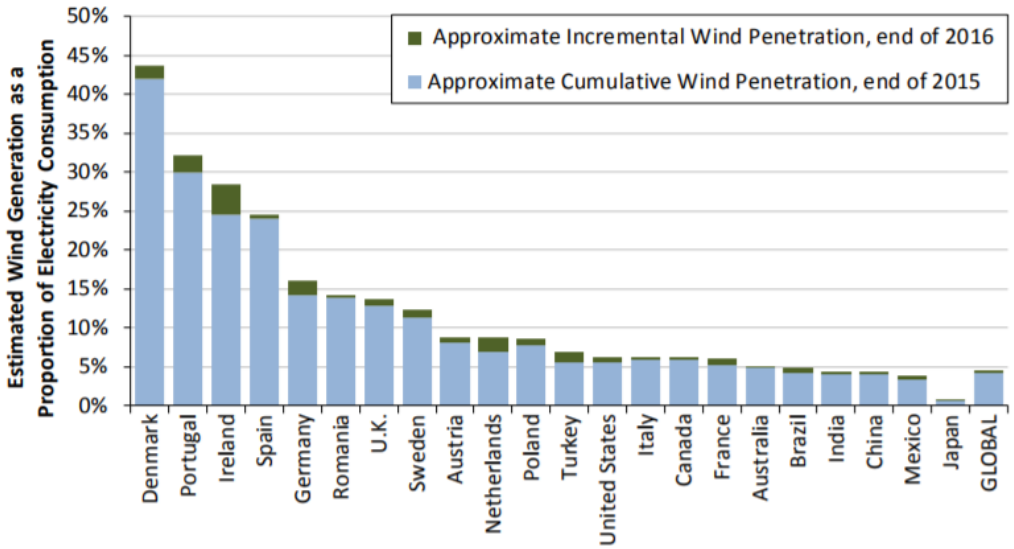

Fig. 1.5: Approximate Incremental Wind Penetration [15]

According to the global wind energy council GWEC, records in new wind power installation were broken by France, Netherland and Finland (1.56GW, 0.88GW and 0.57 GW respectively) Fig. 1.5. Furthermore, the EU is generating nearly 10.4 [%] of its electricity demand from the wind power [14], as stated in Fig. 1.7. Although the wind capacity in Germany is considerably higher than Denmark's one, but the later was, in 2016, the EU's member with the highest penetration the percentage of demand covered by wind energy in a certain region, normally on an annual basis rate (37[%]) three times more than the European average, compared to Germany with (16[%]). Thereby, with this elevated percentage, by 2021 the Denmark is predicted to reach 50[%] of the country's electricity consumption by wind energy [13].

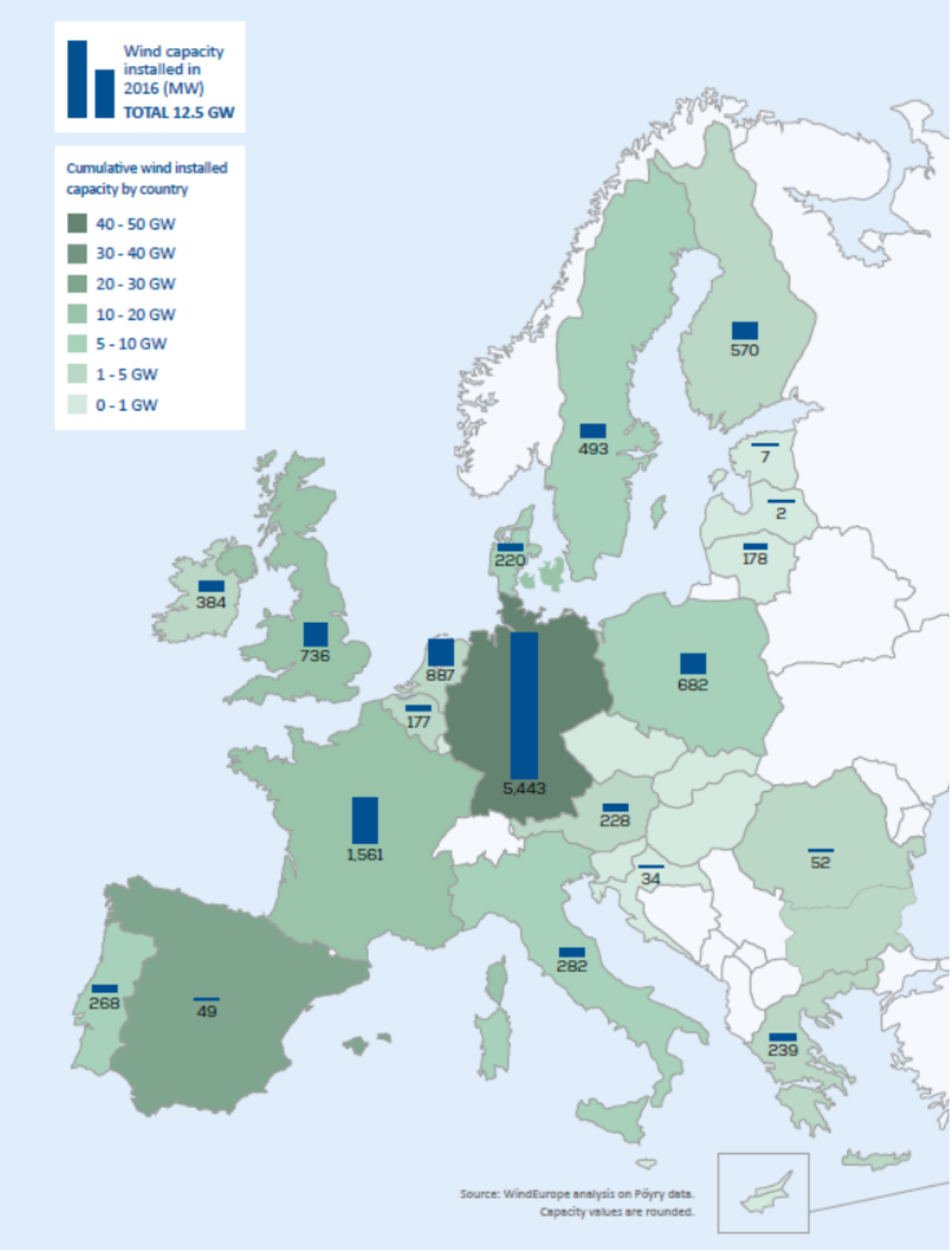

Fig. 1.6: Trends in Renewable Energy in the European Union[14]

Beyond the EU, Turkey is market in wind energy is looks promising, referring to the Global Wind Energy Council GWEC in its last report. In 2016, Turkey was in the list of the top 10 countries in the world with new installed wind capacity, in the 7th place with almost 1.4 GW.

Electricity production from wind power (TWh)

TOTAL EU ELECTRICITY CONSUMPTION (TWH)	ONSHORE WIND ENERGY PRODUCTION (TWH)	OFFSHORE WIND ENERGY PRODUCTION (TWH)	WIND ENERGY PRODUCTION (TWH)	SHARE OF EU CONSUMPTION MET BY WIND ENERGY
2,860	259	37	296	10.4%

Source: WindEurope

Fig. 1.7: Electricity production from wind power [14]

North and South America The market of wind energy in the North America is completely different from that of the Latin America. While the North part (USA, Canada and Mexico) was in a stiff competition with Europe and Asia in the last five years, the south one is far from such considerations; although it accounted for 34[%] of the American annul installed wind capacity. On December 2016, more than 90[%] of the American's wind capacity were spread across three countries the United States, Canada and Brazil. Thus, the USA is the second largest market in the world in terms of new wind power installations, after China. Moreover, according to the International Energy Agency IEA the USA department of Energy DOE is working in many projects to optimize wind design systems. For example, a successful testing of advances drivetrain with simplified gearbox which aims to Improve the Reliability of Wind Turbine at the National Renewable Energy Laboratory NPEL [16]. Also, Researchers at the same laboratory released a new version of FAST (FAST v8), an open-source, multiphysics engineering software tool used to design and analyze wind turbines [17]. The development wind's technologies is expected to continue in the USA, which is trying to bring the wind energy technology to the forefront of renewable technological development.

Middle east, Africa and Pacific Region According to the last report in [13]. The total new wind installation in Africa, Middle east and Pacific Regions was much lower than the global average, with 418 MW and 140 MW respectively. This capacity is nowhere near as experience as the others in Europe, Asia and America. The market of new wind capacity, in this three regions, reached high point in 2014 before falling sharply on the last years Fig. 1.4. For the MEA (Middle east and Africa), are generally discussed for long time as ripe region to explore solar energy. Therefore, wind power does feature highly in the region's energy mix [18]. In contrast, South of Africa and Morocco are embarking on a new era, by setting new and they are expected to expand their capacities over next years. In the Pacific Region, Australia leads this region on the new installed wind power capacity with 140 MW and more than 4 GW cumulative capacity.

1.3 Onshore and offshore wind turbines

Highly recommended by the research institution, industries and governments, the offshore wind turbine seems to be the ideal solution to increase the wind power exploitation with lower costs [19]. Despite the fact that the onshore technology is mature one with af-

fordable energy's cost, it presents many problems from the visual pollution and noise to the land use high power generators for offshore wind turbine. In contrast, the offshore wind turbines offer large area of availability, stronger wind and less visual pollution high power generators for offshore wind turbine. Hence, the short-term prospects look bright. Nevertheless, there are more environmental restriction at the offshore

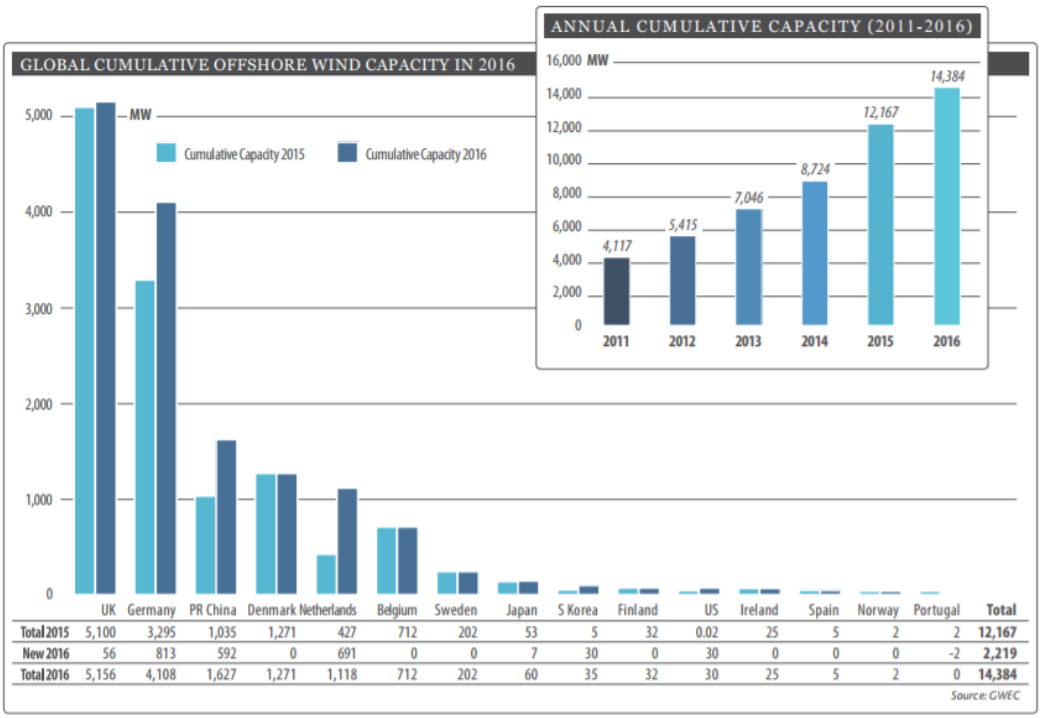

	UK	Germany	PR China	Denmark	Netherlands	Belgium	Sweden	Japan	S Korea	Finland	US	Ireland	Spain	Norway	Portugal	Total
Total 2015	5,100	3,295	1,035	1,271	427	712	202	53	5	32	0.02	25	5	2	2	12,167
New 2016	56	813	592	0	691	0	0	7	30	0	30	0	0	0	-2	2,219
Total 2016	5,156	4,108	1,627	1,271	1,118	712	202	60	35	32	30	25	5	2	0	14,384

Fig. 1.8: The global offshore wind capacity in 2015 and 2015 by region

In term of the offshore farms, the Europe is way out ahead in terms of cumulative offshore wind capacity (America, Africa, Asia and Australia). Based on the statistical data in the Fig. 1.8, with its high wind resource potential, the UK has been the world leader with 5.1 [GW], followed by Germany and China with nearly 4.1 [GW], 1.63 [GW] respectively. In addition, the EU countries accounted for 97% offshore wind installation, which are connected to grid [13]. Overall, 2016 was another special year for the offshore wind turbine, were the first 8 [MW] turbines were connected to the grid.

1.4 Manufactures of wind turbines

According to wind monthly article [20], Vestas takes the lead in the win energy capacity, offshore and onshore counted, with more than 20 [%] of market monopoly for the installed capacity in 2016 and cumulative one. SiemensGamesa comes second thanks to the joint-venture, followed by general electric and Gold wind. These four manufecterer by them selves hold more than 60 [%] of the installed capacity in 2016 and cumulative one. Enercon, Nordex, United power and Senvion follow the lead with less than 12[%] of the installed cumulative capacity for each, as can be seen in Fig. 1.9.

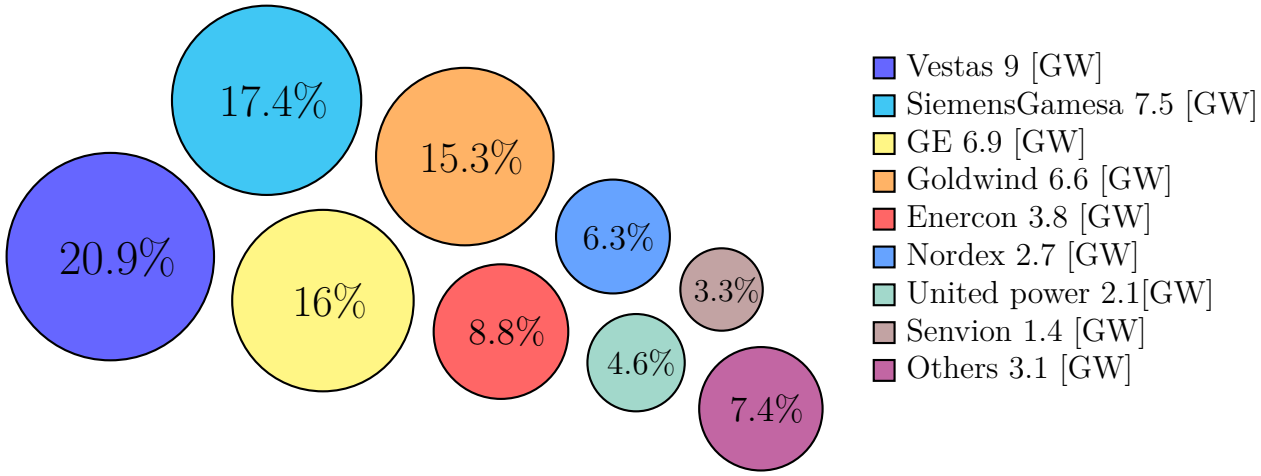

(a) Installed in 2016

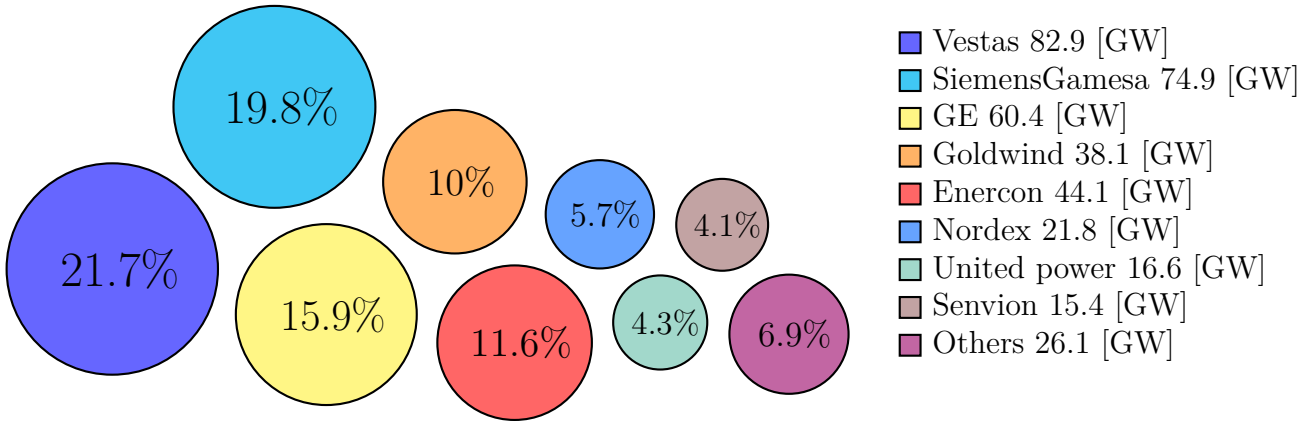

(b) Cumulative capacity in 2016

Fig. 1.9: Wind turbine manufactures capacity [20]

Fig. 1.10 shows the market share of offshore wind turbine in the world in terms of cumulative and annual installed capacities in 2016. It may be seen that Siemens, which made up nearly 67 [%] of the global installed capacity and 60 [%] of the cumulative one, is on the top of the offshore wind turbine suppliers. However, despite the fact that Vestas had no noticeable new installation in the last year, it was the second large company that cumulated wind energy. In addition, nearly the quarter of the global new installed capacity was done by Sewind. Therefore, it goes currently into serious competition with Siemens. However, there was many other companies such as Sewind, Senvion, Adwen and Bard with small capacities.

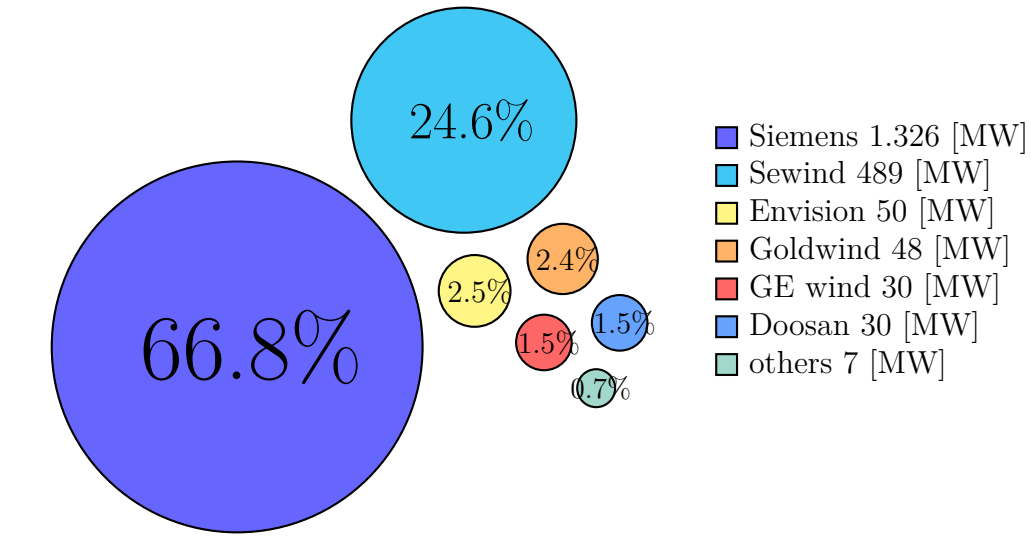

(a) Installed in 2016

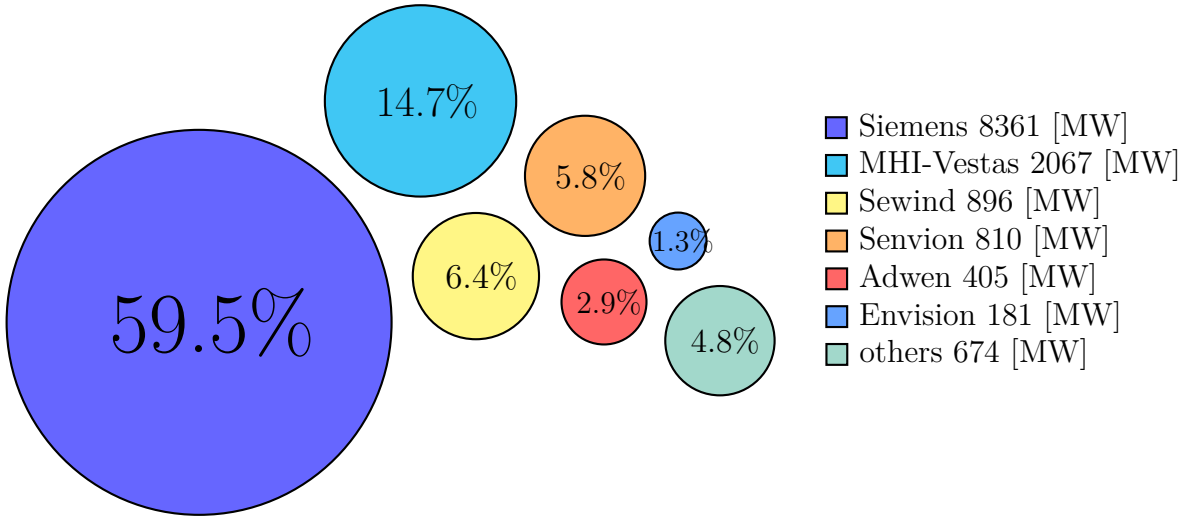

(b) Cumulative capacity in 2016

Fig. 1.10: Offshore wind turbine manufactures capacity [21]

1.5 Wind turbine technology

Wind turbine manufactures adopted different technologies, evolving through the time, in order to reduce energy cost through minimizing failures, material's fatigue, volume and weight. Two main ideologies can be distinguished, from which others can be sectioned too. The first ideology, called indirect drive chain, consists of of integrating a mechanical gearbox between turbine's rotor and generator shaft in order to increase generator speed, which systematically reduces its torque and thus generator's volume and weight. However, gear ratio must be chosen carefully through rigorous optimization in order to minimize energy cost, since increasing too much gear ratio will require more stages for gearbox and will increase failure rate by adding more rotational pieces. The second ideology, known as direct drive chain, couples directly turbine's rotor with generator shaft, which means that generator has the same speed as turbine, while both of them share the same torque, which results by a higher generator weight, since the requested torque in generator shaft

is higher compared to the first ideology. However, the number of rotational mechanical parts is reduced, which may simplify assembly procedures and reduces failures rates. Furthermore, types of generator used in both ideologies will be given:

1.6 Electrical machines used in indirect drive train

Indirect drives also called geared drives use a gear box in order to increase generator speed and thus amplify its power density. Four this type of drive train, two categories of electrical generator can be used, synchronous machine in large wind turbine and asynchronous one mostly for medium and small wind turbines. This choice is related to the manufacturing simplicity and its relatively low cost. However, due to the development of power electronics the use of synchronous permanent magnet generator is growing in medium and small wind turbines, while for large one the use of such technologies is caused by the similar cost of energy over 20 years compared to asynchronous generators.

For the case of asynchronous machine, squirrel cage or winding can be used for rotor structure. For the squirrel choice the performance will be good accompanied by low cost maintenance presenting a robust and stable state. However the squirrel cage asynchronous machine is not suited for maximum power extraction, operates in a fixed range of speed with transmission of all wind speed fluctuation to the grid and most of all consumes reactive energy, which will need compensation capacities. Therefore the use of squirrel cage machines can be considered in river with is quasi-constant flow.

For wound rotor asynchronous two strategies exists, the first one consist of adding a resistor in series with rotor winding in order to operate at interval of speed, however the efficiency was low. Doubly fed asynchronous machines have the advantage of controlling the speed and power through its rotor winding and thus the stator is connected directly to the grid while the converter controlling the rotor winding current is sized around 40 [%] of nominal power. This constitutes the main advantages, however the complexity of the manufacturing and preventive maintenance constitutes a big disadvantage for this topologies.

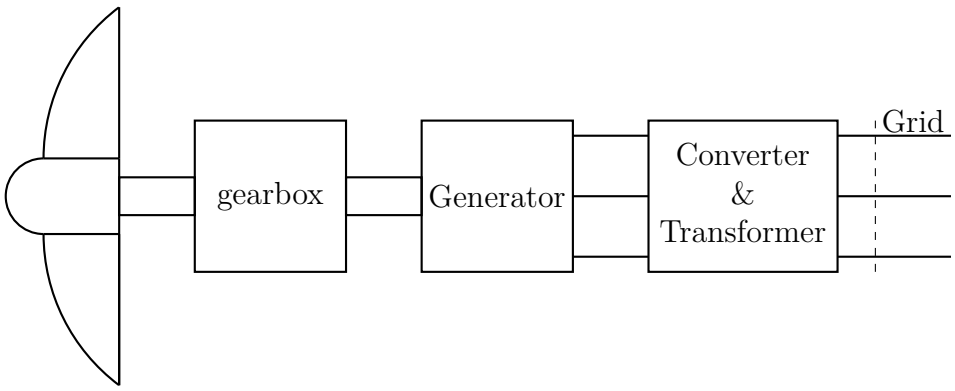

Fig. 1.11: Geared topology

The geared technologies can be separated too into two subcategories, medium speed and high speed one. Low-Medium speed drives uses one single stage planetary gear coupled to permanent magnet synchronous generator, which brings the advantages of

compact structure and eliminates failures related to high speed stage[22]. This solution enables a step-up ratio on 1:10, providing a nominal generator speed around 150 [rpm], while two-stages gear box offers a ratio up to 1:40. The two stages gearbox offers a ratio up to 1:40 resulting by a nominal speed of 500 [rpm] at generator shaft, reduces generators size and enable the use of a doubly feed asynchronous generator, which may cut the overall price of energy. The two listed subcategories represents a fear concerning the premature failure of gearbox due to vibration, misalignment and or loads caused by wind ripples [23]. Planetary gear box is the most suited for wind energy conversion drive chain, since it offers compact size and represents a high density, Fig. 1.12b illustrates the one stage planetary gear, used in low-medium speed generator, while Fig. 1.12a exposes a three stage planetary helical gear, used for high speed drive trains.

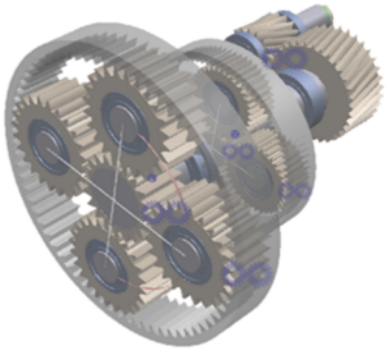

(a) 3-stage[24]

(b) One stage[25]

Fig. 1.12: Planetary helical gearbox

1.6.1 Asynchronous generator

From the point of view of industrialization, the asynchronous generators are among the best candidates, considering the simplicity of their manufacturing, which has been perfectly mastered for years their costs reduction. They are well adapted in high speeds, present ease of maintenance and have a low failure rate compared to other structures. Nevertheless, they are not suitable for direct drive applications because they require the presence of a gearbox in order to have a correct performance [4].
The rotor of the asynchronous generator may have different structures; can be solid smooth or grooved, or laminated with a conductive layer or a reinforced squirrel cage. Its operating principle is based on the interaction between the rotor flux and the stator currents. Compared to permanent magnet synchronous machine, asynchronous ones have higher Joule losses caused by rotor currents, a lower efficiency and power factor, however they can withstand a higher temperature rise. Work in progress aims to put in place more efficient means of cooling and a structural improvement of the machine to better evacuate the generated heat [26].

1.6.1.1 Squirrel cage asynchronous generator

This structure was used in the early time of wind energy through flywheels and converters, however its rival with wound rotor took the spot, presenting a relatively easy and cheap command [3].

1.6.1.2 Wound rotor asynchronous generator

This machine is marketed by several manufacturers like Vestas, Gamesa since and operates at variable speeds. The stator is coupled to the grid through a transformer while the rotor is wound and connected to a static converter, adjusting the slip through its command. Wound rotor structure imposes the presence of a gearbox since the nominal rotation speed is high [3]. To achieve an appropriate coupling with the grid, one of the solutions is to use two three-phase pulse width modulating inverters, where one is in rectifier mode and the other in inverter mode. The major disadvantage of this solution is related to the interactions between the inverter the grid, generating particularly over-currents and voltage dips[27].

1.7 Electrical machines used in direct drive train

Direct drive topology, as illustrated in Fig. 1.13, is based on a permanent magnet synchronous machine with high poles number and considered the best solution for offshore wind turbines and tidal turbines in a lot of research work[3], knowing that their use provides 17% addition in torque density compared to asynchronous generators and up to 25% when it is compared to wound rotor synchronous machine[26, 28]. Direct drive topology offers better performance and low maintenance costs, compared to the geared one. However, their manufacturing cost is high, because the magnetic materials require a cooling system and the power electronics must be sized for the transfer of the total power. In addition to all this, a technical and economic study must be carried out in order to choose the most suitable topology for the application. However [22] states that in the overall price, direct drive solution is quite comparable with geared one, which is due to the lack of maturity of direct drive technology compared to the geared one.

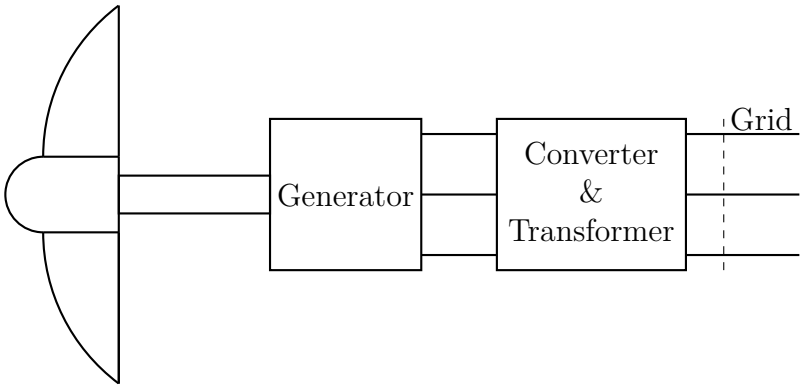

Fig. 1.13: Direct drive topology[29]

The permanent magnet synchronous generator can have an inner or an outer rotor, in the outer rotor configuration the generator may have less volume since outer rotor solution offers more torque density. Outer rotor technology was adopted by Siemens in their 3 [MW] wind turbine [30]. Enercon also adopted direct drive structure for their 7.5 [MW] turbine [29], as can be seen in Fig. 1.14 where:1)rotor blade, 2)rotor hub, 3)hub adapter4), annular generator, 5), main carrier, 6)yaw drive

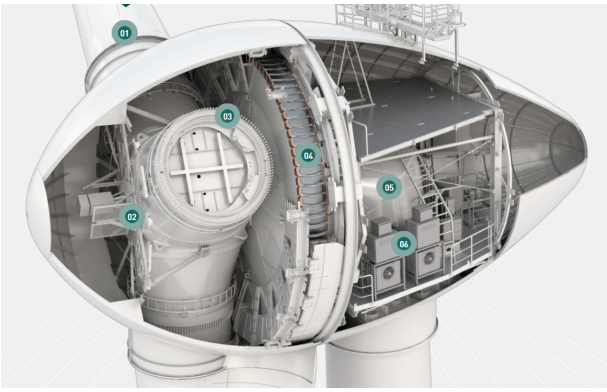

Fig. 1.14: Enercon E126 wind turbine concept[29]

Since the synchrounos machine has bigger volume, manufacturers though of segmented structure, as can be seen in Fig. 1.15, in order to decrease the price and simplify transportation a logistics.

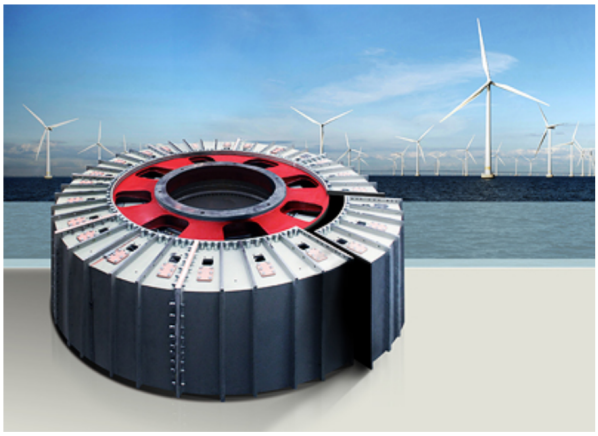

Fig. 1.15: Segmented generator concept by Siemens [31]

1.7.1 Synchronous machines

In general, the cost of synchronous machine is higher than asynchronous one, but the synchronous machine presents a better efficiency for the same requested torque at the same speed with consideration of long term investment. Moreover, synchronous generator responds well to the constraints of a direct drive [4]. This machine was mainly marketed by Enercon, Siemens and Largerwey. With the development of converters power, its integrations in the wind energy conversion chain has become more feasible thus offering an additional attraction to wind manufacturers.

The most used synchronous generators can be classified according to the direction of magnetic flux in the airgap. For the direct drive generators, several researchers like [32, 33, 34] demonstrated the benefit of axial flux structures with respect to their radial flux candidates. The airgap volume is increased in axial flux generator by their natural structure, which results in a higher torque density as can be seen in (1.1).

$$\begin{cases} \Gamma_{\text{radial}} = f(R_{\text{gap}} \times L_{\text{act}}) \\ \Gamma_{\text{axial}} = f(R_{\text{ext}}^2 - R_{\text{int}}^2) \end{cases} \tag{1.1}$$

With L_{act} and R_{gap} as active length and mean airgap radius of the radial flux machine respectively, R_{ext} and R_{int} are respectively outer radius and inner rotor one for axial flux structures.

1.7.1.1 Wound rotor synchronous machine

In the wound rotor synchronous machines the rotor field is created by windings, it can be modulated electronically, which allows an easy control at high speed. However, these structures require electrical contact with the rotor (brush-collector system) which dramatically reduces the its life and complicates its maintenance [35]. These machines are characterized by a better torque density compared to the asynchronous generator but without reaching permanent magnet one. Indeed, the rotor winding causes additional Joule losses leading to both a decrease in efficiency and additional heating. The cooling of this type of machine relatively complex [35].

From the construction point of view, the rotor is formed of polar masses around which are surrounded excitation coils, as can be seen in Fig. 1.16a. These polar masses can be made of solid steel or by a stack of sheets to reduce iron losses. The rotor flux is obtained, therefore, thanks to the excitation current injected into the rotor coils. The stator consists mainly of windings and laminated minimize eddy current losses [36], as illustrated in Fig. 1.16b, Fig. 1.16c and Fig. 1.16d.

1.7.1.2 Permanent magnet synchronous machine

From mass torque density view, the permanent magnet synchronous machine offers a better performance by comparing it to its rivals (synchronous with wound rotor and asynchronous one). Indeed, according to [26], the use of permanent magnet ensures a gain 17 [%] relative to the asynchronous generator. On the other hand, and according to [28], these structures provide a 25 [%] gain compared to rotor wound structure at identical speeds and for the same power. However, the permanent magnet synchronous generator converter needs to be sized at 100 [%] of the nominal power against 30% for doubly fed asynchronous generator [37].

Historically, the permanent magnet synchronous generator have been the focus of significant research efforts in the world wide. This technology can thus be considered as a viable one, given their advantages and use in a wide variety of applications [1, 2]. These structures are classified according to the arrangement of the magnets on the rotor and their different configurations include radial flux machines, axial and transverse ones. [34] indicates that among the topologies best suited for direct variable speed drive applications where permanent magnet generators takes the lead.

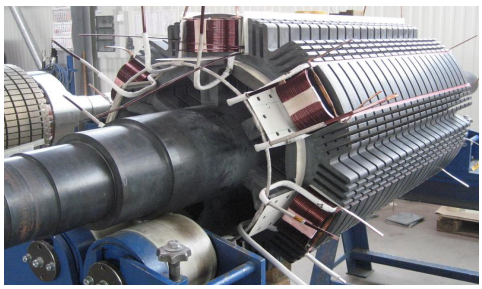

(a) Rotor winding[38]

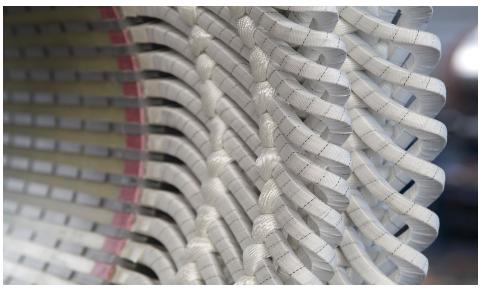

(b) Stator winding [38]

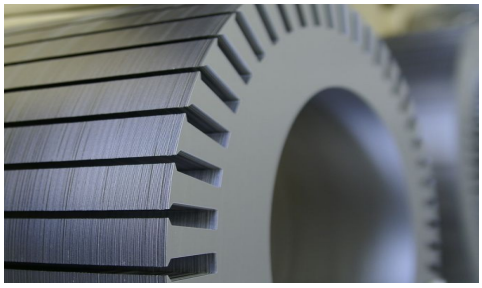

(c) Laminated core [38]

(d) Closed slot winding[38]

Fig. 1.16: Synchronous generator

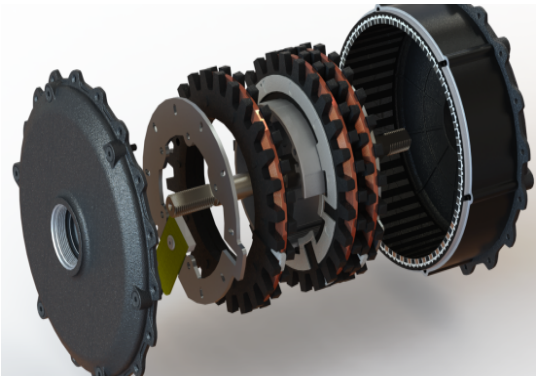

(a) Transverse flux[39]

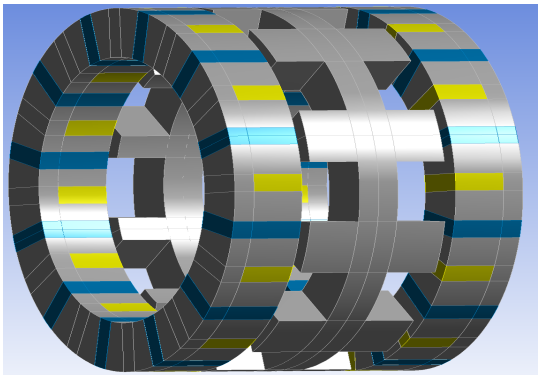

(b) Axial flux

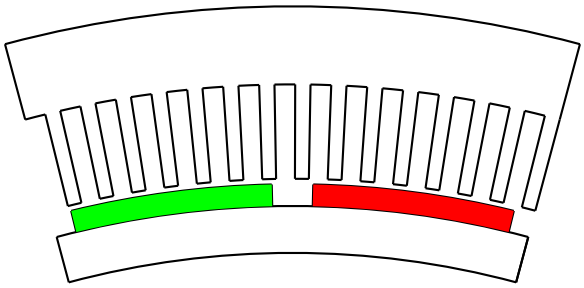

(c) Surface mounted

(d) Buried magnets[40]

Fig. 1.17: Different topologies of permanent synchronous machine

To control the airgap flux in these structures, especially in high speed applications, several research teams propose to use topologies with several excitation systems (Poly-excitation). Generally, two different sources of excitation are used, the flux is thus created

by magnets and by excitation winding (excitation coils). The second source is essentially used to control the magnetic flux created by permanent magnets [41].

1.8 Toward large wind turbines

The current research in the development of wind energy conversion systems are discussing the idea of upscaling the wind turbines more than the aerodynamic concepts. However, upscaling a turbine without affecting the amount of material, including its mass and volume, and the construction's cost can prove quite challenging [7]. Thus, researchers and their partners from industry are getting into the forward cutting-edge of the development on the Megawatts turbines with reduce volume and acceptable weight. Not surprisingly, the average size of offshore wind turbine is increasing over the last years Fig. 1.19. Therefore, with the promise of lower cost of energy, the cumulative number of turbines by size Fig. 1.18 confirms that there has been marked growth in the number of large wind turbines, since 2004. Due to the rise on the deployment of offshore wind turbines with capacity greater than 4 [MW], as illustrated in Fig. 1.18, the global power average of offshore wind turbine is nearly 4.8 [MW] in 2016. However, Siemens is the leader in the manufacturing of wind turbines with capacities more than 5 [MW], as can be seen in Fig. 1.20.

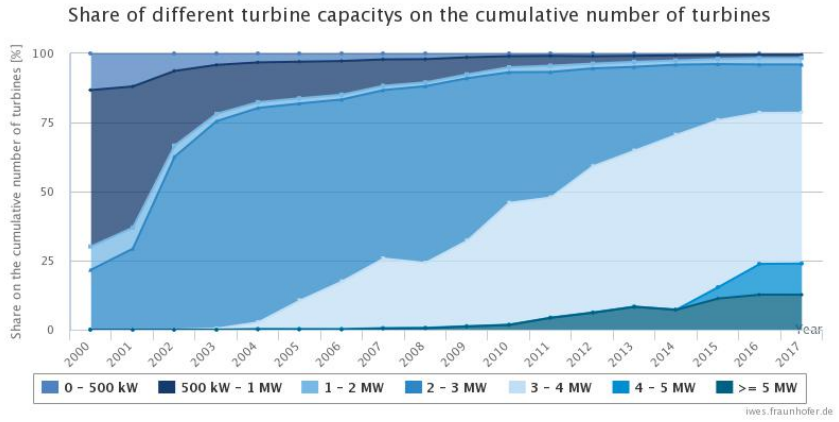

Fig. 1.18: Cumulative number of offshore wind turbine by size [42]

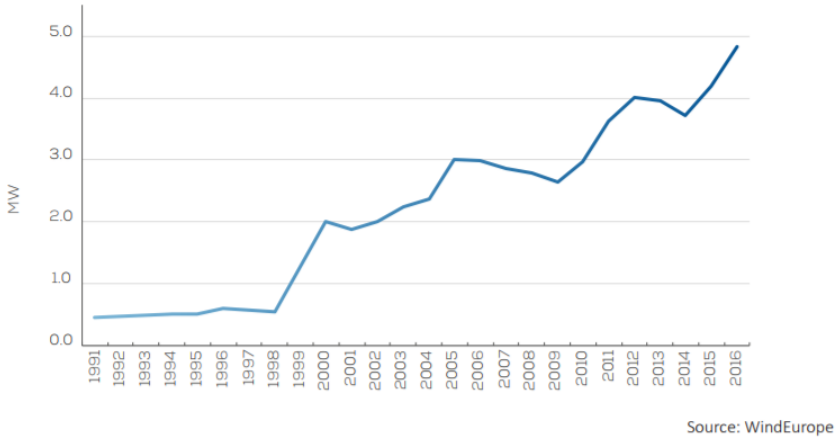

Fig. 1.19: Average offshore wind turbine rated capacity [MW] [21]

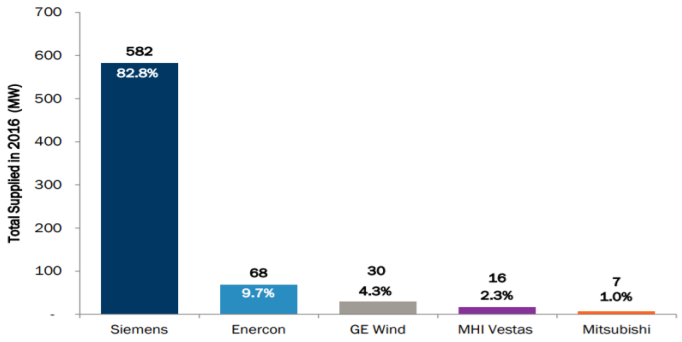

Fig. 1.20: top five suppliers by MW of wind turbines greater than 5 Mw in 2016 [21]

Table 1.1: Offshore wind farms

Farm	Total capacity	Turbine
Gode wind 1 and 2[43] Germany	582 [MW]	97 x Siemens SWT 6.0 Permanent magnet synchronous machine Direct drive
Dudgeon [44] UK	402 [MW]	67 x Siemens SWT 6.0 Permanent magnet synchronous machine Direct drive
Vejamate [45] Germany	402 [MW]	67 x Siemens SWT 6.0 Permanent magnet synchronous machine Direct drive
Bard offshore 1 [46] Germany	400 [MW]	80 x BARD 5MW Doubly fed asynchronous generator 3-stages planetary gear 1:97
Global tech 1 [47] Germany	400 [MW]	80 x AD 5-116 Permanent magnet synchronous machine planetary gear 1:10
Alpha ventus [48] Germany	60 [MW]	6 x AD 5-116 Permanent magnet synchronous machine planetary gear 1:10
T-W BORKUM [49] Germany	200 [MW]	40 x AD 5-116 Permanent magnet synchronous machine planetary gear 1:10
Wikinger [50] Germany	350 [MW]	70 x AD 5-135 Permanent magnet synchronous machine planetary gear 1:10
Nordseeone [51] Germany	332 [MW]	54 x Senvion SE6.2M126 Doubly fed asynchronous generator 3-stages planetary gear 1:116
Thorntonbank [52] Belgium	325 [MW]	48 x Senvion SE6.2M126 Doubly fed asynchronous generator 3-stages planetary gear 1:116

Table. 1.2 contains a non-exhaustive list of wind generator above 5 [MW] used in wind energy conversion. Where the battle between direct drive and indirect one is still on. The same battle opposes doubly fed asynchronous machines and permanent magnet synchronous one, as can be seen in Table. 1.1, where Germany hold a by part of the market, even-though the table presents a non-exhaustive list.

Table 1.2: Large wind turbine data

Turbine	Manufacturer	Rated power	Hub height	Rotor diameter	Rated wind speed
Sea Titan 10MW[53]	AMSC	10 [MW]	125 [m]	190 [m]	11.5 [$m.s^{-1}$]
Haliade [54]	General Electric	6 [MW]	100 [m]	150 [m]	–
SG 8.0 [55]	Siemens	8 [MW]	Site-specific	167 [m]	12 - 13 [$m.s^{-1}$]
SWT-7.0 [55]	Siemens	7 [MW]	Site-specific	154 [m]	13 - 15 [$m.s^{-1}$]
SWT-6.0 [56]	Siemens	6 [MW]	Site-specific	154 [m]	12 - 14 [$m.s^{-1}$]
E-126 [29]	Enercon	7.58 [MW]	135 [m]	127 [m]	16 [$m.s^{-1}$]
AD8 [57]	Adwen	8 [MW]	–	180 [m]	12 [$m.s^{-1}$]
AD5 [57]	Adwen	5 [MW]	–	135 [m]	11.4 [$m.s^{-1}$]
AE 5.0 [58]	Aerodyn	5 [MW]	–	139 [m]	11.8 [$m.s^{-1}$]
V164-9.5 MW [59]	MhiVestas-offshore	9.5 [MW]	–	164 [m]	13 [$m.s^{-1}$]
V164-8.0 MW [59]	MhiVestas-offshore	8 [MW]	–	164 [m]	13 [$m.s^{-1}$]
6.2M 152 [60]	Senvion	6.3 [MW]	–	152 [m]	11.5 [$m.s^{-1}$]
Gamesa [61]	Gamesa	5 [MW]	–	132 [m]	–

1.9 Problematic

As seen previously, it is hard to decide which technology to use; whether direct-drive or indirect one using permanent magnet machines or induction generators. A choice made on an optimal study is the best way to decide, however this requires a fast model with good accuracy, which justifies the choice of lumped models as explained in the second chapter. This model choice takes into consideration material proprieties such as B-H curve and magnet remanent flux dependency on temperature, all of this with being faster than commercial software using finite element method. The optimal design will be then applied on surface mounted permanent magnet machine and on concentrated flux one in the third chapter, with a close look at permanent magnet weight since their price is the most expensive one. NSGAII genetic algorithm will be used in order to find optimal solutions for the three targeted power 5, 8 and 15 [MW]. This will allow the estimation of the average needed permanent magnet weight for each mega-Newton-meter of torque. The fourth chapter investigates the integration of magnetic gears in wind turbines, since costs and downtimes related to mechanical gears are represents one of the drawbacks of direct-drive topologies. An optimal approach will be applied, as the same in the third chapter, in order to estimated the requested amount of permanent magnets for each mega-Newton-meter of torque, which will be compared to the amount of permanent magnet needed for direct drive topology using concentrated flux machines. Suggestions and remarks will cloture this report in a finale conclusion.

Conclusion

This chapter introduced a brief state of the art of wind energy chain conversion and its related problematics, where wind turbine technologies are clearly not mature enough to choose one dominant solution. Gearbox integration still a challenge since its use reduces the generator weight and size, thus its complexity, however it is accompanied by long downtimes and expensive maintenance costs which is represents a big drawback. Eliminating the gearbox or using only 2 stage one, will disable the use of doubly fed asynchronous generator, known for its relatively low price, and forces the integration of permanent magnet machines, which needs fast tools in order to investigate their integration in wind energy conversion chain. These fast and accurate models will be discussed and explained further in the next chapters through optima design procedure.

Chapter 2

Multi-physics modeling of electrical machines

Introduction

In this chapter the methodology used for the multi-physical predesign of electrical machines will be explained, especially the magneto-thermal case. Since the constraints defining the limits and the nominal operating point of the machine are either thermal, mechanical and/or magnetic and one can not optimize the magnetic behavior of an electrical machine without giving a look at its thermal response at least, which can be imposed by the insulation class and magnet's maximum allowed temperature. By cause of existence of many methods of multi-physical modeling, the choice depends highly on needs and design stage, which can be one from these three propositions mentioned in the literature [3, 4, 5, 62, 63]:

Analytical models The first method consist of solving analytically Maxwell's equations for the magnetic part or the heat equation in the thermal case under the assumptions of linearity of material's physical characteristics. This choice can be interesting if the simplicity of the geometry is provided directly or via transformation. Although this method is among the fastest one, it suffers from the lack of its genericity and can be easily trapped by numerical problems.

Lumped parameters The lumped parameters model is the second method which can be classified as a numerical solution, in which the domain is decomposed into subdomains associated to thermal or magnetic resistor/capacitor. With this method an equivalence is made between classical electrical circuits and thermal or magnetic ones, in which the non-linearity of materials can be taken into consideration and allows more complexity in the geometry compared to analytical modeling. This method gives a good accuracy/time compromise and will be deeply explained in the next section of this chapter.

Finite elements method It is known as the most accurate modeling method, despite its heavy computation time, especially for three-dimensional complex problems. Used generally in commercial softwares such as Flux-3D, JMAG or Ansys; which are adopted to adjust the parameters obtained from analytical or lumped parameters models in the final stage of design.

Depending on the study case and the made-up assumptions, a modeling method will be preferred over an other; if accuracy is the goal, the user must sacrifice the computation time and vice versa. In general a big compromise is found between computation time and model's accuracy, which can be represented in Fig. (2.1).

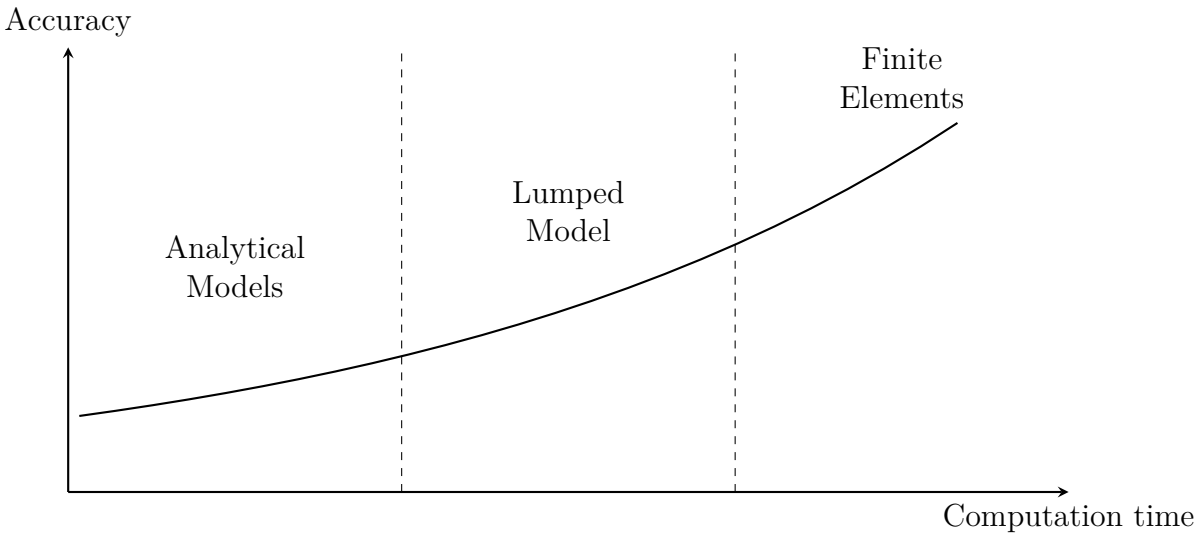

Fig. 2.1: Accuracy and computation time dependency on the modeling method[5]

This chapter will be divided into three different sections, the first one explains the lumped magnetic parameters and its formulation in magneto-static case, which will be followed by the explanation of reluctances computation. After that, the transient thermal lumped model will be elucidated too, with a clarification on the computation of heat coefficients; convection in the air-gap and equivalent conduction in the slot. In the third section, the connection method used for air-gap modeling will be exposed; in which the used method was chosen specifically to avoid numerical problems and to simplify the movement management. Finally results using lumped models will be compared to those obtained by finite element modeling employing the commercial software **Flux-2D** in order to justify the use of this type of solutions for future optimization problems.

2.1 Magnetic modeling of electrical machines

Meshed reluctance network **MRN**, is a numerical method used for the sizing of electromagnetic devices where an equivalence is made with electrical circuits[64, 65, 66]. The method it self is not recent, used first in late sixties for the computation of flux leakage in three-phase power transformers [65] and developed since then to predict the performance of several types of electromagnetic devices; such as Linear actuators in [67, 68, 69], tubular in [70] and radial ones in [71, 72, 73, 74].
The method it self consist of subdividing the domain into elementary ones, where in each one a reluctance and magneto-motive force (MMF) is affected in each direction that the developer considers important for the flux path. The reluctance and MMF depend on the domain's geometry and sources, which can be from permanent magnets and windings, Fig. (2.2a) and (2.2b) illustrate the elementary blocks used for reluctance network in 2-D problems in Cartesian and cylindrical frames, while Fig. (2.3) illustrates the magnet's element in a reluctance network with two possible ways. In the first one the remanent flux is taken into consideration by adding a parallel flux source to the magnet's reluctance and in the second one a magneto-motive force is added in series to the magnets reluctance.

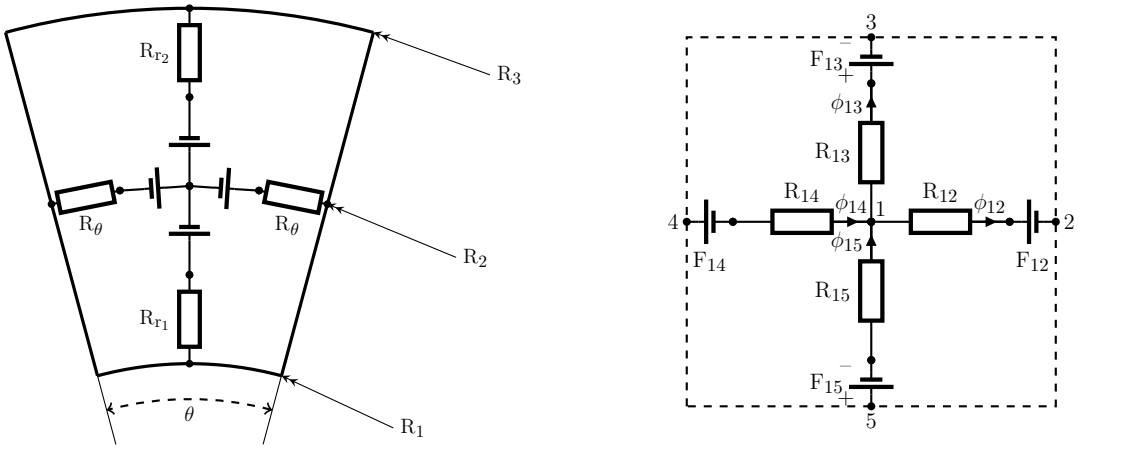

(a) Cylindrical bidirectional reluctances

(b) Rectangular bidirectional reluctances

Fig. 2.2: Representation of an elementary block

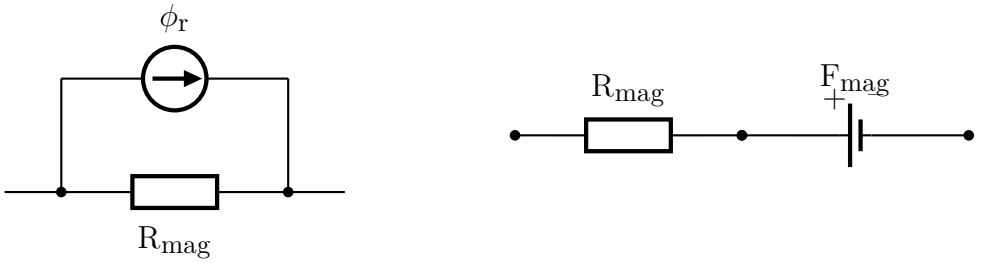

Fig. 2.3: Equivalent reluctant circuit of a magnet

In order to develop this reluctance network some assumptions have to be made; lets suppose that for an elementary volume, the magnetic flux lines are parallel and have the same amplitude, can be represented by one vector and the potential distribution is

uniform on every surface perpendicular to the magnetic flux vector, as illustrated in Fig. 2.4. Under these assumption , the magnetic flux can be written in function of the magnetic scalar potential as follow:

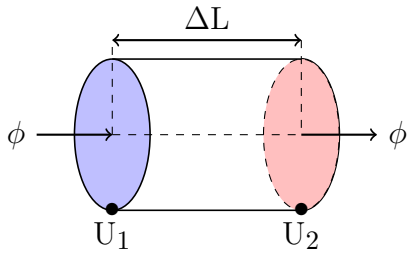

Fig. 2.4: Illustration of flux tube[75, 3]

$$\Delta \mathrm{U} = \mathrm{R}\phi \tag{2.1}$$

The expression of reluctance **R** is achieved through the simplification of Maxwell's equation with the help of previous assumptions and can be obtained using the equation below, more details about the main steps to achieve equation (2.2) and excitation computation from permanent magnet and coils are given in [76].

$$\mathrm{R} = \iiint_{\mathrm{V}} \frac{\partial \mathrm{l}}{\mu_0 \boldsymbol{\mu_r}\, \partial \mathrm{S}} \tag{2.2}$$

where $\boldsymbol{\mu_r}$ is the relative magnetic permeability, which can present a non-linear behavior depending on the thermal or/and the magnetic state of the considered volume. As a general way to formulate the reluctance network governing equations; the node equation of the central elementary block presented in Fig. (2.2) will be written by making an analogy with electrical circuit and using the equation (2.1) :

$$\begin{cases} \sum_{\mathrm{j}=2}^{5} \phi_{1\mathrm{j}} = 0 \\ \\ \dfrac{\mathrm{U_1 - U_2}}{\mathrm{R_{12}}} + \dfrac{\mathrm{U_1 - U_3}}{\mathrm{R_{13}}} + \dfrac{\mathrm{U_1 - U_4}}{\mathrm{R_{15}}} + \dfrac{\mathrm{U_1 - U_2}}{\mathrm{R_{15}}} = \dfrac{\mathrm{F_{12}}}{\mathrm{R_{12}}} + \dfrac{\mathrm{F_{13}}}{\mathrm{R_{13}}} - \dfrac{\mathrm{F_{14}}}{\mathrm{R_{14}}} - \dfrac{\mathrm{F_{15}}}{\mathrm{R_{15}}} \end{cases} \tag{2.3}$$

The magnetomotive force (MMF) is due to excitation such as windings supplied by a current density or permanent magnets; (2.4) gives magnets MMF expression while (2.5) explains the MMF issued from windings. Where $\mathrm{R_{mag}}$ is magnet reluctance, $\mathrm{Br_{mag}}$ its remanent flux and $\mathrm{s_{mag}}$ its section. $\mathrm{J_s}$ is the current density in the and S is the winding surface.

$$\mathrm{MMF_{mag}} = \frac{\mathrm{R_{mag}\ Br_{mag}}}{\mathrm{s_{mag}}} \tag{2.4}$$

$$\mathrm{MMF_{wind}} = \mathrm{I_{total}} = \int \mathrm{J_s}\ \mathrm{ds} \tag{2.5}$$

In general if a node **i** is connected to adjacent node **j** via $\mathbf{R_{ij}}$ reluctances, the governing equation will be written as:

$$\mathrm{U_i} \sum_{\mathrm{j}=\mathrm{n_1}}^{\mathrm{n_2}} \mathrm{P_{ij}} - \sum_{\mathrm{j}=\mathrm{n_1}}^{\mathrm{n_2}} \mathrm{U_j}\ \ \mathrm{P_{ij}} = \phi_{\mathrm{ext}} \tag{2.6}$$

In a general matter and for a multi node system, the equation 2.6 can be extrapoled to a matricial system and can be written as :

$$[\mathrm{P}].[\mathrm{U}] = [\phi] \tag{2.7}$$

[**P**] (**nn-m** x **nn**) is the permeances matrix; [$\boldsymbol{\phi}$] (**nn** x 1) is the source vector, elements of which are related to geometry distribution and physical properties of magnetic field sources (magnetic remanence and current density distributions) and [**U**] (**nn** x 1) is the unknowns vector (the magnetic scalar potentials in each node). **nn** is the number of total nodes in the reluctance network and **m** is the number of nodes located in the sliding surface positioned in the air-gap. The **m** missing equation in the matrix system will be provided by the air gap modeling method, which will be discussed in section 2.5.

In a radial field machine, the computation of the two reluctances $\mathrm{R_r}$ and R_θ, which are respectively the radial and circumferential magnetic reluctances, is done on a cylinder portion located between two radii (an outer one $\mathrm{R_3}$ and an inner one $\mathrm{R_1}$, $\mathrm{R_2}$ is the mean value of the two last radii), with an angular aperture equal to θ, $\mathrm{L_a}$ is the machine active length and μ_r is the relative permeability of the corresponding region. The reluctance formulation is given by (2.8).

$$\begin{cases} \mathrm{R}_{\mathrm{r}_1} = \log\left(\dfrac{\mathrm{R_2}}{\mathrm{R_1}}\right)\dfrac{1}{\mu_0\mu_\mathrm{r}\theta\mathrm{L_a}} \\ \mathrm{R}_{\mathrm{r}_2} = \log\left(\dfrac{\mathrm{R_3}}{\mathrm{R_2}}\right)\dfrac{1}{\mu_0\mu_\mathrm{r}\theta\mathrm{L_a}} \\ \mathrm{R}_\theta = \dfrac{\theta}{2\mu_0\mu_\mathrm{r}\mathrm{L_a}\log\left(\dfrac{\mathrm{R_3}}{\mathrm{R_1}}\right)} \end{cases} \tag{2.8}$$

2.2 Taking into consideration the non-linearity of soft magnetic materials

Unfortunately, one must not only overcome the difficulties of solving mathematically Maxwell's equation in order to compute the electromagnetic field distribution, but also the non-linearity of magnetic iron sheets can harden the study case and must be taken into consideration if needed. In fact, if the magnetic field in the machine is relatively low, the assumption of linear B(H) curve will not highly affect the results accuracy such in [3, 4] where the difference between the results obtained using a non-linear B(H) curve and linear one is neglected because of low or medium magnetic field. As an example, figure 2.5 illustrates the magnetic characteristics of M330-30A steel sheet, where its non-linear behavior can be countered using iterative methods dedicated for this type of problems such as Newton-Raphson method or fixed point one [77], which will be detailed further in this section.

In order to implement and solve mathematically the system, the B(H) curve is needed and can be approached using one of this techniques:

1. Analytical expression : such as the expression given below, where $\mathbf{B_s}$ is the saturation magnetic field density, $\mathbf{mu_r}$ is the initial relative and **a** is a knee control parameter localized in the interval]0,1[:

$$\begin{cases} \mathrm{B(H)} = \mu_0 + \mathrm{B_s}\dfrac{\alpha_\mathrm{a} + 1 - \sqrt{(\alpha_\mathrm{a}+1)^2 - 4\alpha_\mathrm{a}(1-\mathrm{a})}}{2(1-\mathrm{a})} \\ \alpha_\mathrm{a}(\mathrm{H}) = \dfrac{\mu_0(\mu_\mathrm{r}-1)\mathrm{H}}{\mathrm{B_s}} \end{cases} \tag{2.9}$$

2. Polynomial interpolation: this method can also be used, however the developer or user should be careful if the curve is approached with polynomial interpolation by using a method allowing the continuity of the first derivative at least such as cubic interpolation (Spline) and make sure that the curve is as smooth as possible[78] to assure the convergence, if the Newton-Raphson method is used for the non linear solving.

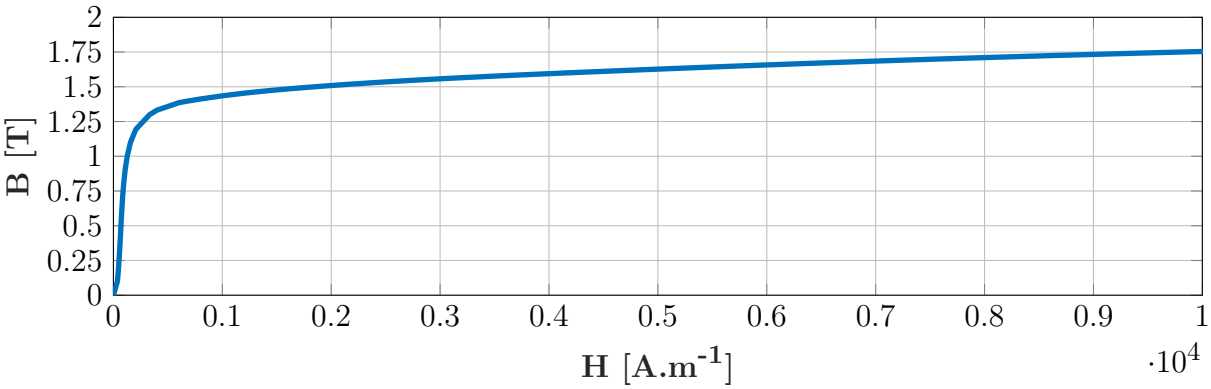

Fig. 2.5: M330-30A B(H) characteristics

Newton-Raphson algorithm can be used to achieve the solution using the non-linear B(H) curve; in fact this method is used to find the root of a function with the help of its derivative. In a general matter, the function defined for the Newton-Raphson method in a reluctance network non-linear problem is given below:

$$\mathrm{f(U)} = [\mathrm{P}][\mathrm{U}] - [\phi_\mathrm{ext}] = 0 \tag{2.10}$$

By using the Jacobian and an initial guess, which can be the solution for the magnetic system under the assumption of linear characteristics of B(H) curve, the iterative process is described as follow, where $\phi_{\mathrm{n+1}}$ and $\mathrm{P_{n+1}}$ are actualized through the potential vector $\mathrm{U_n}$:

1. **Initial solution** $\mathrm{n} = 0$; $[\mathrm{U_0}] = [\phi_0][\mathrm{P_0}]^{-1}$
2. **Compute the magnetic field in the non-linear branches** $\mathrm{mu_{nonlin}} = \mathrm{f_1(U_n)}$
3. **Actualize the permanence matrix** $\mathrm{P_{n+1}} = \mathrm{f_2(U_n)}$ **and excitation vector** $\phi_{\mathrm{n+1}} = \mathrm{f_3(U_n)}$
4. **Compute the new solution** $\mathrm{U_{n+1}} = \mathrm{U_n} - [\mathrm{J_f}]^{-1}[\mathrm{f(U_n)}]$

5. **Compute the error** $\mathrm{Err_n} = \dfrac{|\mathrm{U_{n+1}} - \mathrm{U_n}|}{|\mathrm{U_n}|}$

6. $\mathrm{Err_n}$ **satisfied?, yes : stop, otherwise go to 2** $\mathrm{n} = \mathrm{n} + 1$

The difficult task in this type of method for non-linear resolution is the evaluation of Jacobian matrix, since the system's convergence depends highly on it and can be tough to implement. Although that the Jacobian can be computed numerically, the user must be sure that it will not be the consequence of numerical error and thus maybe the divergence of non-linear resolution algorithm. For those reasons the fixed point method which is an iterative method also has been implemented; with a small difference between it and the Newton-Raphson method for the calculation of the new potential vector, in which the fourth step is replaced by the equation below:

$$[\mathrm{U_{n+1}}] = [\phi_{\mathrm{n+1}}][\mathrm{P_{n+1}}]^{-1} \tag{2.11}$$

The general description of non-linear resolution can be found below in figure (2.6)

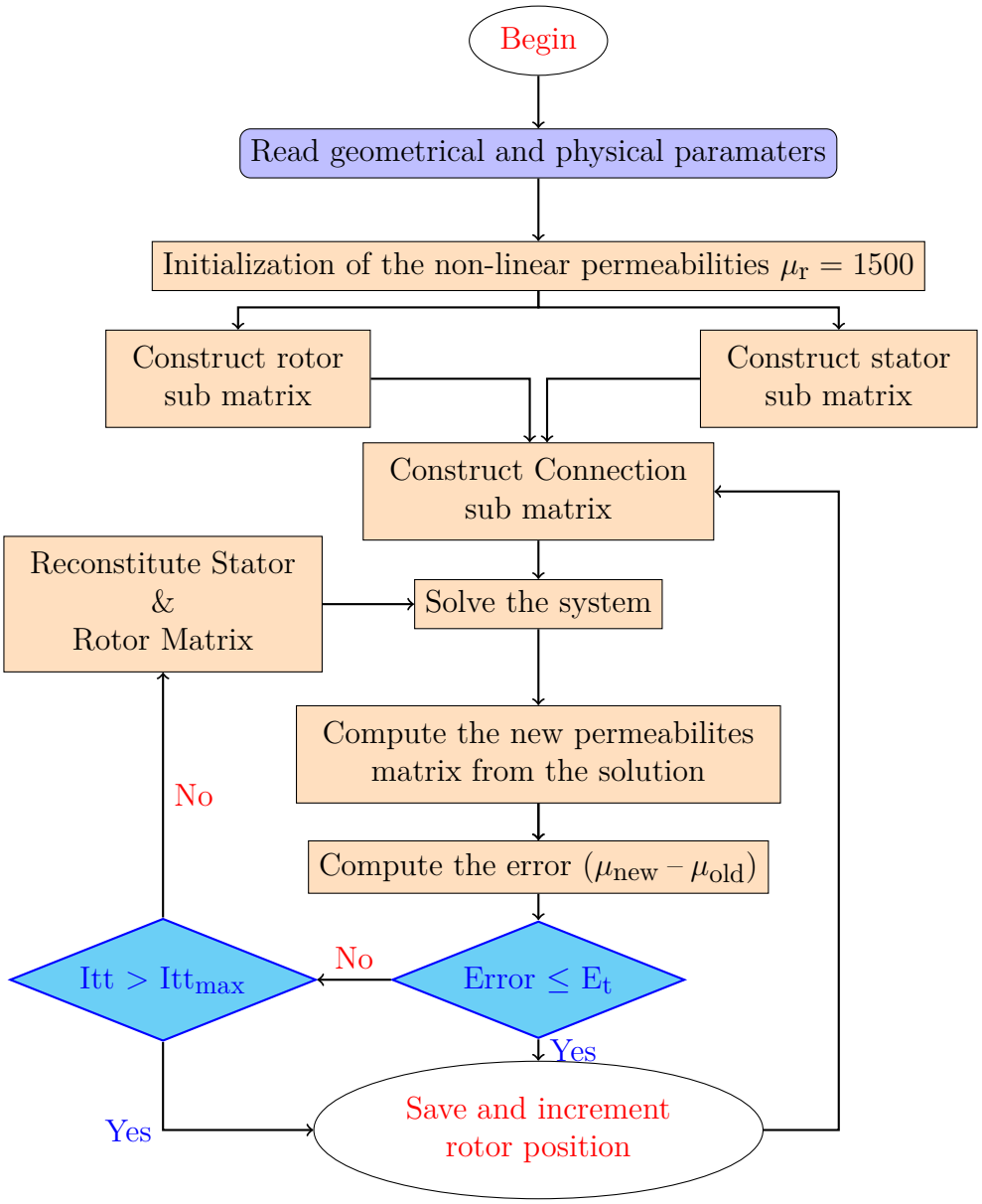

Fig. 2.6: Algorithm's simplified diagram

2.2.1 Electromagnetic torque computation

In general, two main methods are used to compute the electromagnetic torque in electrical machine problems. The first consists on using virtual work theorem and computing the effort, which can be a force or torque, by computing the co-energy derivative in the domain with respect to the displacement **P**; which is the some of co-energies derivative in each sub-domain (reluctance in our case) using equation(2.12). This method is useful in reluctances network, since it doesn't require both component of magnetic field (H_t and B_n), which mean in certain cases the air-gap can be modeled by only unidirectional reluctances such as in[76].

$$\begin{cases} W' = \int\limits_V \int H \, \partial B \, \partial V \\ \\ \overrightarrow{F} = \dfrac{\partial W'}{\partial \overrightarrow{P}} \end{cases} \tag{2.12}$$

The second method consists on using Maxwell's stress tensor, which need a good estimation of both components of magnetic field. The two components, normal and tangential of the stress applied are given by set of equations below:

$$\begin{cases} \overrightarrow{F} = \oint\limits_S \left((\overrightarrow{B}\,\overrightarrow{n})\,\overrightarrow{H} - \dfrac{\overrightarrow{H}\,\overrightarrow{B}}{2\mu_0}\,\overrightarrow{n} \right) ds \\ \\ \overrightarrow{F_n} = \dfrac{1}{2}(H_n B_n - H_t B_t)\,\overrightarrow{n} \\ \\ \overrightarrow{F_t} = H_t B_n \,\overrightarrow{t} \end{cases} \tag{2.13}$$

For more information and detail about the electromagnetic force computation in special, or local force computation in general, work such as [79] explains the methodology and different methods existing for its computation. In our case the electromagnetic torque will be computed at the sliding surface located at the mean radius of air-gap using Maxwell stress tensor.

2.3 Thermal modeling of electrical machines

As said in the introduction of this chapter; one can not conceive or optimize an electrical machine without giving a look at its thermal response, since the life time of a winding depends highly on the materials used for insulation and winding's hottest spot. Which will dramatically decrease winding's life time by half for each 10[°C] added over the allowed maximal temperature[80, 81], table2.1 summarizes the acceptable hottest spot for each insulation class.

Insulation class	A	B	F	H
Hottest spot	105	130	155	180

Table 2.1: Allowed hottest spot for each insulation class

In order to analyze the thermal behavior of electrical machines: lumped solution will be chosen as a modeling method all over this report, which presents the advantages of good accuracy with an acceptable computation time[62, 82, 83, 79, 84].
As the reluctance network, an equivalence is made between the thermal circuit and the electrical one, where the heat flow is the current and the nodal temperature is the voltage. In a brief way, each element in the machine is assigned to a thermal resistance and capacitor depending on the material constituting it as shown in fig.2.8, its geometrical parameters and the transfer mode (convection or conduction).

$$-[\mathrm{C}]\frac{\partial[\mathrm{T}]}{\partial \mathrm{t}} = [\mathrm{P}][\mathrm{T}] - [\mathrm{E}] \tag{2.14}$$

In order to achieve lumped thermal equations, some explanations and assumptions must be done for each sub-volume of domain such as:

1. Volumes are considered rigid.
2. The heat flux lines are parallel and constant.
3. The temperature distribution is uniform on each surface perpondeculare to heat flux lines as can be seen in Fig. (2.7).

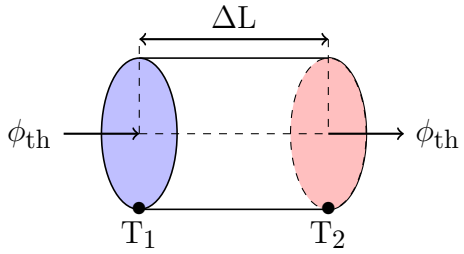

Fig. 2.7: Illustration of thermal flux tube

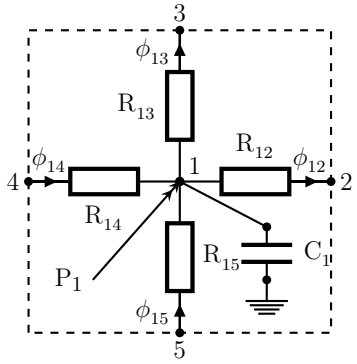

Fig. 2.8: Representation of an elementary block for transient thermal computation

Under the previous assumptions and by the help of thermodynamics laws, the general heat equation can be written as :

$$\begin{cases} -\rho \mathrm{C}\dfrac{\partial \mathrm{T}}{\partial \mathrm{t}} = \mathrm{div}(\mathrm{k}\ \overrightarrow{\mathrm{grad}(\mathrm{T})}) + \mathrm{P} \quad = \nabla^2(\mathrm{T}) + \mathrm{P} \\ \Delta \mathrm{T} = \mathrm{R_{th}}\phi \end{cases} \tag{2.15}$$

Where $\boldsymbol{\rho}$ is the material density, **C** its associated heat capacity and $\mathbf{R_{th}}$ is the thermal resistor; knowing that its expression depends on heat transfer mode, which can be one of these three[82]:

Conduction This type of heat flow is present in solids where the transfer is assured by electrons movement and microscopic collisions of particles, its associated thermal resistor is described by equation below, where **k** is the conduction transfer coefficient:

$$\mathrm{R_{cond}} = \frac{\mathrm{L}}{\mathrm{kS}} \tag{2.16}$$

Convection It occurs when heat flows between solid and fluid, in the case of electrical machine this can represent the heat flow between stator and rotor through the air-gap or stator and external medium, which is caused by the fluid movement by consequence of its temperature raise. The expression governing the computation of thermal convection resistor is:

$$\mathrm{R_{cond}} = \frac{1}{\mathrm{hS}} \tag{2.17}$$

Where **h** is the convection coefficient and **S** is convection exchange section.

Radiation This type of transfer is generally neglected, and will be during this report, in preliminary sizing studies of electrical machine; since the study domain is relatively small and at low temperature.

The most difficult part in thermal modeling is the determination of heat transfer coefficient: the main problem is not the mathematical resolution, but it is about the material's system thermal characteristics (heat coefficients). The determination of such coefficients will be discussed further in this document. However, the mathematical formulation needed to solve such a system must be treated, for which the equation in central node of the sub-volume will be written in equation (2.18), as illustrated in Fig. 2.7, where the heat flow is assumed to be bidirectional.

$$\begin{cases} \sum_{\mathrm{j}=2}^{5} \phi_{1\mathrm{j}} = 0 \\ \\ \dfrac{\mathrm{T_1 - T_2}}{\mathrm{R_{12}}} + \dfrac{\mathrm{T_1 - T_3}}{\mathrm{R_{13}}} + \dfrac{\mathrm{T_1 - T_4}}{\mathrm{R_{15}}} + \dfrac{\mathrm{T_1 - T_2}}{\mathrm{R_{15}}} + \mathrm{P_1} = -\rho_1 \mathrm{C_1} \dfrac{\partial \mathrm{T_1}}{\partial \mathrm{t}} \end{cases} \tag{2.18}$$

The previous equation can be generalized and extrapolated for a system of **nn** nodes as:

$$[\mathrm{P}][\mathrm{T}] - [\phi_{\mathrm{ext}}] = -[\rho \mathrm{C}] \frac{\partial [\mathrm{T}]}{\partial \mathrm{t}} \tag{2.19}$$

By the help of Euler's numerical method, the solution can be found as :

$$[\Delta \mathrm{t}[\mathrm{P}] + [\rho \mathrm{C}]]\,[\mathrm{T_{n+1}}] = -[\rho \mathrm{C}][\mathrm{T_n}] + [\phi_{\mathrm{ext}}]\Delta \mathrm{t} \tag{2.20}$$

[**P**] (**nn-m** x **nn**) is the thermal permeances matrix; [$\boldsymbol{\phi}_{\mathbf{ext}}$] (**nn** x 1) is the source vector, elements of which are related to geometry and thermal physical properties distribution (losses distribution and boundary conditions; convection or imposed temperature), [**T**] (**nn** x 1) is the unknowns vector at each time step (the temperature at each node) and

[$\boldsymbol{\rho}$**C**] (**nn** x **nn**) is a diagonal matrix containing the value of heat capacity of each sub-volumes. **nn** is the number of total nodes in the reluctance network and **m** is the number of nodes located in the sliding surface positioned in the air-gap. The **m** missing equation in the matrix system will be provided by the air gap modeling method, which will be discussed in section 2.5.

2.3.1 Convection heat coefficient computation

The transition surfaces between a solid and fluid such as air-gap/stator, air-gap/rotor, stator/ambient air and rotor/ambient air will have convection as dominant heat transfer mode for the general case of electrical machines, characterized by a convection coefficient; which depends on surface section, its state (rough or smooth) and the nature of fluid flow (forced or natural)[85]. Since rotor speed influences air flow in the air-gap region, which can be assimilated to an annulus confined between two cylinders, where one is static and the other is mobile. Finite elements CFD/thermal analysis can be used to estimate Nusselt number and thus heat transfer coefficient by convection accurately. However, reduction of computation time in early stages of design is important and thus an analytical accurate expression of heat coefficient will be welcomed and CFD/FEM computation will be avoided, since it is time consuming. Fortunately, Many works have been interested to air-gap convection coefficient correlation in electrical machines through experimental measurement[86, 87, 88, 89], for which the definition of dimensionless numbers is needed such as:

Taylor Number : Taylor studied the air instability in an annulus confined between two cylinders, in which one is on rotation. The author defined a critical number from which vortexes start to appear and affect highly the heat transfer coefficient[90], its expression is given in equation (2.21), where $\boldsymbol{\omega}$ is the rotational speed, $\mathbf{L_c}$ the characteristic length and $\boldsymbol{\nu}$ the kinematic viscosity.

$$\mathrm{T_a} = \frac{4\omega^2 \mathrm{L_c^4}}{\nu^2} \tag{2.21}$$

Nusselt Number : It represents the fraction between the heat transfer by convection and conduction. If this number relatively big, the heat transfer is mostly done by convection, in the contrary and when this number is close to one the transfer is done mostly by conduction, its expression is given in equation (2.22).

$$\mathrm{N_u} = \frac{\mathrm{hL}}{\mathrm{k_f}} \tag{2.22}$$

Reynolds Number : It characterizes the flow and its nature (laminar, transient turbulent), which presents the fraction between inertia forces and viscous ones, where **V** is the fluid characteristic speed.

$$\mathrm{R_e} = \frac{\mathrm{VL_c}}{\nu} \tag{2.23}$$

Many works were done to correlate convection coefficient through these dimensionless numbers, next paragraph summarizes some formulas retained to compute convection heat coefficient in electrical machines air-gap:

Becker and Kaye To study the air-gap heat transfer in electrical machine, author in [87] realized series of tests on an annulus confined between a static cooled cylinder and a heated rotating one, both cylinders are characterized by smooth exchange surfaces. Authors obtained results for different configurations, with axial flow and without it, of Nusselt's number depending on four states of air flow: (1)Laminar flow, (2)Laminar with Taylor vortexes flow, (3)Turbulent, (4)Turbulent flow with taylor vortexes flow. Without forced axial flow, the correlation between Nusselt number and modified Taylor one, is given in equation (2.24). However in axial flow case, author presented only graphs of Nusselt number dependency on Taylor and Reynold numbers, a correlation will be given further in this section.

$$N_u = 0.409 \times T_{a_m}^{0.241} - 137 \times T_{a_m}^{-0.75} \tag{2.24}$$

Where $\mathbf{T_{a_m}}$ is the modified Taylor number,$\mathbf{E}$ is the air-gap height, $\mathbf{R_{1,2}}$ are respectively inner and outer annulus radii and $\mathbf{F_g}$ is the geometrical factor and can be computed by the help of equation (2.25).

$$\begin{cases} T_{a_m} = \dfrac{\omega^2 R_m e^3}{\nu^2} \dfrac{1}{F_g} \\ R_m = \dfrac{E}{\log\left(\dfrac{R_2}{R_1}\right)} \\ F_g = \dfrac{\pi^4}{1697P} \dfrac{R_1 + R_2}{2R_1} \\ P = 0.0571(1 - \dfrac{0.652E}{R_1}) + 0.00056(1 - \dfrac{0.652E}{R_1})^{-1} \end{cases} \tag{2.25}$$

For the configuration where the axial flow is null, author noticed for all Taylor numbers under 1700, which is defined as Taylor critical number $\mathbf{T_{a_c}}$, heat transfer is dominated by pure conduction since Nusselt number is around the value 2 ($N_u \approx 2$), which corresponds to laminar flow of air. For this configuration, authors's results showed good agreement with previous works such as [86, 88]. Above the critical Taylor number vortexes start to appear and the heat transfer is increased with it and can be approximated through the correlation given in equation (2.24).

M.Bouafia Author in [89] studied the same case as the previous with addition to rough surface case. Results obtained in [89] in the case of smooth surface showed good correlation in general with ones obtained in [87, 88, 86], author found the same correlation given in equation (2.24), as can be seen in Fig. (2.9).

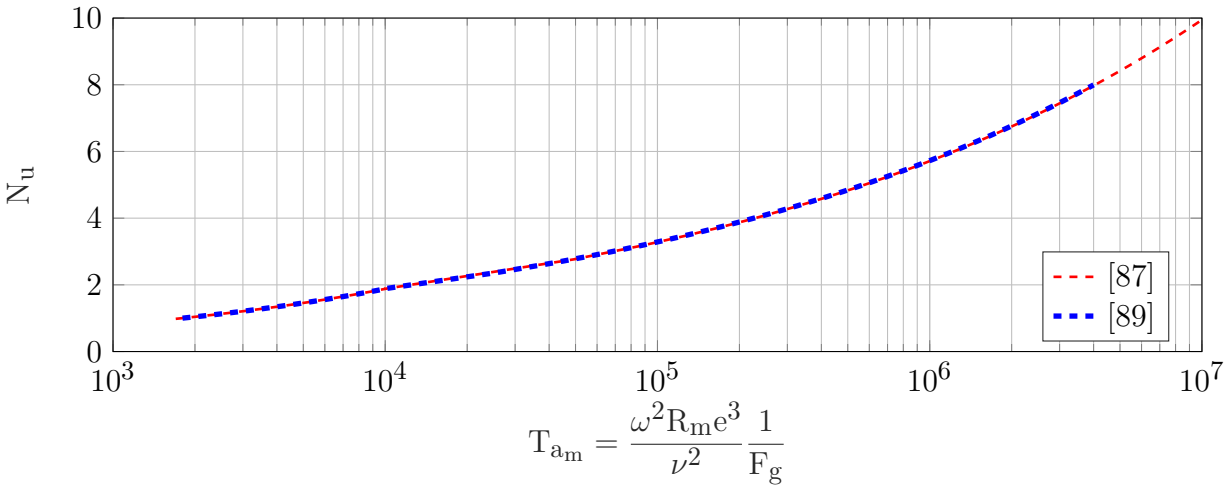

Fig. 2.9: Nusselt number dependency on Taylor modified number

However, in the situation of rough surface author noticed difficulties to determine critical Taylor number from which air-flow becomes instable and favors convective heat transfer, which is situated around 3900 in his case. Also, a boost between 2% and 20 % of convective exchange compared to smooth surface is observed with the dilemma of associating the air flow nature in air-gap and rough surfaces slots together. Since the air flow in the slots and in air-gap is not the same at low speed and can be separated, but becomes highly related when speed increases, which makes interpretation harder compared to smooth surface case. Two correlations are given for the case of rough surface and without axial flow depending on Taylor modified number, as given in equation (2.26).

$$\begin{cases} Nu = 0.132\ T_{a_m}^{0.3} & T_{a_m} \in [6000\ -\ 1.4 \times 10^6] \\ Nu = 0.029\ T_{a_m}^{0.4} & T_{a_m} \in [1.4 \times 10^6\ -\ 2 \times 10^7] \end{cases} \tag{2.26}$$

With axial flow presence, the determination of Nusselt number can be done through the computation of effective speed $\mathbf{V_{eff}}$ and by the aid of Reynolds numbers expressions, given in equation (2.27), where $\mathbf{V_a}$ is the axial fluid velocity, $\mathbf{R_{e_a}}$, $\mathbf{R_{e_t}}$ and $\mathbf{R_{e_{eff}}}$ are respectively axial tangential and effective Reynolds numbers and $\boldsymbol{\alpha}$ is a weight coefficient which indicate the contribution of rotation speed with respect to the axial flow.

$$\begin{cases} V_{eff} = \sqrt{V_a^2 + \alpha(\omega R_1)^2} \\ R_{e_a} = \dfrac{V_a d_h}{\nu} \\ R_{e_t} = \dfrac{\omega R_1 d_h}{\nu} \\ R_{e_{eff}} = \sqrt{R_{e_a}^2 + R_{e_t}^2} \end{cases} \tag{2.27}$$

The correlation then differs from stator and rotor, as the author noticed, where the laws used to evaluate convection coefficient for rotor and stator for smooth and rough surface are given respectively by equation (2.28) and (2.29).

$$\begin{cases} N_{u_{rot}} = 0.025 \times R_{e_{eff}}^{0.8} & R_{e_a} \in [1.1 \times 10^4\ -\ 3.1 \times 10^4] \\ N_{u_{stat}} = 0.046 \times R_{e_{eff}}^{0.7} & R_{e_t} \in [500\ -\ 3.1 \times 10^4] \end{cases} \tag{2.28}$$

$$\begin{cases} \mathrm{N_{u_{rot}}} = 0.021 \times \mathrm{R_{e_{eff}}^{0.8}} & \mathrm{R_{e_a}} \in [1.1 \times 10^4 \ - \ 3.1 \times 10^4] \\ \mathrm{N_{u_{stat}}} = 0.046 \times \mathrm{R_{e_{eff}}^{0.7}} & \mathrm{R_{e_t}} \in [500 \ - \ 3.1 \times 10^4] \end{cases} \tag{2.29}$$

In all our cases, all surfaces are supposed smooth and without axial flow, which will lead us to use mainly equations 2.24 and 2.25. Furthermore, an explanation will be given about the estimation of slot's equivalent conduction coefficient.

2.3.2 Slot's equivalent conduction coefficient

The thermal behavior depends highly on the transfers coefficients. Their estimation can be difficult for certain regions, such for the slots composed from different materials having specific thermal conductivities: copper, which is a good thermal conductor, residual air, the insulator and impregnation, which are characterized by a poor conduction factor. To take into consideration the heterogeneity, authors in [91] defined a thermal resistor depending on several factors, such as material used for insulation and quality of the impregnation, residual air quantity after it. From which an equivalent conduction coefficient is derived using slot's section $\mathbf{S_{slot}}$, perimeter $\mathbf{l_{sp}}$, interior area $\mathbf{A_{slot}}$ and filling factor $\mathbf{k_f}$. Equations (2.30, 2.31) and 2.32 illustrate the computation of the slot's thermal resistor and its corresponding coefficient:

$$\mathrm{k_{equi}} = 0.1076 \ \mathrm{k_f} + 0.029967 \tag{2.30}$$

$$\mathrm{R_{slot}} = \mathrm{t_{eq}} \ (\mathrm{k_{equi}} \ \mathrm{A_{slot}})^{-1} \tag{2.31}$$

$$\mathrm{t_{eq}} = (1 - \mathrm{k_f}) \ \mathrm{S_{slot}} \ \mathrm{l_{sp}^{-1}} \tag{2.32}$$

A second method consists of representing all the materials composing the slot (copper, insulator, residual air and impregnation) as can be seen in Fig. (2.10), which adds more complexity to the modeling processes. Since the impregnation processes has random behavior adding to that the difficulty to approximate residual air left after the impregnation processes, knowing that with this method the system to solve will increase dramatically compared to homogeneous material method, since the mesh or decomposition of geometry must be as fine as possible in order to respect geometrical material distribution.

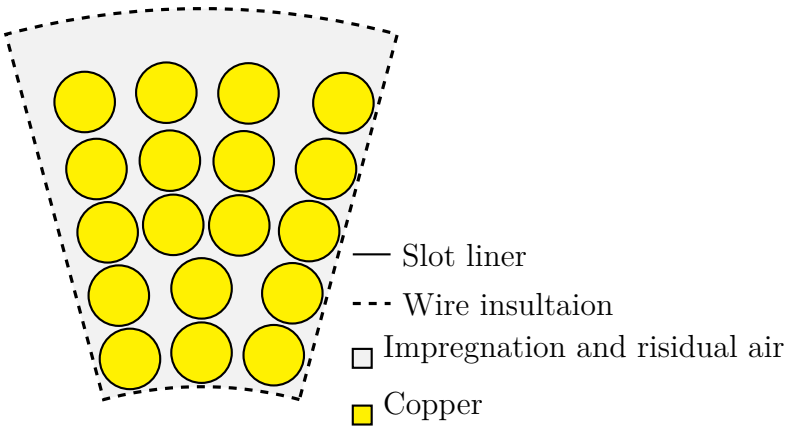

Fig. 2.10: A way to represent the slot for thermal computation

2.4 Non-linear thermal behavior of copper

Some materials used for the manufacturing of electrical machines have non-linear thermal behavior, the most interesting one is copper [1], since most of losses are generated in windings for relative low and medium speed machines. For these reasons, copper electrical resistivity characteristic versus temperature will be needed. Work in [92] gathered multiple copper, gold and silver resistivity measurement through the bibliography for wide range of temperature [1K - 1700K]. We will be interested on thermal characteristics of copper located in the interval [20°C - 200°C], since in electrical machines, it is not common to find an application requiring an operating point under thermal constraints outside of this range. The results found in [92] showed that copper conductivity increases with a linear law with respect to the temperature, which can be seen in Fig. (2.11). From which a linear equation can be derived given in equation (2.33), where $\boldsymbol{\rho_{cu_{20}}}$ is copper resistivity at 20[°C] equal to 1.6×10^{-8} [Ω.m] and $\boldsymbol{\alpha_{cu}}$ is the electrical resistivity expansion coefficient equal to 0.004 [$\Omega.m.K^{-1}$].

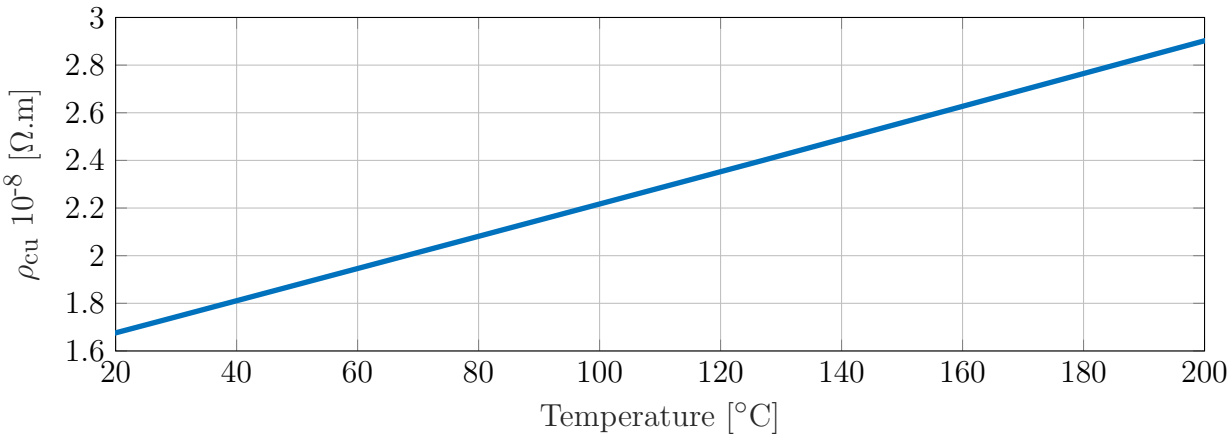

Fig. 2.11: Copper resistivity dependency on the temperature[92]

$$\rho_{cu}(T) = \rho_{cu_{20}}(1 + \alpha_{cu}(T - 20)); \tag{2.33}$$

The last information given about the thermal behavior imposes its consideration, indeed and since Joule losses depends linearly to the resistance and thus to copper resistivity. For this reason the estimation of copper losses using its corresponding resistivity at 20[°C] will be underestimated by 40%, which clearly will lead to totally false estimation of machine's temperature distribution and thus thermal undersizing. The method used to take into consideration this behavior is similar to the magnetic one, where Joule losses are corrected at each time through temperature computation as explained and exposed in Fig. (2.12).

[1] from the thermal point of view

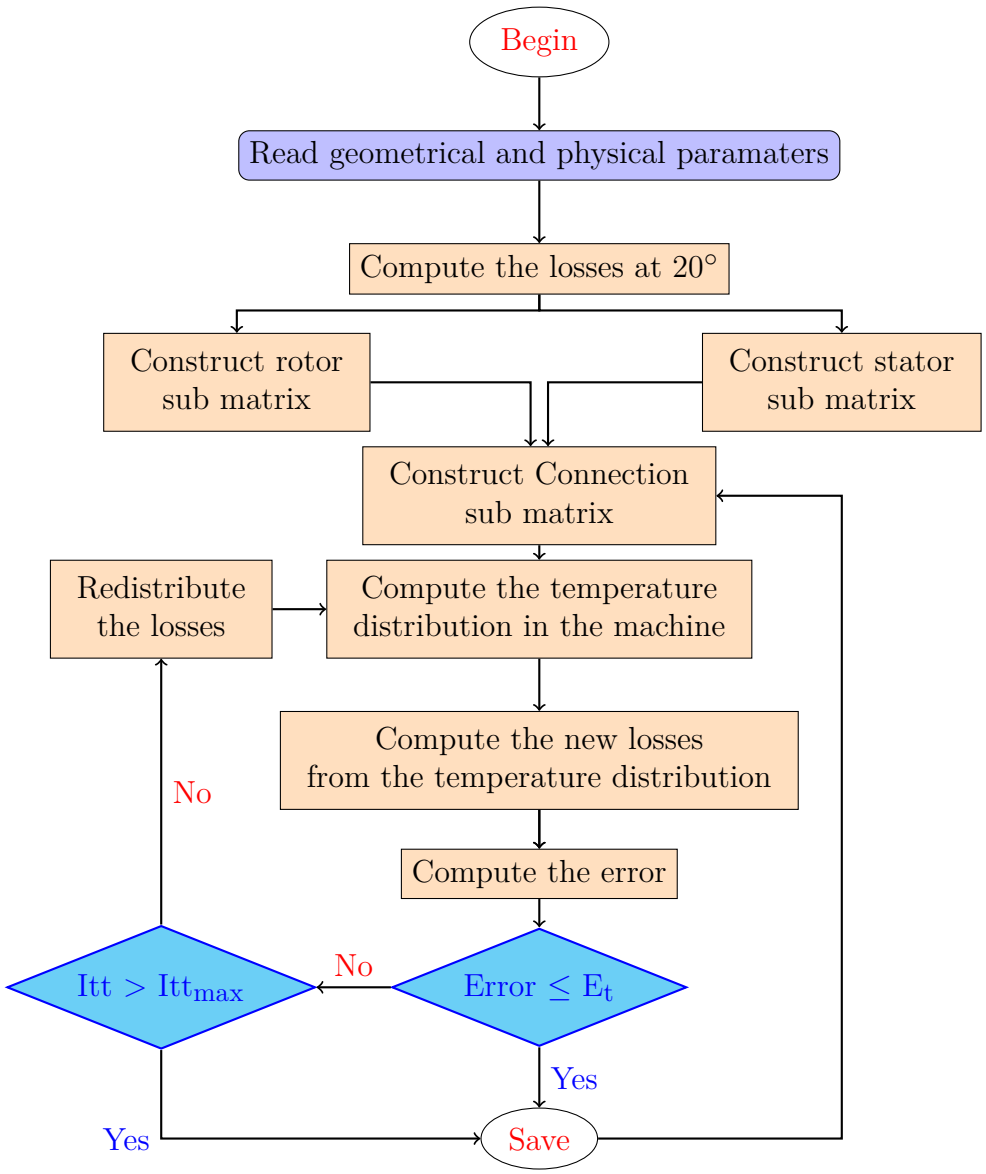

Fig. 2.12: Algorithm's simplified diagram for thermal computation

2.5 Air-gap modeling

The air-gap modeling is relatively a hard task to achieve, since the rotor discretization and the stator are generally not the same [93], one of these several modeling approaches presented bellow can be considered for the stator's and rotor's nodes connection:

1. **Analytical solution**: This solution can eliminate easily the connectivity problem between the stator and the rotor, in fact the air-gap is modeled analytically by solving the partial differential equation resulting from Maxwell's equations using the scalar magnetic potential formulation or from the heat equation, considering only the transfer by conduction, given in the equation (2.34):

$$\nabla^2 U = 0; \quad \nabla^2 T = 0 \tag{2.34}$$

After finding the Laplacian equation solution, this last is written as a Fourier sum, under certain assumptions, and used for a strong coupling between the two nodal

networks by assuring flux and the potential continuity at the transition surfaces [94]; air-gap/stator and air-gap/rotor. Although this solution offers a total independence for discretization and gives an easy way to take into consideration the movement, it comes with its drawbacks, which are:

Badly scaled Matrix : First the flux and potential continuity equations give a bad shape to the system's matrix. Resulting in a denser matrix compared to the global matrix system of a pure nodal network and consequently the program will take more time to solve the matricial equation of the system.

Limited maximum harmonic number : Theoretically the maximum harmonic number is infinite, but in reality the computer has its limitation. Whereas, the largest and smallest finite floating-point number are defined, depending on the machine's characteristics. However, since the studied machine is a radial flux one, the most suitable frame to solve the previous equation is a cylindrical one and under the assumption of a bidirectional magnetic field, the previous partial differential equation becomes:

$$\frac{\partial^2 \mathrm{U}}{\partial \mathrm{r}^2} + \frac{\partial^2 \mathrm{U}}{\mathrm{r}^2 \partial \theta^2} + \frac{\partial \mathrm{U}}{\mathrm{r} \partial \mathrm{r}} = 0; \qquad \frac{\partial^2 \mathrm{T}}{\partial \mathrm{r}^2} + \frac{\partial^2 \mathrm{T}}{\mathrm{r}^2 \partial \theta^2} + \frac{\partial \mathrm{T}}{\mathrm{r} \partial \mathrm{r}} = 0 \tag{2.35}$$

The solutions are given in equations (2.36 and 2.37), while **n** is the harmonic rank and **p** is the number of magnetic/thermal periods of the machine in 360° mechanical angle:

$$\mathrm{U}(\mathrm{r}, \theta) = \sum_{1}^{+\infty} \begin{cases} (\mathrm{a_n r^{np}} + \mathrm{b_n r^{-np}}) \cos(\mathrm{np}\theta) \\ + \\ (\mathrm{c_n r^{np}} + \mathrm{d_n r^{-np}}) \sin(\mathrm{np}\theta) \end{cases} \tag{2.36}$$

$$\mathrm{T}(\mathrm{r}, \theta) = \mathrm{T_0} + \mathrm{T_1} \log(\mathrm{r}) + \sum_{1}^{+\infty} \begin{cases} (\mathrm{a_n r^{np}} + \mathrm{b_n r^{-np}}) \cos(\mathrm{np}\theta) \\ + \\ (\mathrm{c_n r^{np}} + \mathrm{d_n r^{-np}}) \sin(\mathrm{np}\theta) \end{cases} \tag{2.37}$$

It is clear that the maximum harmonic number, which can be handled by the computer, depends highly on the machine's geometry: its radii and the number of repetitions on a mechanical period. Depending on the simplicity of the geometry, previous solutions formula can be changed in order to avoid numerical problems, as given in equations (2.38 and 2.39). Using this new formula, the direct dependency of solution's stability and machine' radii is avoided, which allows the study of relatively small or big machines through an analytical solution.

$$\mathrm{U}(\mathrm{r}, \theta) = \sum_{1}^{+\infty} \begin{cases} \left(\mathrm{a_n} \dfrac{\mathrm{r}}{\mathrm{R_0}}^{\mathrm{np}} + \mathrm{b_n} \dfrac{\mathrm{r}}{\mathrm{R_0}}^{-\mathrm{np}}\right) \cos(\mathrm{np}\theta) \\ + \\ \left(\mathrm{c_n} \dfrac{\mathrm{r}}{\mathrm{R_0}}^{\mathrm{np}} + \mathrm{d_n} \dfrac{\mathrm{r}}{\mathrm{R_0}}^{-\mathrm{np}}\right) \sin(\mathrm{np}\theta) \end{cases} \tag{2.38}$$

$$\mathrm{T}(\mathrm{r},\theta) = \mathrm{T}_0 + \mathrm{T}_1 \log(\mathrm{r}) + \sum_{1}^{+\infty} \begin{cases} \left(\mathrm{a_n} \dfrac{\mathrm{r}}{\mathrm{R}_0}^{\mathrm{np}} + \mathrm{b_n} \dfrac{\mathrm{r}}{\mathrm{R}_0}^{-\mathrm{np}}\right) \cos(\mathrm{np}\theta) \\ + \\ \left(\mathrm{c_n} \dfrac{\mathrm{r}}{\mathrm{R}_0}^{\mathrm{np}} + \mathrm{d_n} \dfrac{\mathrm{r}}{\mathrm{R}_0}^{-\mathrm{np}}\right) \sin(\mathrm{np}\theta) \end{cases} \tag{2.39}$$

2. **Variable nodal network**:The easiest and classical solution consists of a variable nodal network depending on the relative position between the moving armature and the static one. Although this method seems suitable for this case of study [95, 96, 76], but it comes with its drawbacks too, which can be listed below:

   Size variation of the unknown vector Let's remind that the objective here is to find the potential at each node, so we are looking for a vector and thus a memory allocation must be done to store it for post-processing. If the vector size is constant, it will be easy to allocate it, since its size is known for every rotor relative position. However, the number of nodes in the air-gap depends on the relative position between the rotor and the stator and can change from a rotor step to another, which will affect the solution vector's size and thus the global matrix size. This will expose a problem for the post-processing; indeed, to avoid this at each step the air-gap matrix must be stored in memory, since it is needed to compute the flux through all the branches, which will slow down the program and requires more memory compared to other methods.

   b. Small exchange surfaces As the analytical solution, the variable nodal network can cause some numerical problems. It uses the cross section between two blocks to determine the magnetic or thermal resistor connecting them. However if this surface is too small, it can be the consequence of a relative big reluctance which will disturb the matrix stability and thus the results accuracy.

3. **Node interpolation in the sliding region**: This method uses nodal interpolation functions to take into consideration the continuity of potential and flux density at the surface of the sliding region, which is the surface separating the moving parts from the static one. Let's assume a rotor node located in the sliding surface is sandwiched between two nodes associated to the stator having $\boldsymbol{\theta_r}$, $\boldsymbol{\theta_{s1}}$ and $\boldsymbol{\theta_{s2}}$ as circumferential coordinates $\mathbf{U_r}$, $\mathbf{U_{s1}}$ and $\mathbf{U_{s2}}$ as nodal scalar potential respectively, as can be seen in figure (2.13). The potential located in the rotor can be written in function of the two placed in the stator by using first order Lagrange interpolation as in (2.40): the same analogy can be made between the magnetic circuit presented in figure (2.13) and a thermal one.

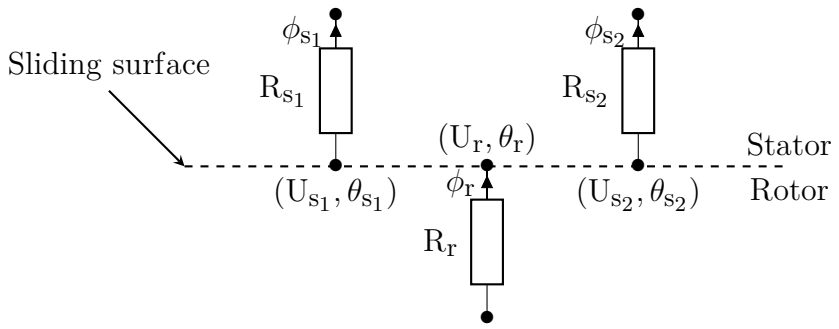

Fig. 2.13: Scalar potential interpolation in the sliding surface

$$U_r = \frac{(\theta_r - \theta_{s1})}{(\theta_{s2} - \theta_{s1})} U_{s2} + \frac{(\theta_r - \theta_{s2})}{(\theta_{s1} - \theta_{s2})} U_{s1}; \quad T_r = \frac{(\theta_r - \theta_{s1})}{(\theta_{s2} - \theta_{s1})} T_{s2} + \frac{(\theta_r - \theta_{s2})}{(\theta_{s1} - \theta_{s2})} T_{s1} \quad (2.40)$$

With the previous equation we assume that the potential has a linear shape between two successive nodes. This assures the equality of the scalar potential in the sliding surface, which will provide the missing $\mathbf{M_{rt}}$ equations for the rotor. In general the previous equation can be generalized and written in a matricial system as fellow:

$$[U_r] - [M_{interp_{strt}}][U_s] = 0; \quad [T_r] - [M_{interp_{strt}}][T_s] = 0 \quad (2.41)$$

With $[\mathbf{U_r}]$ $[\mathbf{U_s}]$ are the vectors containing rotor and stator potentials corresponding to the nodes located at the sliding surfaces and $[\mathbf{M_{interp_{strt}}}]$ is the interpolation matrix. To satisfy the second interface condition; which is the continuity of the flux density, and provide the missing $\mathbf{M_{st}}$ equation for the stator, the flux density continuity between the two reluctance networks will be assured by using the same interpolation method employed previously. In this case stator's flux density will be written in function of the rotor's one. As the previous step, let's assume that a node belonging to the stator and located in the sliding surface is sandwiched between two nodes associated to the rotor having $\boldsymbol{\theta_s}$, $\boldsymbol{\theta_{r1}}$ and $\boldsymbol{\theta_{r2}}$ as circumferential coordinates and $\mathbf{B_s}$, $\mathbf{B_{r1}}$ and $\mathbf{B_{r2}}$ as flux density respectively, which is illustrated in figure (2.14). The flux density crossing the node located in the stator can be written as a function of the two placed in the rotor by using first order Lagrange interpolation as indicated in (2.42): as the first step of coupling the same analogy can be made between the magnetic circuit presented in figure (2.14) and a thermal one.

$$B_s = \frac{(\theta_s - \theta_{r1})}{(\theta_{r2} - \theta_{r1})} B_{r2} + \frac{(\theta_s - \theta_{r2})}{(\theta_{r1} - \theta_{r2})} B_{r1}; \quad \varphi_s = \frac{(\theta_s - \theta_{r1})}{(\theta_{r2} - \theta_{r1})} \varphi_{r2} + \frac{(\theta_s - \theta_{r2})}{(\theta_{r1} - \theta_{r2})} \varphi_{r1} \quad (2.42)$$

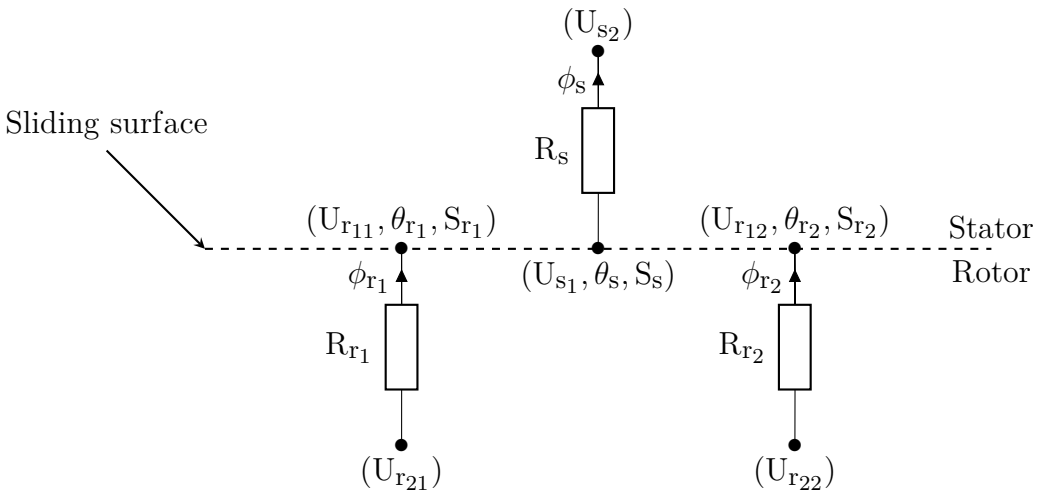

Fig. 2.14: Flux density interpolation in the sliding surface

Using the relation between the flux density and the scalar potential, which is the scalar potential difference multiplied by the permeance and divided by its cross section, given in the equation below:

$$\frac{\Delta U_s}{R_s S_s} = \frac{(\theta_s - \theta_{r1})}{(\theta_{r2} - \theta_{r1})} \frac{\Delta U_{r2}}{R_{r2} S_{r2}} + \frac{(\theta_s - \theta_{r2})}{(\theta_{r1} - \theta_{r2})} \frac{\Delta U_{r1}}{R_{r1} S_{r1}} \tag{2.43}$$

$$\frac{\Delta T_s}{R_s S_s} = \frac{(\theta_s - \theta_{r1})}{(\theta_{r2} - \theta_{r1})} \frac{\Delta T_{r2}}{R_{r2} S_{r2}} + \frac{(\theta_s - \theta_{r2})}{(\theta_{r1} - \theta_{r2})} \frac{\Delta T_{r1}}{R_{r1} S_{r1}} \tag{2.44}$$

The last equation can be transformed into matrix form:

$$[M_1][U_{s1}] - [M_1][U_{s2}] - [M_{interp_{rtst}}][U_{r1}] - [M_{interp_{rtst}}][U_{r2}] = 0 \tag{2.45}$$

$$[M_1][T_{s1}] - [M_1][T_{s2}] - [M_{interp_{rtst}}][T_{r1}] - [M_{interp_{rtst}}][T_{r2}] = 0 \tag{2.46}$$

With $[\mathbf{U_{r1}}\ ]\ [\mathbf{U_{s1}}]$ are the vectors containing rotor and stator potentials corresponding to the nodes located at the sliding surfaces and $[\mathbf{U_{r2}}\ ]\ [\mathbf{U_{s2}}\ ]$ contain the rotor and stator first scalar potential located below/above the sliding surface. $[\mathbf{M_{interp_{rtst}}}]$ is the modified interpolation matrix, in which every element is divided by the magnetic or thermal connected to and its cross section, while $[\mathbf{M_1}]$ is the matrix containing the permeance of the element divided by its cross section for each element.
It is clear hear that the movement can be taken into consideration easily, since the number of nodes is fix and problem transforms from connecting two independent networks to simply interpolating the scalar potential and the flux density at the sliding surface. Also at each line corresponding to the interpolation equation, only six elements are non-null at maximum. Furthermore, this method will be fast compared to the two previous ones, since the global matrix of the system is as sparse as possible and has a fixed node number.

2.6 Model validation

2.6.1 Magnetic model validation

In order to validate the modeling approach, the electromagnetic performances of two different topologies will be computed. The first one is a surface mounted synchronous machine as shown in figure 2.15, while the second is a spoke type permanent magnet machine. For both structures, flux through the phases[2], magnetic flux densities in the middle of air gap region and torque obtained by the developed reluctance network will be compared with those obtained with commercial software using finite elements method. The electromagnetic torque is computed at the sliding surface and using maximum torque angle and Maxwell's stress tensor. In order to validate the capability of the model to work in a wide range, two windings will be used; in machine **A** the winding is pentaphased single layered, while in machine **B** winding is threephased superposed double layered one. Table 2.2 contains the main geometric and physical parameters used to simulate the magnetic behavior of the studied machines.

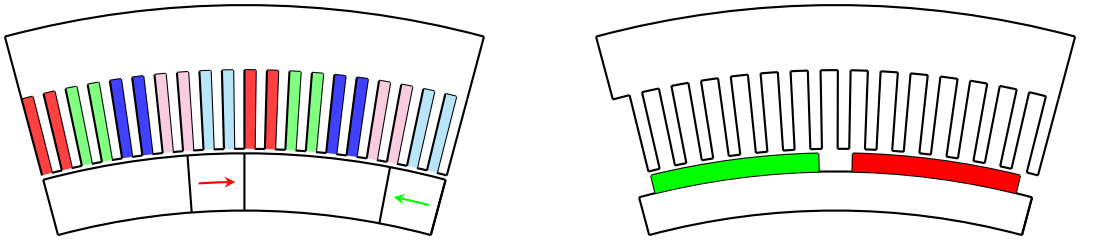

(a) Spoke type synchronous machine (b) Surface mounted synchronous machine

Fig. 2.15: Studied machine for magnetic model validation

Table 2.2: Physical and geometrical parameters for the studied generators

	Machine A	Machine B
Axial length [mm]	1100	1100
Exterior stator radius [mm]	1224	1224
Stator yoke height [mm]	86	86
Slot height [mm]	104	104
Stator tooth aperture angle [°]	0.75	3.75
Stator slot aperture angle [°]	0.75	3.75
Exterior rotor radius [mm]	1028	1028
Magnet height [mm]	75.7	24
Rotor yoke height [mm]	–	51.7
Magnets aperture angle [°]	4.2	12
Air gap height [mm]	8	8
Number of phases-winding topology	5-distributed-single layer	3-distributed-Double layer
Poles - Slots	24 - 240	24 - 180
Current density[A.mm^{-2}]	3.5	2.2

[2]No-load flux are computed for one turn per coil, supposing that all the winding are in series.

2.6.2 Machine A results

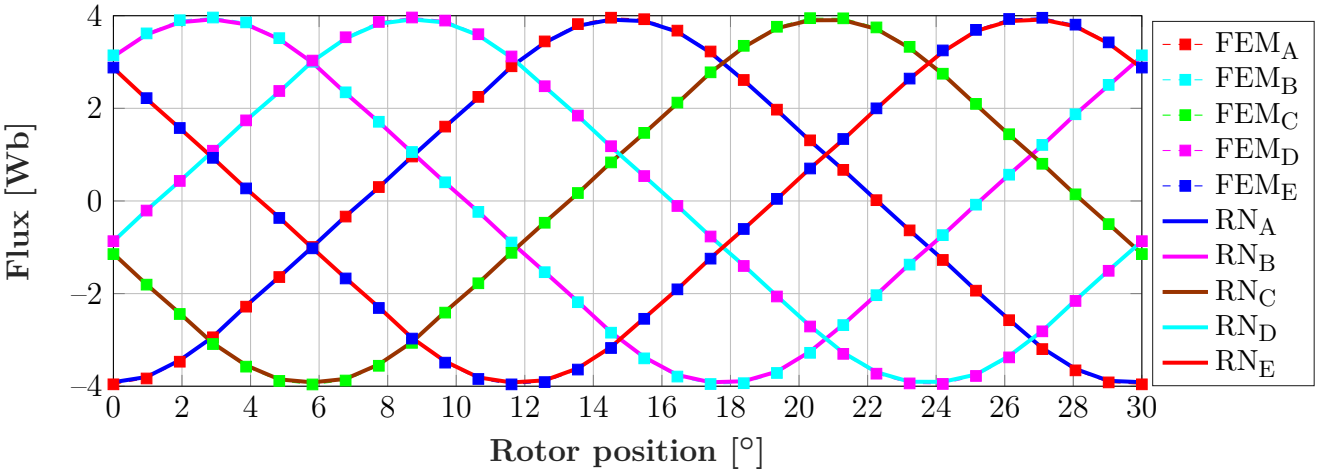

Fig. 2.16: Flux through the phases at no-load

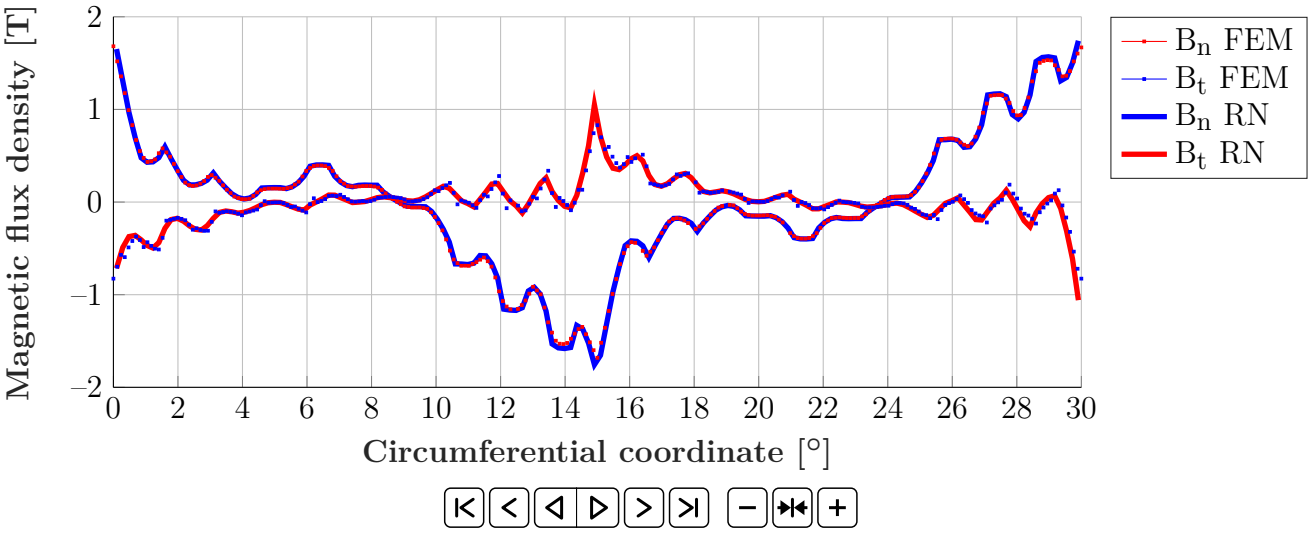

Fig. 2.17: Magnetic flux densities comparison

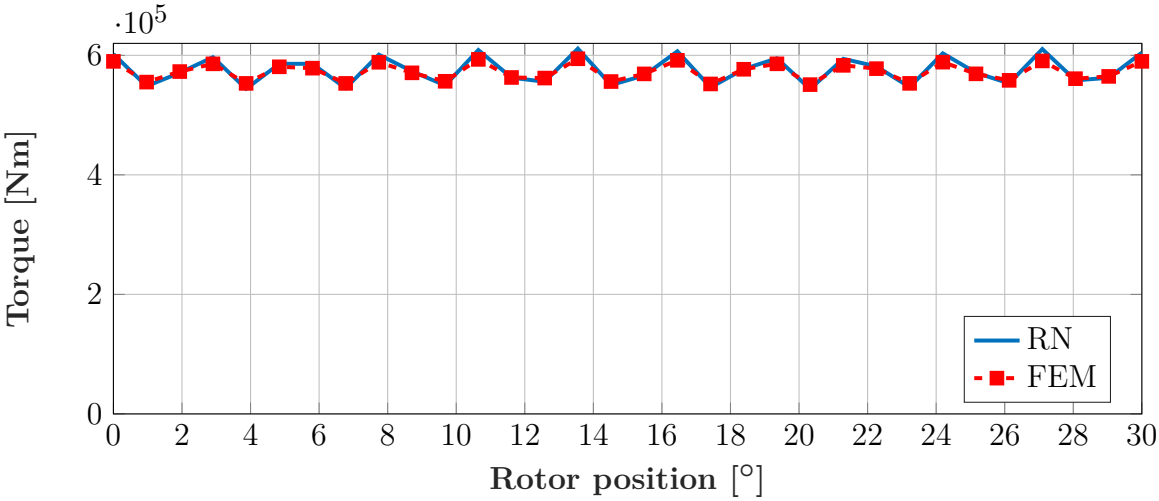

Fig. 2.18: Electromagnetic torque

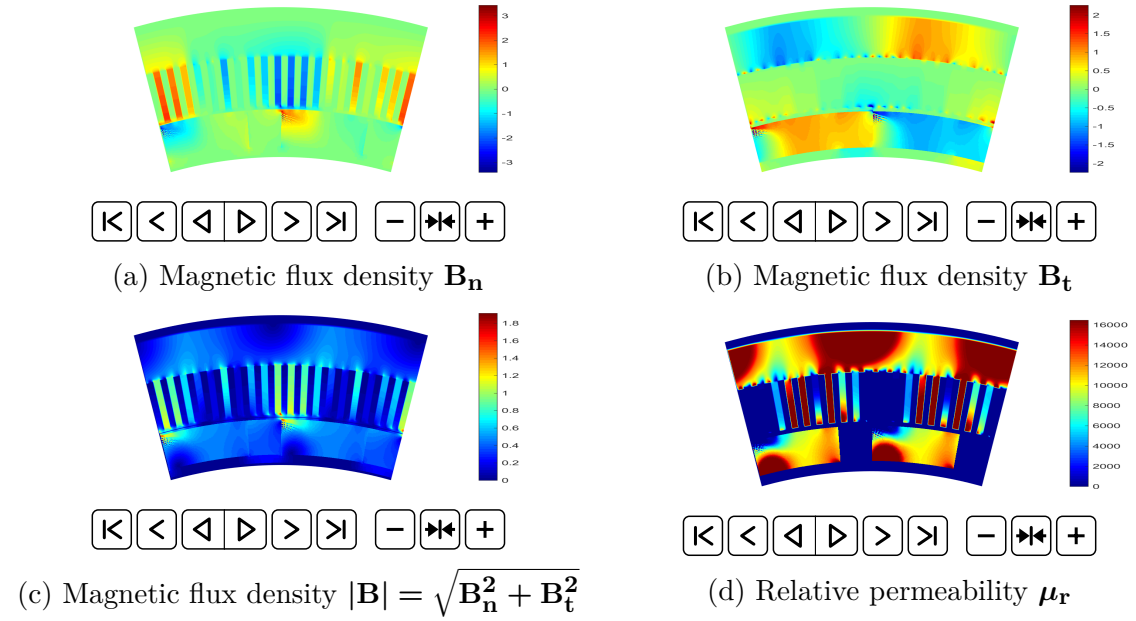

(a) Magnetic flux density $\mathbf{B_n}$

(b) Magnetic flux density $\mathbf{B_t}$

(c) Magnetic flux density $|\mathbf{B}| = \sqrt{\mathbf{B_n^2} + \mathbf{B_t^2}}$

(d) Relative permeability $\boldsymbol{\mu_r}$

Fig. 2.19: Results obtained by reluctance network

As can be seen from figures 2.16, 2.17, 2.18, a good agreement is shown between results obtained from the developed model and those derived from the commercial software. It can be noticed also that all the studied positions local quantities are accurate, which is achieved thanks to interpolation in the airgap

2.6.3 Machine B results

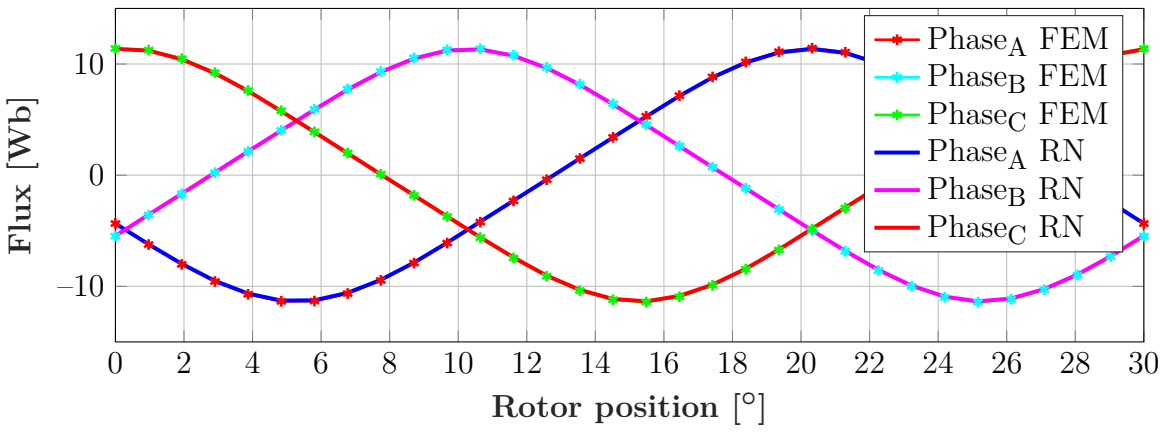

Fig. 2.20: Magnetic flux densities comparison

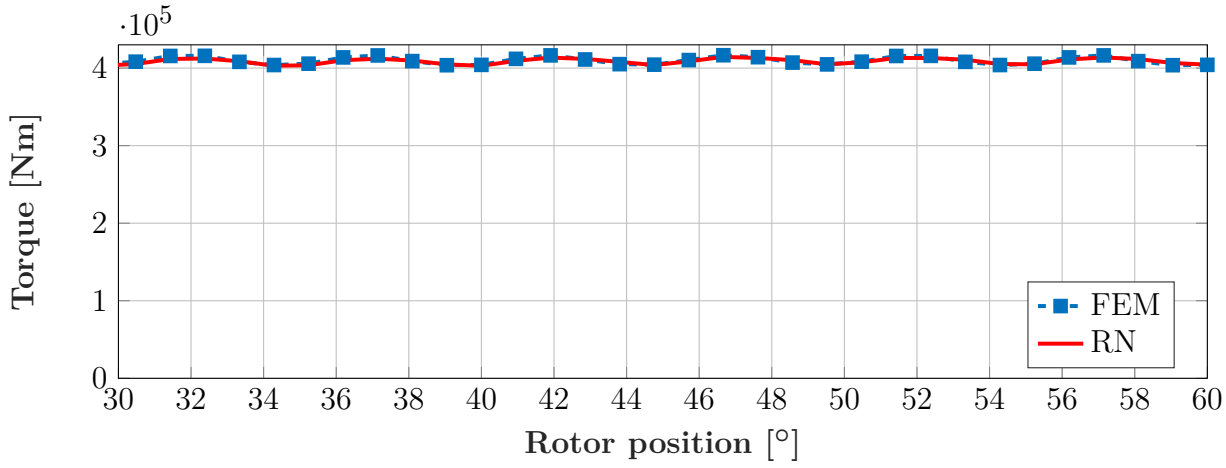

Fig. 2.21: Electromagnetic torque

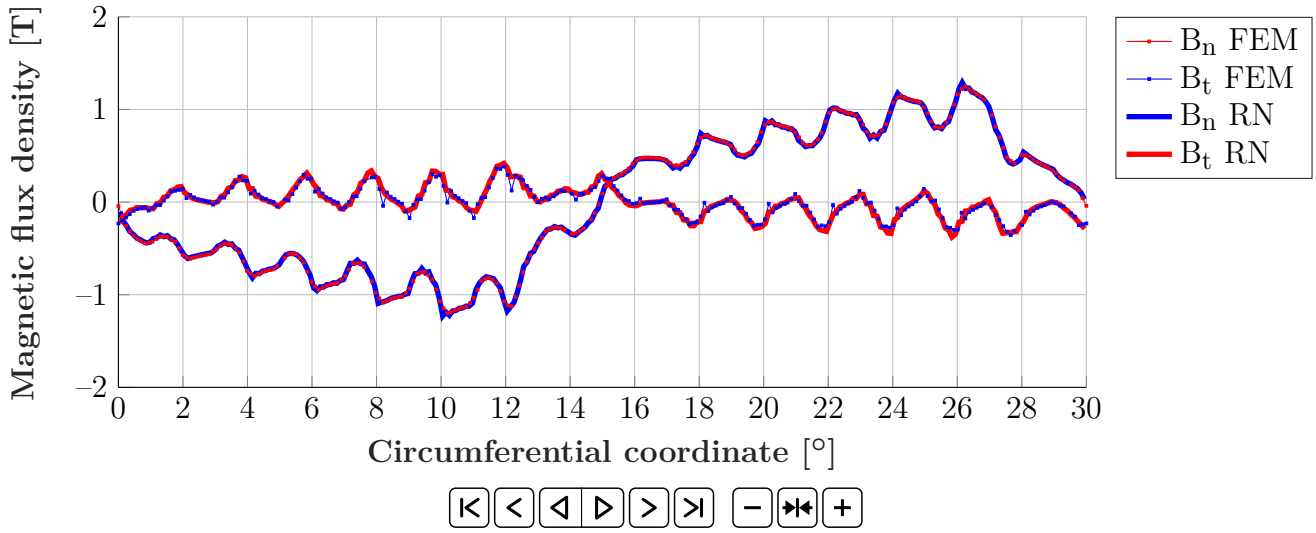

Fig. 2.22: Magnetic flux densities comparison

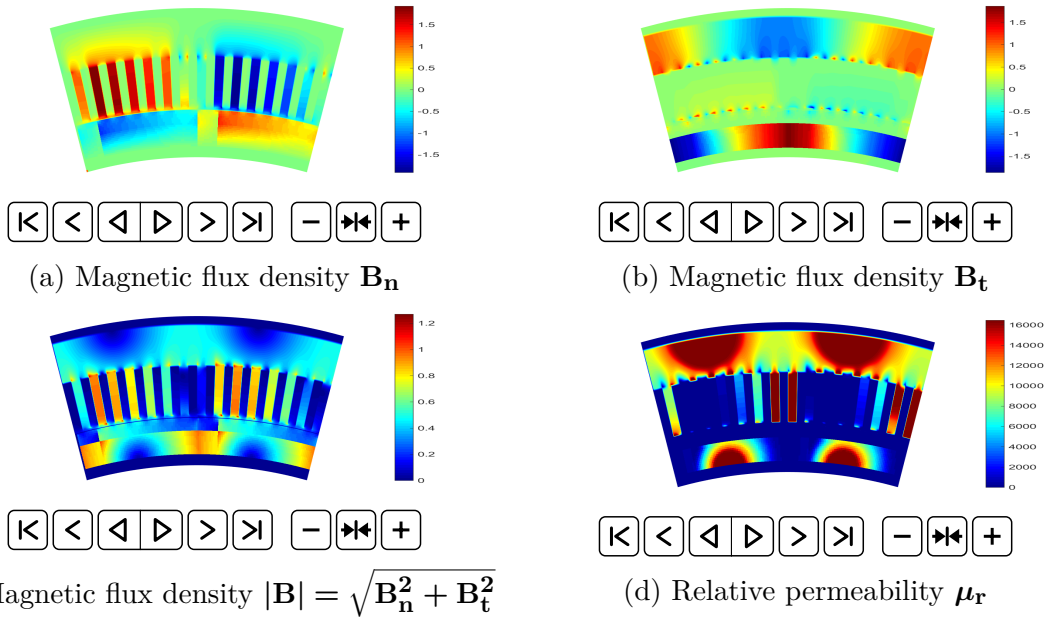

(a) Magnetic flux density $\mathbf{B_n}$

(b) Magnetic flux density $\mathbf{B_t}$

(c) Magnetic flux density $|\mathbf{B}| = \sqrt{\mathbf{B_n^2} + \mathbf{B_t^2}}$

(d) Relative permeability $\boldsymbol{\mu_r}$

Fig. 2.23: Results obtained by reluctance network

As can be seen from figures 2.20, 2.21 and 2.22, a good agreement is shown between results obtained from the developed model and those derived from the commercial software. Since current density supplying machine **A** is greater than the one delivered to machine **B**, it is clear that magnetic flux densities are greater in machine **A**, which explains greater torque and higher saturation levels as can be seen in figures 2.19 and 2.23.

2.6.4 Thermal model validation

In order to validate the transient thermal model, comparison between the obtained results with the model and measurement will be done on a double star surface mounted synchronous machine. First, only Joule losses will be taken into consideration, which means that the machine will be stationary and fed by a direct current supply for each of the six phases ensuring a uniform losses distribution, which is achieved via the wiring explained through the figure 2.24. Second, the machine's thermal state will have two stages, the first one is heating phase, while the second is natural cooling one by simply switching off the DC supply. Finally, the temperature evolution of the hottest spot in the slot obtained from the model will be compared to the measured one, which means that the temperature sensor is assumed to be located exactly in the same theoretical hot spot determined from simulation, table 2.3 contains the main parameters used to simulate the thermal behavior of the machine[3].

Table 2.3: Thermal simulation conditions

Ambient temperature	23 [C°]
Joule losses	70 [W]
Iron thermal conductivity	50 [$W.K^{-1}.m^{-1}$]
Crankcase thermal conductivity	150 [$W.K^{-1}.m^{-1}$]
Magnets thermal conductivity	13 [$W.K^{-1}.m^{-1}$]
Convection coefficient between external air and crankcase	20 [$W.K^{-1}.m^{-2}$]
Filling factor	0.45
Iron thermal capacity	440 [$J.K^{-1}.Kg^{-1}$]
Magnet thermal capacity	360 [$J.K^{-1}.Kg^{-1}$]
Copper thermal capacity	380 [$J.K^{-1}.Kg^{-1}$]
Crankcase thermal capacity	897 [$J.K^{-1}.Kg^{-1}$]
Air thermal capacity	1003 [$J.K^{-1}.Kg^{-1}$]

[3]Some geometrical parameters are not communicated for confidential reasons.

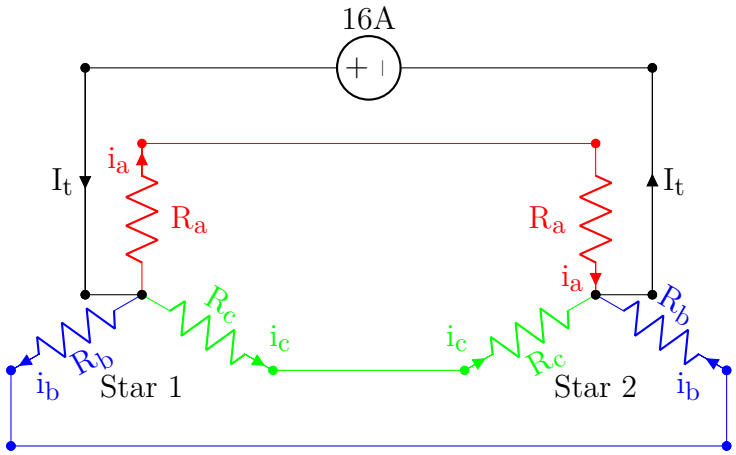

Fig. 2.24: Supply circuit

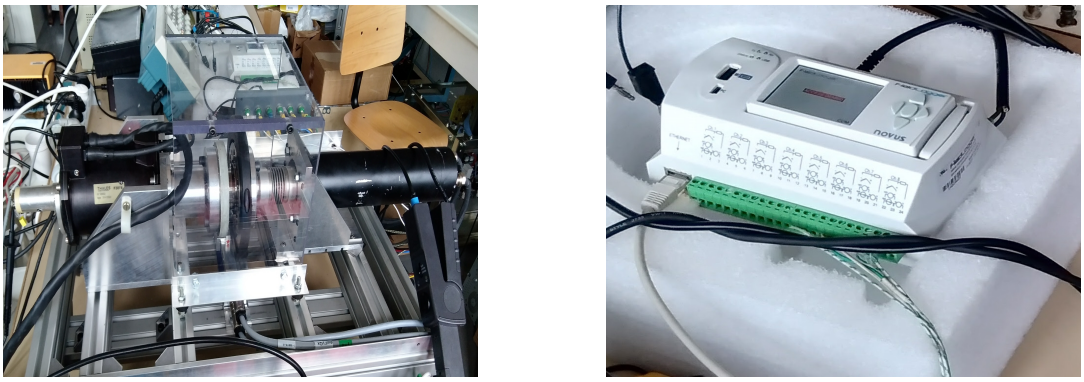

(a) Studied machine (on the right)

(b) Thermal acquisition module

Fig. 2.25: Material used fo measurment

Fig. 2.25 shows the material for the measurment, while Fig. 2.26 compares simulation results with measurements one for both heating and natural cooling one, a good agreement is observed with which one can confirm the formulation used in (2.30) and strengthen all the assumption made among this chapter for the thermal part.

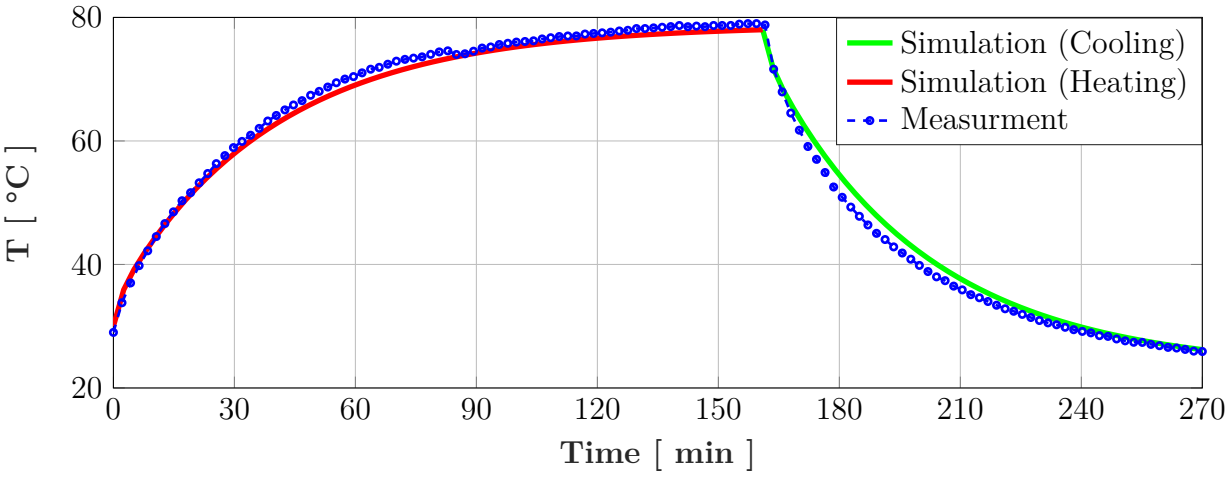

Fig. 2.26: Temperature evolution through the time

Conclusion

This chapter explained the magneto-thermal modeling of electrical machines. the choice of methodology was oriented to lumped parameter since it offers the best compromises between computation time and accuracy which is most suitable in the pre-design stage, in which an evaluation of a large domain is needed.

The selection of interpolation method at the sliding surface eliminates most of the numerical problem met with classical solution such as analytical one or variable reluctance network method, offering an interdependency between two reluctance networks, or more which will be discussed with magnetic gears example in the next chapter.

Results showed a respectable accuracy by comparing the obtained results with those derived from finite elements method for the magnetic model and with measurement. It is clear, even before writing the model or implementing it via a programing language, that lumped thermal model will be theoretically more accurate than reluctance network; since in thermal model the comparison is done using directly the potential. However in reluctance network case, results are derived from magnetic scalar potential which explains the error amplification and thus a lower accuracy compared to lumped thermal models.

Even though reluctance network offers good accuracy in a global way for the non-linear resolution, local one is not achieved in some conditions which may be caused by machine's structures it self and/or to slot's current density and/or convergence criteria which was set to global in our model; which can be seen in figure 2.23. In an other way and honestly speaking, reluctance network may not be suitable for iron losses computation in extreme saturation levels since local divergence can cause higher errors in magnetic field computation. This last remark is valid for the case of fixed point method using global convergence criteria, results may change and more numerical stability and accuracy can be achieved using Newton-Raphson method. As could be seen through this chapter, an equivalence can be found between reluctance network and lumped parameter model which is resumed in the table under[3].

	Magnetic circuit	**Thermal circuit**
State variable	U [A]	T [K]
R	$\mathrm{R} = \int_{\mathrm{s}} \frac{\partial \mathrm{l}}{\mu_0 \mu_\mathrm{r}(\mathrm{H}) \partial \mathrm{s}}$ [H^{-1}]	$\mathrm{R} = \int_{\mathrm{s}} \frac{\partial \mathrm{l}}{\mathrm{k} \partial \mathrm{s}}$ [$\mathrm{W}^{-1}.\mathrm{K}$]
Flux equation	$\phi_{\mathrm{mag}} = \mu_0 \mu_\mathrm{r} \int_{\mathrm{s}} \overrightarrow{\mathrm{grad}}(\mathrm{U})$	$\phi_{\mathrm{th}} = \lambda \int_{\mathrm{s}} \overrightarrow{\mathrm{grad}}(\mathrm{T})$
Basic equation	$\Delta \mathrm{U} = \mathrm{R} \phi_{\mathrm{mag}}$	$\Delta \mathrm{T} = \mathrm{R} \phi_{\mathrm{th}}$

Chapter 3

Optimal design of the studied structures

Introduction

This chapter will introduce and explain the optimal design procedure used for the design of electrical machine, the general approach will be detailed and problem formulation will be given. In addition, a brief introduction to several optimization algorithms will be given, in order to identify the appropriate algorithm to use depending on design stage and on the model used to compute objectives and/or constraints. To do so, the first section will introduce the general formulation of an optimization problem followed by a second one, in which some benchmark functions are presented, in order to explain the difficulties met during minimization process. After that and in the third section, types of optimization algorithms will be explained briefly, which will help the choice later for the considered study. Fourth and fifth section clarify the multi-objective constrained optimization with the different methods used to achieve the minimization with single or multiple runs. This will be followed by a non-exhaustive list of previous works in the optimization of electrical machines field in order to see the used algorithms and models used for optimal design. Finally, optimization results for two topologies, a surface mounted synchronous generator and a concentrated flux permanent magnet machine, under different constraints will be discussed analyzed and validated by comparing the obtained characteristics with FEM software ones.

3.1 General mathematical definitions

In order to explain the optimal design of electrical machine and avoid common mistakes, some definitions must be made. In general, a multi-objectives constrained and bounded optimization problem is defined in 3.1.

$$\begin{cases} \min \mathrm{F_i}(\mathrm{x}) \\ \mathrm{G_i}(\mathrm{x}) \leq 0 \\ \mathrm{H_i}(\mathrm{x}) = 0 \\ \mathrm{x_{LB}} \leq \mathrm{x} \leq \mathrm{x_{UB}} \end{cases} \tag{3.1}$$

Where:

1. $\mathbf{F_i(x)}$ are the objective functions to minimize, which can have multiple inputs and outputs.

2. $\mathbf{G_i(x)}$ are the inequality constraint functions, which can be linear or not.

3. $\mathbf{H_i(x)}$ are the equality constraint functions, which can be linear or not.

4. $\mathbf{x_{LB}}$ & $\mathbf{x_{UB}}$ are respectively the lower and upper bounds, which define the limits of the research domain.

Before going further on the types of optimization algorithms existing around the scientific world, one must differentiate between local and global minima, in a brief simplistic way possible :

Local minima = minimize the objectives in a defined sub-interval of the research domain.

global minima = minimize the function on the overall research domain; minimize all the local minima.

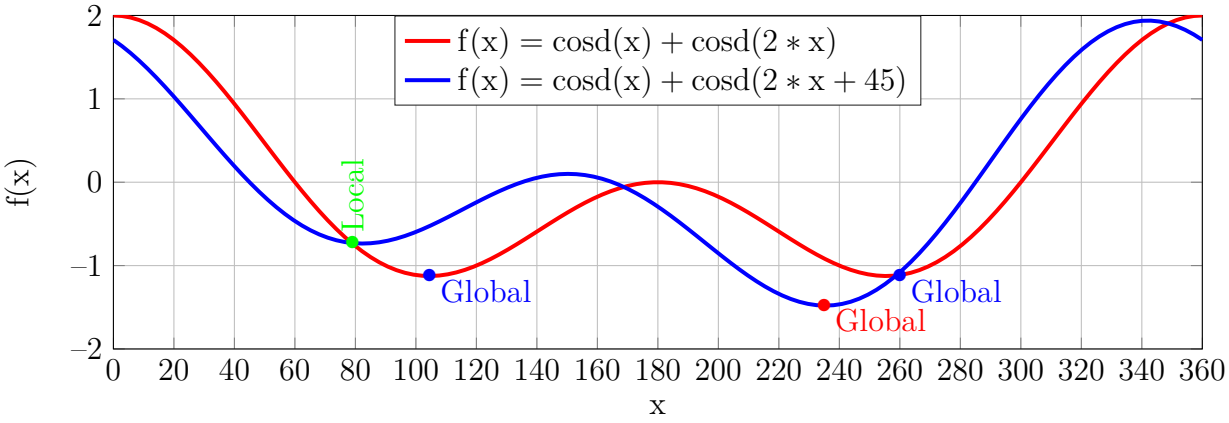

Fig. 3.1: Example of local and global minima

As can be seen in Fig. 3.1, both functions represent difficulties, the first one with two global minima, which means that a global research algorithm will be needed to find both of them in the same time, otherwise multiple runs must be done at different initial conditions, hoping that both minima will be found. The second one contains a local minima which again can be tricked by some algorithm, thus a global research algorithm must be used in order to increase the chances of finding it.
The last definition is important, since it impacts directly algorithm's choice ; in an other word some methods get triggered by local minima and others may avoid them and find global ones. For those reasons, the next section proposes test functions used to measure the robustness of an optimization algorithm. The second one explains the different families of optimization algorithms, their positives and negatives aspects in terms of initial information requirements and computation time.

3.2 Benchmark functions for optimization algorithm

The first goal of test function is to test the ability of an optimization algorithm of finding global minimum, the goal here is not to expose them entirely but to see what can an optimization algorithm meet during its research. These function have one or many characteristics such as [97, 98] :

Modality Represents the number of peaks or in an other term local minima which can trap the optimization process and modify the search pattern.

Basins Represented by a domain surrounded by large areas of steep incline, this will attract easily optimization algorithm and once more trick them.

Valleys Represented by an area with little change of objective function and surrounded by regions of steep descent. This last region will attract the algorithm rapidly, however, once the floor of the valley reached the processes can be slowed down dramatically.

Dimensionality This increases the difficulty, since increasing the dimension of the system will systematically enlarge the research domain and thus the difficulty of finding the minima, since it can increase valleys, basins and modality.

In order to explain more the difficulty of optimal research and the encountered problems, listed above, with optimization algorithms, an example of some test function are given below :

Bukin function Characterized by many local minima located at the same ridge as can be seen in Fig. 3.2a, its global minimum is located at $x = (-10, 1)$ given by (3.2). This function represents the modality problem.

$$f(x) = 100\sqrt{\left|x_2 - 0.01 * x_1^2\right|} + 0.01|x_1 + 10| \tag{3.2}$$

Booth function Characterized a plated shape which can trick gradient algorithm as can be seen in Fig. 3.2b, its global minimum is located at $x = (1, 3)$ given by (3.3). With this function the valley problem.

$$f(x) = (x_1 + 2x_2 - 7)^2 + (2x_1 + x_2 - 5)^2 \tag{3.3}$$

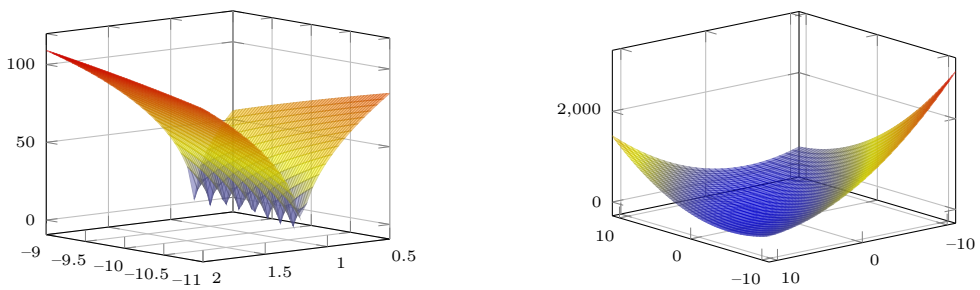

(a) Bukin function (b) booth function

Fig. 3.2: Example of optimization test function

3.3 Type of optimization algorithms

Optimization algorithm can be separated into two large families: ones with deterministic behavior and the rest with stochastic, probabilistic function, this will be explained in the next subsection with examples of famous used algorithms among both families.

3.3.1 Deterministic optimization algorithm

Generally called as local optimization algorithms, their specificity accord that they are deterministic, since if the process of optimization is repeated using the same deterministic algorithm and condition, it will converge to the same minimum via the same path. Which means that no random behavior is characterized. In addition, a starting point is needed to execute these type of algorithms and an information about the derivative may be needed; which will lead to the following classification:

Order 0 algorithm Only an information about the function is needed such as ; Powell algorithm [99] and Rosenbrock method [100].

Order 1 algorithm An information about the function and its first derivative (gradient) are needed such as ; conjugated gradient [101].

Order 2 algorithm An information about the function, its first derivative (gradient) and second (Hessian) are needed, which is an improved version of the order 1 algorithms where the Hessian serves as a mean to have a dynamic step in the optimization processes.

These algorithm fails to find global minima, especially functions representing the previous listed difficulties and knowing that optimization in electrical machines field are done in complex non linear functions and under constraints with more than one objective, which obligates the designer the use of stochastic algorithms such as genetic algorithm or particle swarm.

3.3.2 Stochastic algorithms

Stochastic optimization methods rely on probabilistic and random mechanisms. This characteristic indicates that several successive executions of these methods can lead to different results for the same initial configuration problem of optimization, which gives a great ability to find the overall optimum of the problem. Unlike most deterministic methods, they don't require an initial point, nor the objective function gradient in order to reach the optimal solution. However, a large number of evaluations is needed before converging to the optimal solution. Next two famous algorithms will be presented, in order to explain these algorithms pattern.

3.3.2.1 Particle swarm PSO

Proposed in [102], the algorithm tries to reproduce cooperative animal's behavior such as ; insects, herds birds and fishes [103]. This behavior of a swarm is characterized by a search path, which depends on its and others members experiences. To describe the functioning of this algorithm ; each individual of the population have a velocity and position, which will be updated iteratively with respect to the best solution found by the particle best solution

and population one. The first principles of this method were basics and encountered first improvements such as additional parameters to correct the particle velocity such as inertia weight [104] or constriction factor [105]. Further development added more stability to PSO such as multi-sub-population, selection strategy improvement, velocity update and combination with other search techniques[103].

3.3.2.2 Genetic algorithms GA

Genetic algorithm copy populations evolution according to the principles of natural selection and "survival "of the fittest" as stated by Darwin [106], in which and from an initial "population" constituted from a set of "individuals", the algorithm "evolves" at each iteration called "generation" in order to "select" the best individuals and thus the optimal solution. In order to evolve, GAs stimulate biological processes such as ; mutation, crossover and reproduction[107], which is described in Fig. 3.3, for more deep explanation readers are guided to [108, 109, 110, 111].

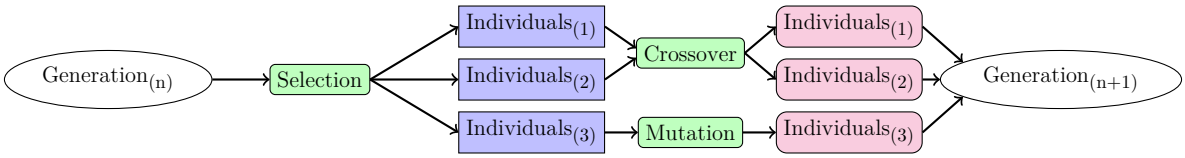

Fig. 3.3: General scheme of genetic algorithms

It can be noticed that the important parameters affecting the nature og a GAs are the operators, which will be explained next.

Selection operator This operator is the most important one, since it allows the selection of parents and create the next generation. In a general matter, individual can be selected using different techniques depending on the survival probability, ranking and fitness function [112] :

1. Each individual have a survival probability, which is proportional to its fitness value; ending up by a method of selection called proportionate reproduction
2. Each individual will be selected depending on its ranking, which is its position in the population sorted from best to worst.
3. The individual will be selected from a tournament, in which other randomly chosen individual participate and the one with the best fitness function wins.

Crossover operator The crossover operation generates two children from two different parents, in fact this operation allows the information exchange between individuals, as illustrated below, many possibilities can occur to generate a crossover operator such as :

1. A binary random vector having the same length as the individual will be generated containing only 1 and 0, position with 1 value will be affected from parent one, otherwise it will be generated from parent two, the operation is inversed

for the second child, as can be seen below :

$$\begin{cases} \text{Parent}_1 = [\alpha\beta\gamma\lambda] \\ \text{Parent}_2 = [1234] \\ \text{Vec} = [0101] \end{cases} \Rightarrow \begin{cases} \text{Child}_1 = [1\beta3\lambda] \\ \text{Child}_2 = [\alpha2\gamma4] \end{cases} \tag{3.4}$$

2. A random integer number will be generated between 0 and **n** the length of the vector characterizing the individual, the lowest value will be taken from one parent and the highest from the other, the same processes can be applied on two generated random number.

$$\begin{cases} \text{Parent}_1 = [\alpha\beta\gamma\lambda] \\ \text{Parent}_2 = [1234] \\ \mathbf{n} = 3 \end{cases} \Rightarrow \begin{cases} \text{Child}_1 = [\alpha\beta\gamma4] \\ \text{Child}_2 = [123\lambda] \end{cases} \tag{3.5}$$

3. A random number will be generated and a child will be created as follow:

$$\begin{cases} \text{Parent}_1 = [\alpha\beta\gamma\lambda] \\ \text{Parent}_2 = [1234] \\ \text{r}_\text{i} = \text{random} \end{cases} \Rightarrow \left\{ \text{Child}_\text{i} = \text{Parent}_1 + \text{r}_\text{i} * (\text{Parent}_1 - \text{Parent}_2) \right. \tag{3.6}$$

It is clear that the crossover is a powerful operator which will allow the exchange of information among population, however this information will be inside it, which means that the algorithm can be misled by local minima, for these reasons a mutation operator is added and explained next.

Mutation operator the role of this operator is to change randomly a part of the individual gene, which can be global or local. The next illustration below explains the difference between global and local mutation; lets imagine that an individual characterized by a vector of 8 variable:

1. In the first case, a random vector will be selected, affecting a mutation probability to each of its components ; If the number is superior than a given value, selected by the designer or user, then the value of the correspondent components will be replaced by a random number picked from an interval confined between its bounds. Otherwise the components will stay the same.
2. A random vector from Gaussian distribution will be added to the current one, the standard deviation and mean value can be tuned depending on the user or developer.
3. The third cases explains a function existing in Matlab and may be useful in constrained bounded optimization problems, where the mutation will be chosen according a certain direction and length. The direction and length are determined by the information feasibility from previous generations; with this, the respect of boundaries and constraints will be achieved easily than the two previous ones.

3.4 Multi-objectives constrained optimization

As stated previously the reproduction and the behavior of an evolutionary algorithm depends highly on the fitness function, which is related directly or indirectly to the objective function in the case of mono-objective optimization. However, in the case of multi-objectives optimization when a trade-off must be made, as an example and in the domain of electrical machine design the reduction of magnets weight and the maximization of efficiency might be difficult since these two objectives are antagonist. This will impose a problem on which solution is better than the other, and generally ends up by what's called Pareto optimality leaving the final decision to the user by choosing between compromised solution were the improvement of one objective lead to the deterioration of others when the dominant solution are achieved. In a mathematical way, a solution x_1 is said dominant on x_2 when (3.7) is satisfied. This means that x_1 improves at least one objective without deteriorating the other.

$$\begin{cases} f_i(x_1) \leq f_i(x_2) & \forall i \in [1, 2, 3, ...K] \\ f_i(x_1) < f_i(x_2) & \exists i \in [1, 2, 3, ...K] \end{cases} \tag{3.7}$$

The handling of multi-objectives criteria can be achieved through one of the two commonly known methods[113]:

3.4.1 Transformation of the problem into mono-objective

This is the first proposed solution, where the multiple objectives are transformed to a single one through one of the following methods:

Weighted aggregation The mono-objective equivalent problem is obtained by multiplying each objective by its own coefficient, which can be dynamic or static, it is clear that coefficients choice, which is left to the user, impacts directly the optimization results and may deviate the minimization processes from the optimum solution set. The mathematical transformation is given in (3.8)

$$F_{mono} = \sum w_i F_{i_{multi}} \tag{3.8}$$

Goal programming This method associates a goal to each objective function and a weight, the idea is to hopefully force the mono-objective algorithm to the optimal solution, while respecting goals for each objective function. The weight associated to each objective function represent there importance order. In a mathematical way, the problem is illustrated in (3.9)

$$F_{mono} = \sum w_i \left| F_{i_{multi}} - Goal_i \right| \tag{3.9}$$

ϵ-constraint the method consists of optimizing using one objective function while treating the rest as bounded constraints repetitively until the Pareto front is found. The mathematical formulation is illustrated in 3.10

$$\begin{cases} \min(F_k) \\ F_i < \epsilon_i \quad i \neq k \end{cases} \tag{3.10}$$

3.4.2 Pareto-based approaches

The main advantage of these approaches is there ability to generate optimal Pareto solutions in the concave portions of the Pareto border, in order to achieve it two criteria are needed :

1. Converging to the Pareto border: most research focused on the selection stage. In which, ranking methods are applied in order to establish an order (called rank) between individuals. This last one depends on the notion of dominance and therefore directly from the Pareto optimality.

2. Find diversified solutions in the Pareto border: the methods of diversity maintenance use technique of niches or the crowding, which will be important for stabilizing subpopulations along the Pareto border.

The famous algorithm using this technique are ; NSGA2 [114] with its first version NSGA1 [115], SPEA2 [116] and its first algorithm SPEA [117]. The goal as said previously is to determine the ranks of population a certain generation in order to make an appropriate selection and apply the listed previously operators to generate the next population and converge to the Pareto frontier, the same Pareto approach is also made in particle swarm optimization in [118, 119]; for more detailed information about the selection, mutation and crossover process, readers are guided to the listed references.

3.5 Solving the constrained problem

The constraints introduced into an optimization problem can be constituted from equality, inequality function or both of them as in (3.1), taking them into consideration is necessery in order to have optimal solution satisfying all the listed conditions. Two methods will be discussed here :

Augmented Lagrangian The method consist of transforming the constrained problem into series of unconstrained problems, where the Lagrangian function ($\mathcal{L}$) is introduced and minimized in order to satisfy the constraints [120]. The mathematical formulation of the problem is givzn by (3.11), where λ_i and r are respectively Lagrange multipliers and penalty coefficient.

$$\mathcal{L}(x, \lambda, r) = F(x) + \sum \lambda_i g_i(x) + r \sum g_i^2(x) \tag{3.11}$$

Penality method The method consists of adding a penalty term to the objective function, its can be static or dynamic [121]. In the dynamic case the penalty depends on the feasibility space, in a simplistic way (3.12) explains the constrained problem transformation, where δ_i are the penalty coefficient .

$$F_{new}(x) = F(x) + \sum \delta_i g_i \begin{cases} \delta_i = 1 & \text{if constrainst is violated} \\ \delta_i = 0 & \text{if constrainst is satisfaied} \end{cases} \tag{3.12}$$

3.6 Previous work on electrical machine optimization

This section presents a list of previous work related to the optimization of electrical machines with different objective and parameters using analytical or/and numerical tools to model the multi-physics behavior of the electromagnetic actuators.

Doubly-fed induction machine Optimization [122] Optimizes a doubly-fed induction machine of 3.2 [MW] power and operation at a rated speed of 360 [rpm]. In order to achieve his goal, the author used a coupled model between Matlab and Comsol, where the FEA model was based on an approximation of the transient-behavior through the magneto-static resolution [123]. NSGA2 was used in order to determine the Pareto front constituting the trade between actives material costs and efficiency using nine geometric variables (stator and rotor) under three constraints, which are stator and rotor tooth heights ratios respectively to their width and axial length maximal value. Results showed that the Pareto front is delimited between (94%,60[keuros]) and (96%,160[keuros]) for a stator current density of 4[A.mm^{-2}], while when this last value is set to 3[A.mm^{-2}] the front is delimited by (94%,70[keuros]) and (95%,120[keuros]). However for two selected machine from the front, torque ripples were equal to 14% and 15% respectively, which is relatively considerable in this power range.

Direct-coupled ironless axial flux optimization [124] Proposes an optimization of direct-drive 30 [kW] ironless axial flux permanent magnet synchronous wind generator. The main goal was to have low cost and high annual energy yield, to do so, Rayleight distribution was used in order to model the wind characteristics while the generator performances were computed through a reduced magnetic equivalent circuit, in which the saturation was taken into consideration. The optimization were conducted using PSO constrained algorithm with five parameters: 1)inner to outer diameter ratio, 2)magnet width to pole pitch ratio, 4)flux density of the air gap, 5)electrical loading. Torque, ratio of outer diameter to axial length and deflection of the rotor disc in the outer radius represented the constraints. The optimization processes was done for multiple poles/slots combination and resulting by 12poles/18slots as the best one for maximum profit were the cost of active materials was around 49 [keuros] with: an outer generator diameter equal to 1030[mm], axial length of 30 [mm] and an efficiency of 91.5% at the rated speed of 200 [rpm].

Multi-physics modeling and optimization of a multi-v-shape IPM [125] proposes a coupled multi-physics model for a multi-V-shape 11 [kW] Interior Permanent Magnet (IPM) motor with concentrated winding. Multi-objectives famous genetic algorithm NSGA2 was used in order to achieves the requirement, which are the maximization of efficiency and reduction of cost. The optimization processes was subject to five constrains which are : 1)electromagnetic torque, 2)power factor, 3)stator current, 4)voltage, 5)demagnetization field. In order to achieve the objectives and satisfy the listed constraints, authors used semi-analytical models for magnetic and thermal modeling; where the most impacting physical phenomena were taking into consideration such as steel sheet non-linearity, slot's equivalent thermal conductivity, iron losses and end windings leakage inductance, while the electrical model serves to compute the voltage at the motor terminals. The optimization was curried out with ten parameters:1)airgap radius, 2)tooth angle, 3)stack length, 4)tooth height, 5)number of turns, 6)barrier tilt angle, 7)barrier opening angle ratio, 8)barrier width, 9)current angle, 10)current density. The study resulted by a Pareto front delimited by (94.2%,1pu) and (92.8%,0.8pu) for efficiency and cost respectively, results were compared with finite elements ones and showed a good agreement with the proposed model.

Gear Ratio Optimization of a Full Magnetic Indirect Drive Chain [126] deals with the optimization of a full magnetic indirect drive with magnetic gears. Multi-objectives particle swarm (MOPSO) algorithm was used to solve this problem, where the constraints are constituted from torques in high-speed and low-speed shafts of the magnetic gear. The optimization is composed of seven parameters: 1,2)yoke thicknesses, 3,4)permanent magnet thicknesses, 5)ferromagnetic pole thickness, 6,7)pole pair number of the permanent magnet rings. The magnetic gear is modeled analytically by formal solution of Maxwell's equations and under strong assumption ($\mu_{\text{iron}} = \infty$), after that, the objectives, which are gear ratio and magnetic gear weight, are computed for a given set of parameters and for a 5 [MW] power. The last step allowed the fitting of the obtained Pareto front by a third degree polynomial, allowing the determination of several Pareto fronts through an analytical estimation of generator weight through its external radius. Authors found that direct drive structures are characterized by the heaviest weight, where the optimal solution represents 65 [ton], followed by single stage indirect drive where the generator weight 21.5 [ton] and magnetic gear one 26.2 [ton], ending by a total mass of 47.7 [ton]. Finally and according to authors, two stage indirect drive represents the minimal weight compared to the two previous ones where, first stage magnetic gear weights 17.7 [ton], while the second gear weights 5.7 [ton] and a generator mass equal to 6.1[ton]. The global gear ratio for one stage indirect drive was equal to 8.7, while for the two stage one the global ratio was near 46. However, authors suggested a mechanical analytical model, in order to estimated the full global structure weight and thus correct the obtained Pareto front.

High-speed interior PM Machine multiobjective optimization [127] proposes multiphysic optimal modeling of an interior permanent-magnet synchronous machine (IPMSM) dedicated to high speed, including magnetic, electric, thermal and mechanical aspects. The optimization processes includes two objectives : efficiency and machine's weight, while thirteen variables are used to compute magnetic, thermal and mechanical stress of the selected topology are :1)stator outer diameter, 2,3)slot depth and width, 4)airgap length, 5)stator inner diameter, 6,7)magnet height and width, 8)hub radius, 9)stack length, 10)magnet remanence, 11)current density, 12)number of turns connected in series, 13)load angle. The constraints are constituted from: electromagnetic torque, demagnetization field, maximum field at load, phase voltage, copper temperature, static deformation and mechanical stress. It is clear her also that the multiphysics model needs to be as less complex as possible for magnetic, thermal and mechanical ones, therefore authors used analytical models based on d-q axis quantities computation for the magnetic part, lumped thermal parameters model for the thermal one and analytical expressions for the mechanical part. The used algorithm is a genetic one based on multi-objective optimization evolutionary approach, resulted by a Pareto front delimited by 96% and 97.4% efficiency for receptively 8.3 [kg] and 44.21 [kg], finally the model choice was justified by comparing its results with finite elements one for a chosen point front the Pareto front.

Optimization of cost including gearbox, generator and converter [128] investigates the cost-effective ranges of gearbox ratios and power ratings of multibrid permanent-magnet (PM) wind generator systems by using a design optimization method. Authors used analytical models for a single-stage mechanical gear, three phase surface

mounted permanent magnet generator and a back-to-back voltage converter. The optimization was processed through a genetic algorithm with the reduction total system cost as objective, while power and maximum flux density in the stator cores constitute the constraints. These constraints are computed through five variable : 1)air gap radius, 2)stator length, 3)poles number, 4)the peak air gap flux density, related to magnet's shape, 5)the peak stator yoke flux density, which from it the slots height and current density are determined. The optimization proceeded as follow: first for a given power and gear ratio, the total cost will be optimized using torque and gear ration in order to estimate the mechanical gear box cost, the optimization parameter in order to estimate the generator cost and finally its current to evaluate converter losses. It is clear here that the choice of an analytical model is necessary through linearization and simplification assumptions, otherwise the complexity of the model will increase exponentially requiring more variables and thus computation time. The optimization method then proceeds to for a specific range of gear ratio and choose the optimal one reducing the global cost. Results showed that for all studied power (0.75, 1.5, 3, 5 and 10) [MW] that cost is reduced between 13% to 33% by using geared generators, also for these solutions the optimal gear ration is between 4.5 and 9.7. The cost of 1[kW] varied from 108 to 209 euros for geared solution and from 141 euros to 242 euros for direct drive one, however, one msut be careful with these results since speed wind turbine speed decreases with the increase of the demanded power, which increases the needed torque and thus generator, gearbox and converter cost. This work strengthen the capability of GA optimization algorithms on finding optimal solution, since its results were compared with previous works such as in [129]

3.7 Results and discussion

In this part, an optimization study will be done in order to investigate the capability and behavior of two types of generators: a surface mounted one and a concentrated flux one, the main objectives are the reduction of permanent magnet masses and active parts one, since generator mass is a key factor in wind turbine generators. The studied structures must respect two major constraints; torque in order to achieve the requested power and temperature to stay under the maximal allowed one by the insulation class. In order to compute these constraints the developed model will be used, in which first the temperature distribution will be estimated through the geometric parameters and current density (only joule losses are taken into consideration) followed by a magnetic simulation in order to evaluate the maximum produced torque. Two major cases can be noticed using this pattern:

1. The machine does not respect the maximum allowed temperature in the slot and a penalty will directly assigned to it, which will bypass torque computation, in order to avoid unnecessary time computation.

2. The machine respects thermal constraints, thus magnet maximum temperature will be taken into account to correct remanent flux density and used after by magnetic model to compute the electromagnetic torque. In order to save more time, only static torque will be computed; which means that the electromagnetic field from the stator is static and rotor one is rotating through its movement. This means that

for each phasing between stator and rotor fields torque will be computed for only one position; allowing to reduce computation steps and finding maximum torque delivered by the generator. It is clear that this method is efficient only with generators having a relative reduced torque ripples, otherwise the estimated electromagnetic torque by the last described method will be either over or underestimated compared to the mean one. In a simple way, windings will be supplied by currents described in (3.13)

$$I_{phase} = I_{max} \times \cos(\frac{2 \times pi \times Phase_{number}}{n_{phase}}) \tag{3.13}$$

The used optimization algorithm is the embedded Matlab multi-objective algorithm, which is a copy of NSG2 [130]. The algorithm was tuned as follow for all the performed optimized: mutation rate was set to 0.01 and crossover one to 0.8, while the the optimization was performed for 200 generations with a population of 100 individuals. The non linear constraints were handled by penalty algorithm, in which: the penalty function is the fitness function if the individual is feasible, otherwise the penalty function is the maximum fitness function among feasible members of the population, plus a sum of the constraint violations of the infeasible individual multiplied by a factor of 100,which is the penalty factor.
For all the targeted power, the insulation is supposed to be class H, while the stator is assumed to be cooled through a fluid. Thermal coefficients are determined using the formulas given in the previous chapter, while materials proprieties used to compute active parts masses are give in Table. 3.1.The general scheme of optimization is illustrated in Fig. 3.4.

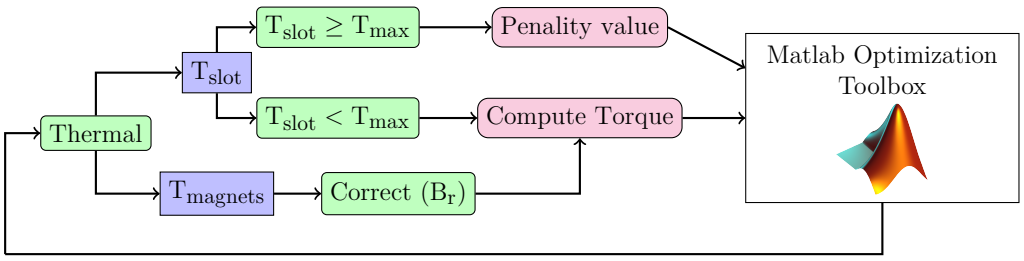

Fig. 3.4: General scheme of optimization process

The studied machines have respectively eight and nine parameters given below where:

concentrated flux permanent magnet machine (CFPM) Mostly called spoke type permanent magnet machine and having magnets with an ortho-radial magnetization as illustrated in Fig. 3.5 . Its main parameter used for optimization are :

1. Mean radius of air gap R_{mean}.
2. Active length among z axis L_{act}[m].
3. Slot's current density J_s.
4. Slot's angular opening θ_{slot}.
5. Slot's depth H_{slot}.
6. Stator yoke depth H_{yoke}.

7. Magnet opening θ_{mag}.
8. Magnet thickness H_{mag}.

Surface mounted permanent magnet machine (SMPM) Having magnets with an radial magnetization and mounted on the surface of the rotor yoke as illustrated in Fig. 3.15 . Its main parameter used for optimization are :

1. Mean radius of air gap R_{mean}.
2. Active length among z axis L_{act}[m].
3. Slot's current density J_s.
4. Slot's angular opening θ_{slot}.
5. Slot's depth H_{slot}.
6. Stator yoke depth H_{yoke}.
7. Magnet opening θ_{mag}.
8. Magnet thickness H_{mag}.
9. Rotor yoke thickness.

Tables 3.2, 3.5, 3.8,3.11, 3.14 and 3.17 summirize the optimization parameters, bounds, constraints and objectives for three different power ranges (5, 8 and 15 [MW]).

Table 3.1: Thermal proprieties used for the optimization

Cooling fluid temperature	30 [C°]
Iron conductivity	50 [$W.K^{-1}.m^{-1}$]
Aluminum conductivity	150 [$W.K^{-1}.m^{-1}$]
Magnets conductivity	9 [$W.K^{-1}.m^{-1}$]
Convection coefficient stator/cooling fluid	800 [$W.K^{-1}.m^{-2}$]
Filling factor	0.6
Iron density	7800 [$g.cm^{-3}$]
Magnet density	7600 [$g.cm^{-3}$]
Copper density	8500 [$g.cm^{-3}$]

3.7.1 Simulation and results for the concentrated flux machine

The optimization was curried out using the listed previously conditions, one can note that first the higher the torque , the higher required materials which is logic from Fig. 3.6, Fig. 3.9 and Fig. 3.12. Stator mass represents between 78% and 73% for the 15 [MW], 85% and 77% for the 8 [MW] and 84% and 77% for the 5 [MW] as can be seen in Table. 3.4, Table. 3.7 and Table. 3.10. Table. 3.3, Table. 3.6 and Table. 3.9 shows that using static torque computation did not affect the results that uch since torque ripple are not that high, which saved a considerable computation time during the optimization process, however 8 [MW] torque ripples are not acceptable for such application, which can be reduced using appropriate skewing or by modifying slot shape, one can note also that the increase of magnets will reduce the slot's depth, which impacts directly copper and stator

iron masses and reduces dramatically the required mass. It can be noticed also from Fig. 3.8, Fig. 3.11 and Fig. 3.14 that :

1. Air gap radius is stabilized around a mean value; 2.1, 1.1 and 1 [m] for respectively 15, 8 and 5 [MW] results, while the same can be noticed on active length. This is the consequence of optimization results, since the two major factor impacting global machine's weight are active length and radius, also this is related to torque's constraints, which is related directly to the square of air gap radius and active length, assuming a quasi-constant tangential pressure for Pareto front members.

2. Current density is bounded between 2.8 and 3.5 [A.mm–2], which seems logical for class H insulation, however it can be noticed that magnet parameters and slot's height are antagonist, since increasing magnet volume will allow the decrease of slot's height and thus copper and iron weight which results with a lighter machine compared to an other machine having less magnet volume.

3. Yoke thickness has the same variation with slot's height, this can be explained by the increase of magneto-motive force in the stator, thus a thicker yoke is needed in order to reduce saturation rate, this information couldn't be obtained without taking into consideration iron non-linearity, which justify the use of such model, since in linear model any yoke thickness will be sufficient.

4. A minimum of 1000, 135, 220 [Kg] of magnets is required in order to achieve the needed torques resulting density of 555, 500, 547 [Kg of magnet/MNm] respectively with class H insulation and using the considered cooling method.

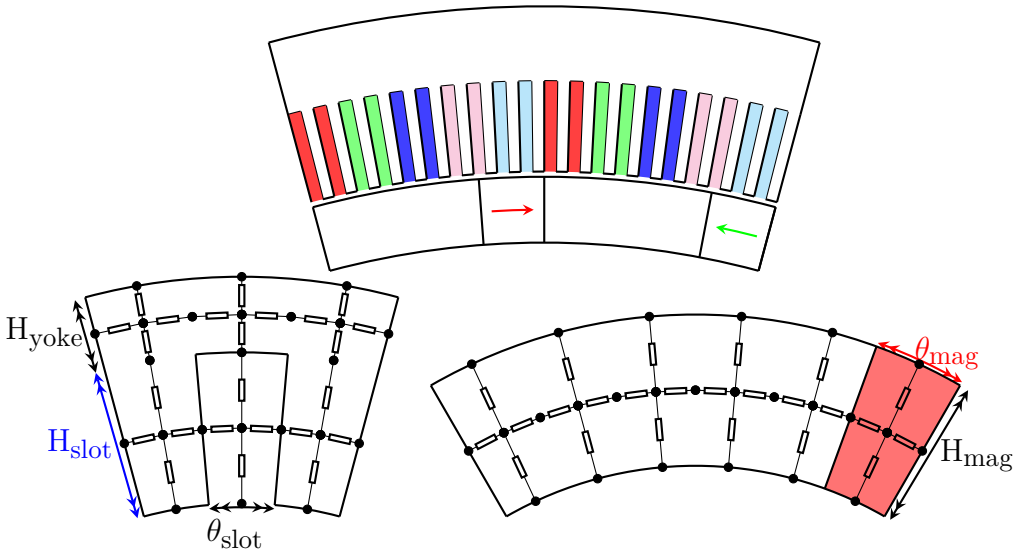

Fig. 3.5: View of concentrated flux machine and main geometric parameters

3.7.1.1 15 MW optimization results

Table 3.2: Optimization parameters (15 MW)

Fixed parameters		**Constraints**	**Objective functions**
Nominal speed	90 [rpm]	$\Gamma_{max} \geq 1.8 \times 10^6$[Nm]	$f_1 = \min(Mass_{PM})$
Poles / Slots	42 / 420		
Winding topology	Penta-Distributed	$T_{max} \leq 125$[°C]	$f_2 = \min(Mass_{all})$
Remanent field of PM	1.2 [T]		
Airgap	20 [mm]		
Bounds			
$\leq$[R_{mean}[m]; L_{act}[m]; J_s[A.m^{-2}]; θ_{slot}[°]; H_{slot}[m]; H_{yoke}[m]; θ_{mag}[°]; H_{mag}[m]]$\leq$			
[**1.7**; **1**; **2.5e6**; **0.34**; **0.1**; **0.04**; **0.85**; **0.05**]			
[**2.5**; **2**; **5e6**; **0.51**; **0.2**; **0.1**; **2.57**; **0.1**]			

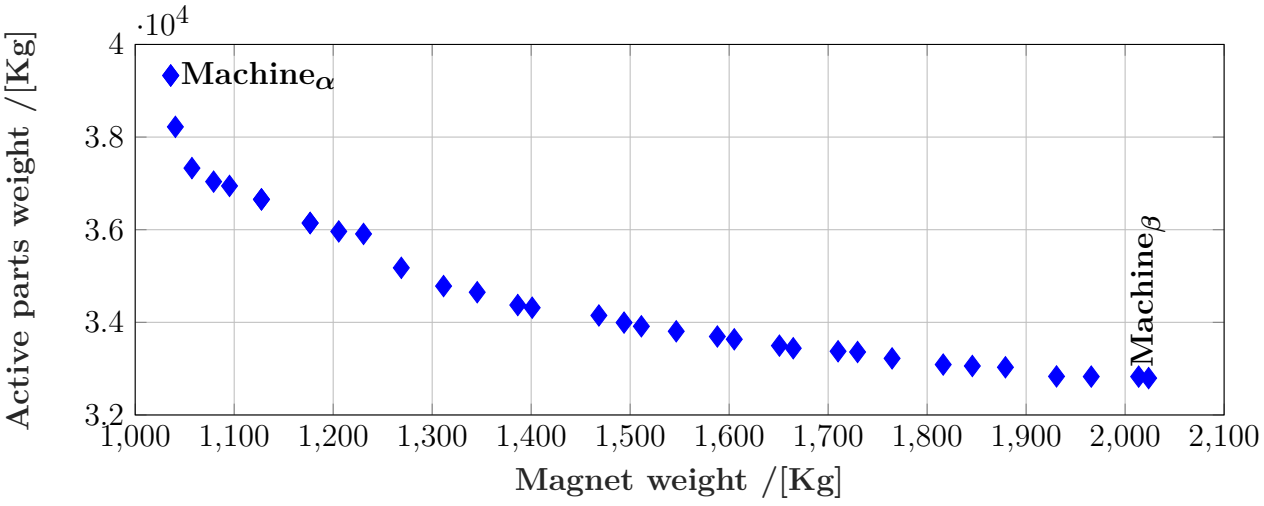

Fig. 3.6: Pareto optimality using NDFeB ($B_r = 1.2$[T])

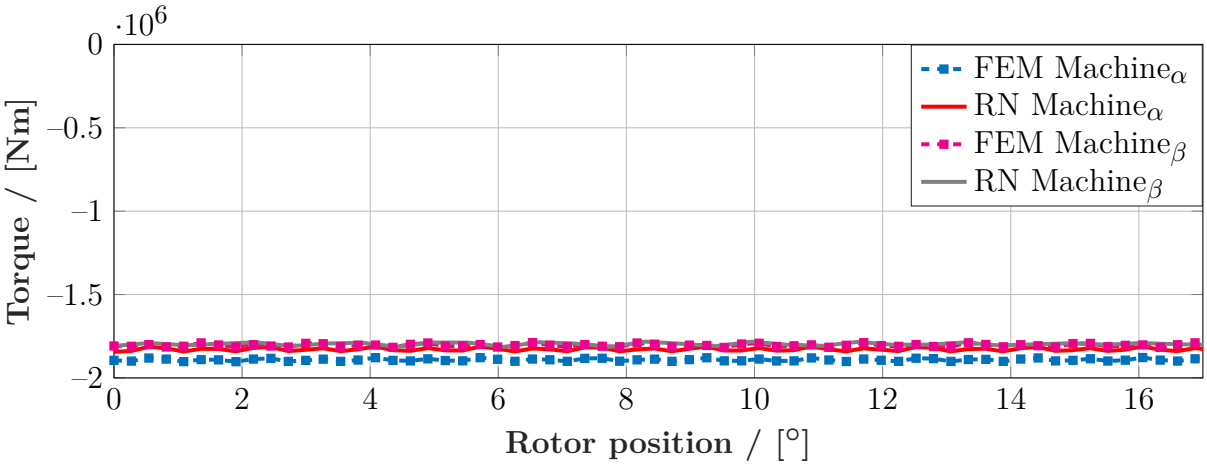

Fig. 3.7: Results validation (15MW)

Table 3.3: Comparison between FEM and the developed model results

	Γ_{mean} [MNm]	rms($\Gamma - \Gamma_{mean}$)[%Γ_{mean}]	T_{slot}	$Br_{corrected}$
Machine$_\alpha$ RN	–1.82	0.53	124	1.12
Machine$_\alpha$ FEM	–1.89	0.38	123	1.12
Machine$_\beta$ RN	–1.79	0.52	116	1.14
Machine$_\beta$ FEM	–1.80	0.46	118	1.14

Table 3.4: Active parts masses [kg]

	Copper Mass	Magnet Mass	Stator Iron Mass	Rotor Iron Mass
Machine$_\alpha$	9933	1035	20932	7482
Machine$_\beta$	8061	2023	16016	6693

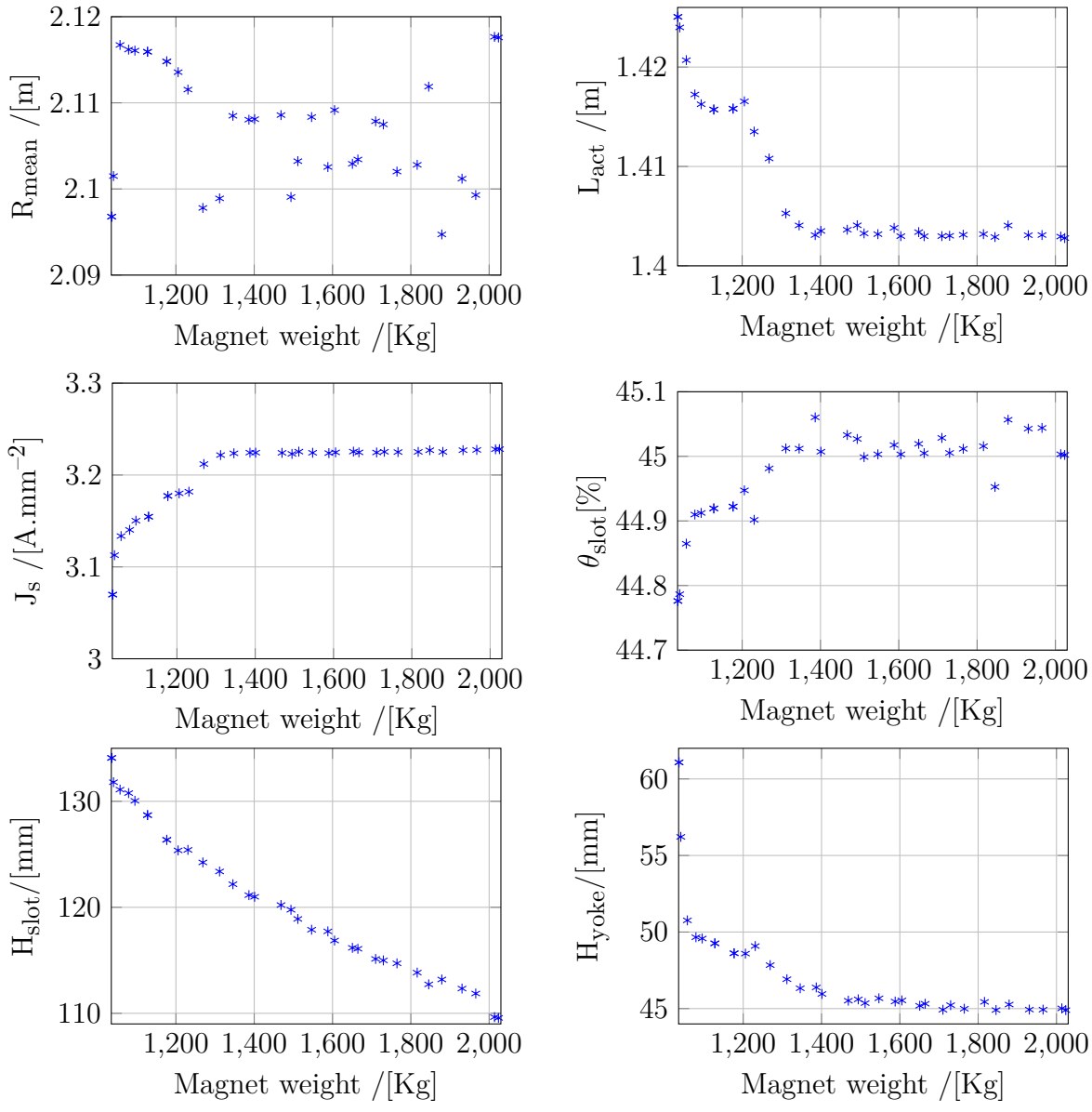

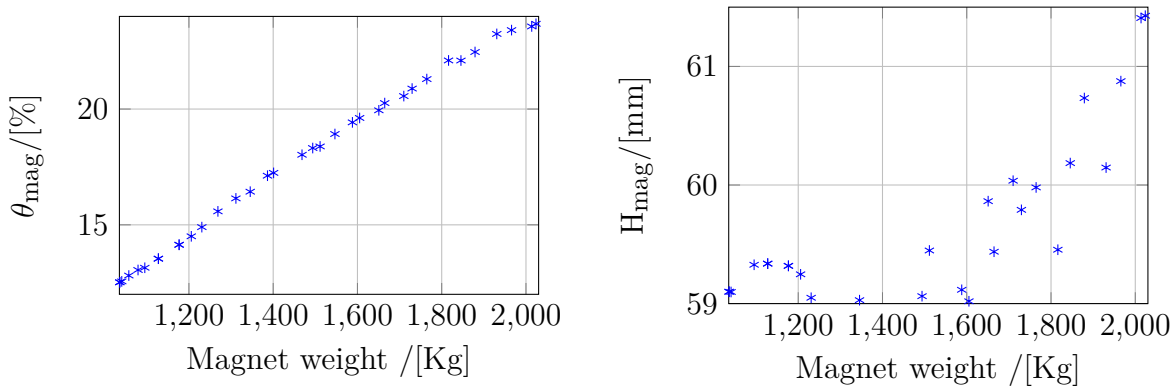

Fig. 3.8: Optimized machines parameters

3.7.1.2 8 MW optimization results

Table 3.5: Optimization parameters (8 MW)

Fixed parameters		**Constraints**	**Objective functions**
Nominal speed	350 [rpm]	$\Gamma_{max} \geq 2.7 \times 10^5$[Nm]	$f_1 = \min(Mass_{PM})$
Poles / Slots	24 / 240		
Winding topology	Penta-Distributed	$T_{max} \leq 125$[°C]	$f_2 = \min(Mass_{all})$
Remanent field of PM	1.2 [T]		
Airgap	10 [mm]		
Bounds			
$\leq$[R_{mean}[m]; L_{act}[m]; J_s[A.m^{-2}]; θ_{slot}[°]; H_{slot}[m]; H_{yoke}[m]; θ_{mag}[°]; H_{mag}[m]]$\leq$			
[**1.7**; **0.5**; **2.5e6**; **0.6**; **0.1**; **0.04**; **1.5**; **0.04**]			
[**2.5**; **2**; **5e6**; **0.9**; **0.2**; **0.1**; **4.5**; **0.1**]			

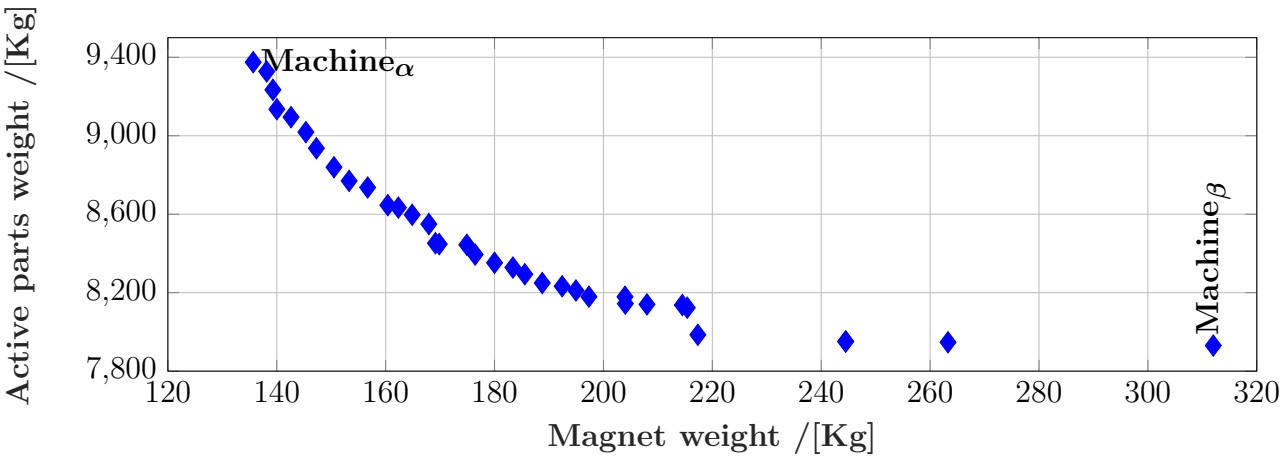

Fig. 3.9: Pareto optimality using NDFeB ($B_r = 1.2$[T])

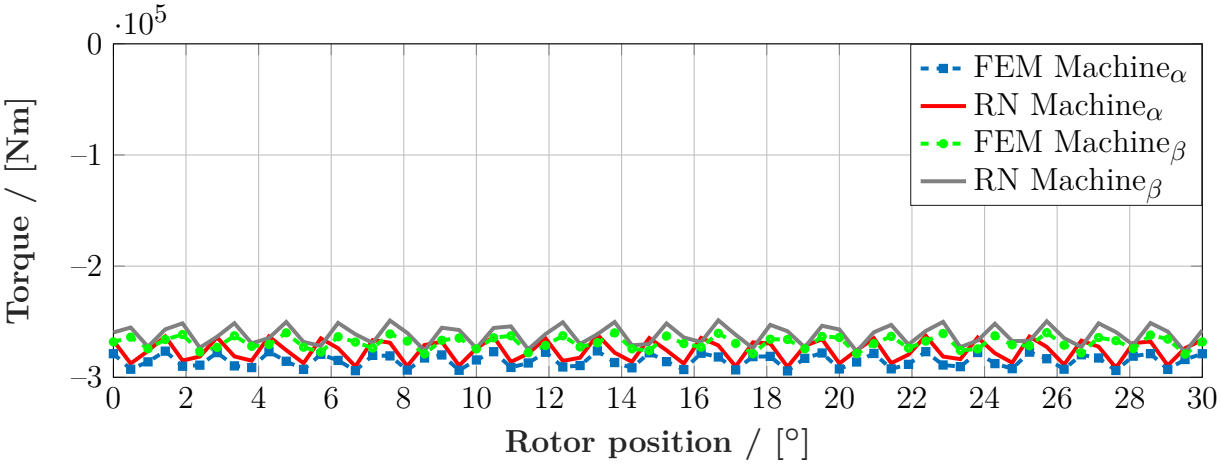

Fig. 3.10: Results validation (8MW)

Table 3.6: Comparison between FEM and the developed model results

	Γ_{mean} [kNm]	rms($\Gamma - \Gamma_{mean}$)[%Γ_{mean}]	T_{slot}	$B_{r_{corrected}}$
Machine$_\alpha$ RN	–267	2.10	117	1.11
Machine$_\alpha$ FEM	–275	3.21	117	1.11
Machine$_\beta$ RN	–261.7	3.32	118	1.11
Machine$_\beta$ FEM	–267	2.13	120	1.11

Table 3.7: Active parts masses [kg]

	Copper Mass	Magnet Mass	Stator Iron Mass	Rotor Iron Mass
Machine$_\alpha$	2793	138	5197	1200
Machine$_\beta$	2115	312	4015	1487

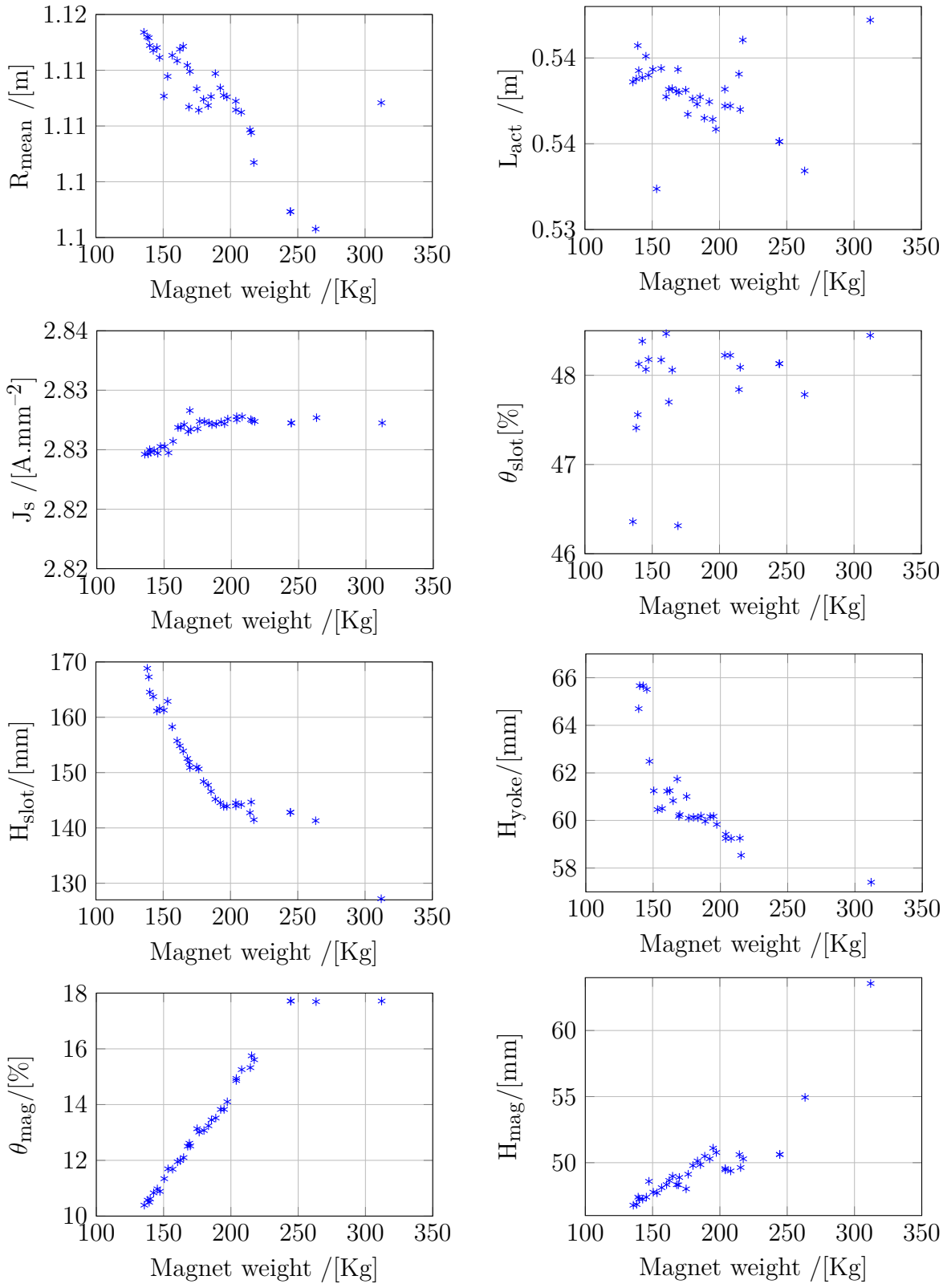

Fig. 3.11: Optimized machines parameters

3.7.1.3 5 MW optimization results

Table 3.8: Optimization parameters (5 MW)

Fixed parameters		**Constraints**	**Objective functions**
Nominal speed	135 [rpm]	$\Gamma_{max} \geq 4.2 \times 10^5$[Nm]	$f_1 = \min(Mass_{PM})$
Poles / Slots	24 / 240		
Winding topology	Penta-Distributed	$T_{max} \leq 125$[°C]	$f_2 = \min(Mass_{all})$
Remanent field of PM	1.2 [T]		
Airgap	8 [mm]		
Bounds			
[**1.7**; **0.5**; **2.5e6**; **0.6**; **0.1**; **0.04**; **1.5**; **0.05**]			
≤[R_{mean}[m]; L_{act}[m]; J_s[A.m^{-2}]; θ_{slot}[°]; H_{slot}[m]; H_{yoke}[m]; θ_{mag}[°]; H_{mag}[m]]≤			
[**2.5**; **2**; **5e6**; **0.9**; **0.2**; **0.1**; **4.5**; **0.1**]			

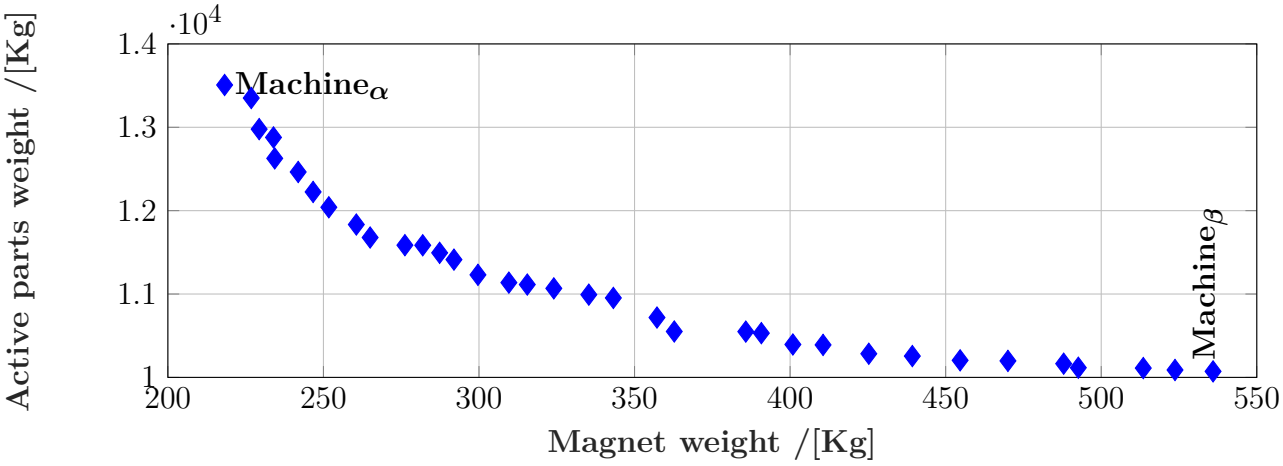

Fig. 3.12: Pareto optimality using NDFeB ($B_r = 1.2$[T])

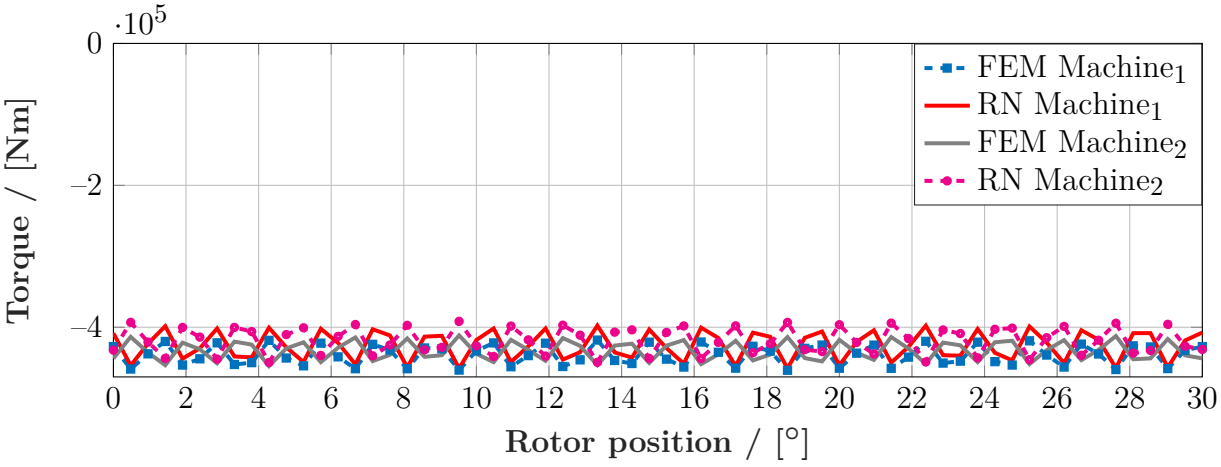

Fig. 3.13: Results validation (5MW)

Table 3.9: Comparison between FEM and the developed model results

	Γ_{mean} [kNm]	rms($\Gamma - \Gamma_{mean}$)[%Γ_{mean}]	T_{slot}	$Br_{corrected}$
Machine$_\alpha$ RN	–425	4.73	123	1.11
Machine$_\alpha$ FEM	–439	3.21	124	1.11
Machine$_\beta$ RN	–428	4.37	124	1.11
Machine$_\beta$ FEM	–433	3.09	123	1.11

Table 3.10: Active parts masses [kg]

	Copper Mass	Magnet Mass	Stator Iron Mass	Rotor Iron Mass
Machine$_\alpha$	3954	218	7486	1847
Machine$_\beta$	2800	535	5161	1575

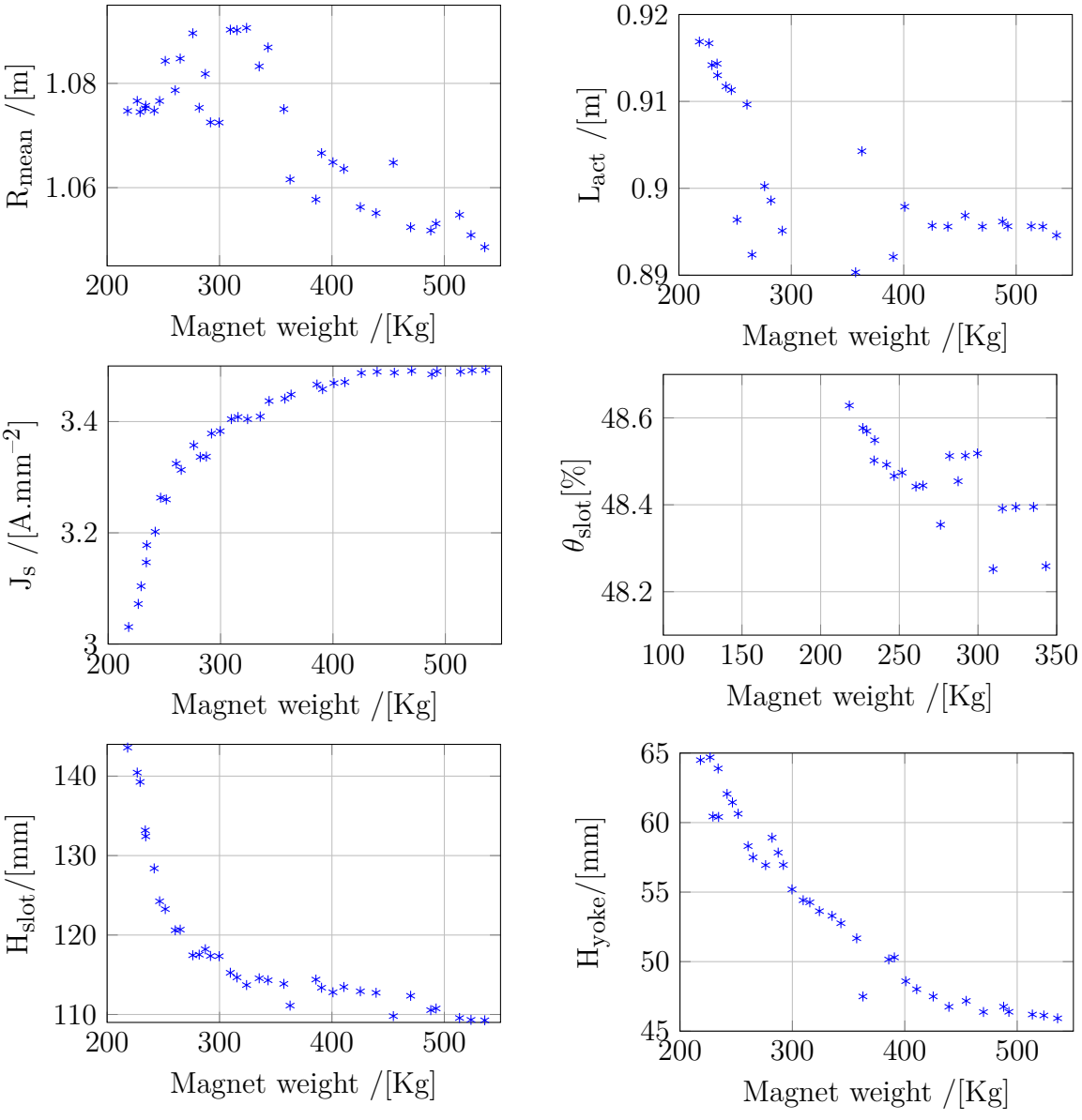

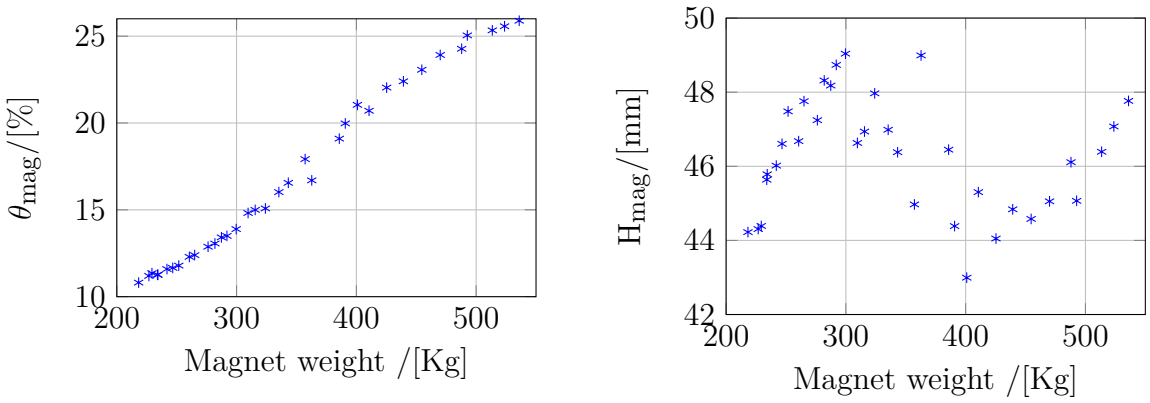

Fig. 3.14: Optimized machines parameters

3.7.2 Simulation and results for the surface mounted permanent magnet machine

Same observation as before can be conducted; first the higher the torque , the higher required materials which is logic from Fig. 3.16, Fig. 3.19 and Fig. 3.22. Stator mass represents between 74% and 69% for the 15 [MW], 75% and 77% for the 8 [MW] and 76% and 72% for the 5 [MW] as can be seen in Table. 3.13, Table. 3.16 and Table. 3.19. It can be stated as the concentrated flux generator that Table. 3.12, Table. 3.15 and Table. 3.18 show that using static torque computation did not affect the results that such since torque ripple are not that high, which saved a considerable computation time during the optimization process, however torque ripples are reduced in this structure compared to the previous one, since it doest represent a saliency $\mu_{\text{rPM}} = 1$. One can note also that the increase of magnets will reduce the slot's depth, which impacts directly copper and stator iron masses and reduces dramatically the required mass. It can be noticed also from Fig. 3.18, Fig. 3.21 and Fig. 3.24 that :

1. Air gap radius is stabilized around a mean value; 2, 1.1 and 1.2 [m] for respectively 15, 8 and 5 [MW] results, while the same can be noticed on active length. This is the consequence of optimization results, since the two major factor impacting global machine's weight are active length and radius, also this is related to torque's constraints, which is related directly to the square of air gap radius and active length, assuming a quasi-constant tangential pressure for Pareto front members.

2. Current density is bounded between 2.8 and 3.5 [A.mm–2], which seems logical for class H insulation, however it can be noticed that magnet parameters and slot's height are antagonist, since increasing magnet volume will allow the decrease of slot's height and thus copper and iron weight which results with a lighter machine compared to an other machine having less magnet volume.

3. Yoke thickness has the same variation with slot's height, this can be explained by the increase of magneto-motive force in the stator, thus a thicker yoke is needed in order to reduce saturation rate, this information couldn't be obtained without taking into consideration iron non-linearity, which justify the use of such model, since in linear model any yoke thickness will be sufficient.

4. A minimum of 2080, 480, 530 [Kg] of magnets is required in order to achieve the needed torques resulting density of 1155, 1777, 1260 [Kg of magnet/MNm] respectively with class H insulation and using the considered cooling method.

5. The global weight of the surface mounted machine is lighter than concentrated flux one, however the surface mounted machine requires more magnets, approximatively the double. This can be explained as follow:

   (a) In order to profit from the concentration flux phenomenon, the depth of the magnet must be at least equal to half of the rotor tooth angular length, which will require a magnet depth between 91 and 180 [mm], this will dramatically increase magnets weight and the rotor iron mass, since rotor weight is a square function of its thickness. This means that at no-load the magnetic flux density will not be favorable for the concentrated flux structure, compared to the surface mounted one. However, in the surface mounted machine, magnet thickness represents an additional air gap to stator magneto-motive force, which ot the case for the concentrated flux machine and thus represents one of its assets.

   (b) The surface mounted machine has more chance to be hotter than the concentrated flux one, since heat flux will be forced through the rotor in the surface mounted structure, while in the second one it will mainly go through the iron. This will allow more heat flux to the shaft and thus less thermal constraints, also magnets remanent flux density will have a slight drop in the surface mounted structure due to the extra thermal stress applied on the magnet

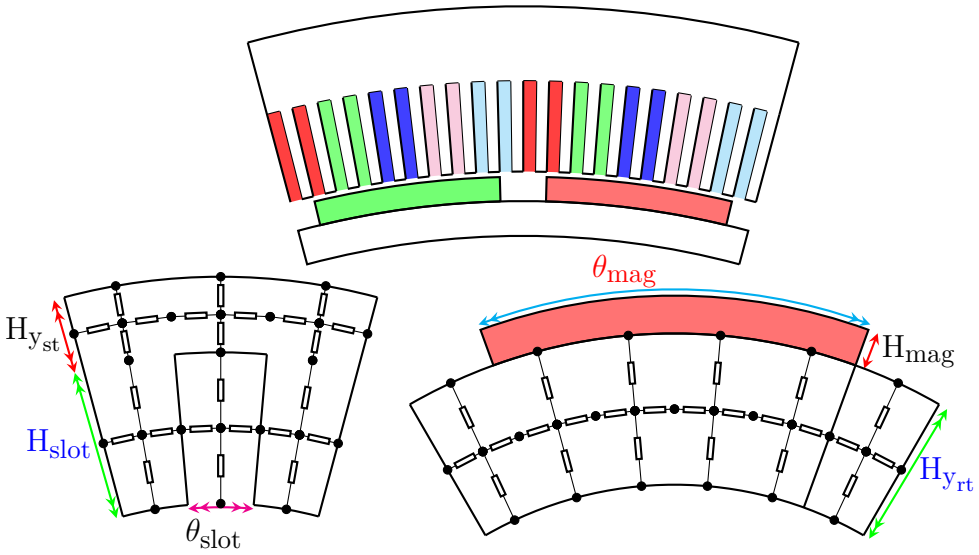

Fig. 3.15

3.7.2.1 15 MW optimization results

Table 3.11: Optimization parameters (15 MW)

Fixed parameters		**Constraints**	**Objective functions**
Nominal speed	90 [rpm]	$\Gamma_{max} \geq 1.8 \times 10^6$[Nm]	$f_1 = \min(Mass_{PM})$
Poles / Slots	24 / 240		
Winding topology	Penta-Distributed	$T_{max} \leq 125$[°C]	$f_2 = \min(Mass_{all})$
Remanent field of PM	1.2 [T]		
Airgap	20 [mm]		
Bounds			
$[\mathbf{1.5}; \mathbf{1}; \mathbf{2.5e6}; \mathbf{0.34}; \mathbf{0.1}; \mathbf{0.04}; \mathbf{6.86}; \mathbf{0.02}; \mathbf{0.03}]$			
$\leq [R_{mean}[m]; L_{act}[m]; J_s[A.m^{-2}]; \theta_{slot}[°]; H_{slot}[m]; H_{y_{st}}[m]; \theta_{mag}[°]; H_{mag}[m]; H_{y_{rt}}[m]] \leq$			
$[\mathbf{3}; \mathbf{2}; \mathbf{5e6}; \mathbf{0.51}; \mathbf{0.2}; \mathbf{0.1}; \mathbf{7.72}; \mathbf{0.06}; \mathbf{0.07}]$			

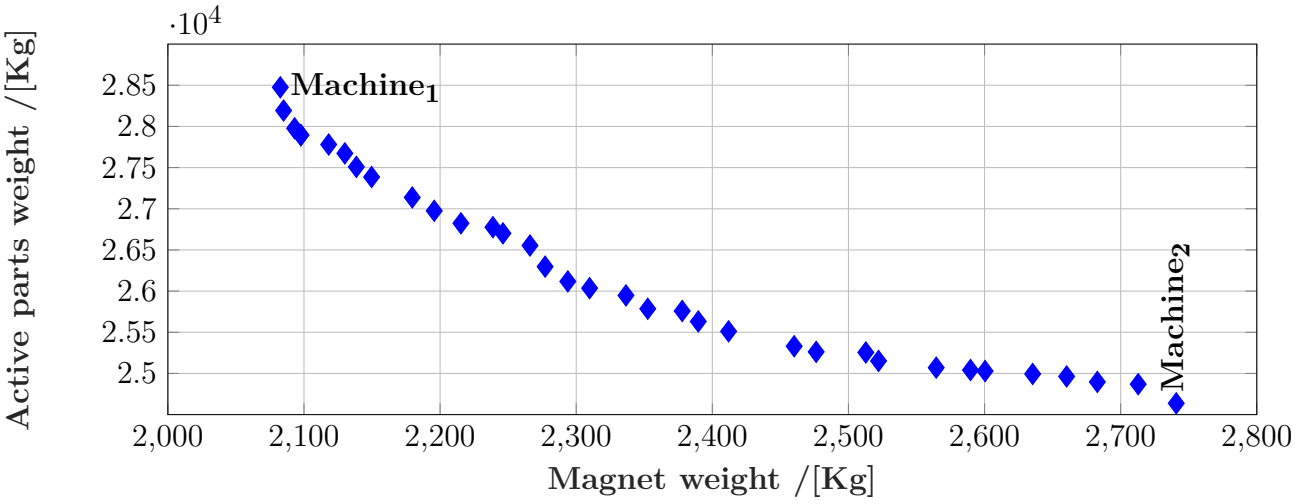

Fig. 3.16: Pareto optimality using NDFeB ($B_r = 1.2$[T])

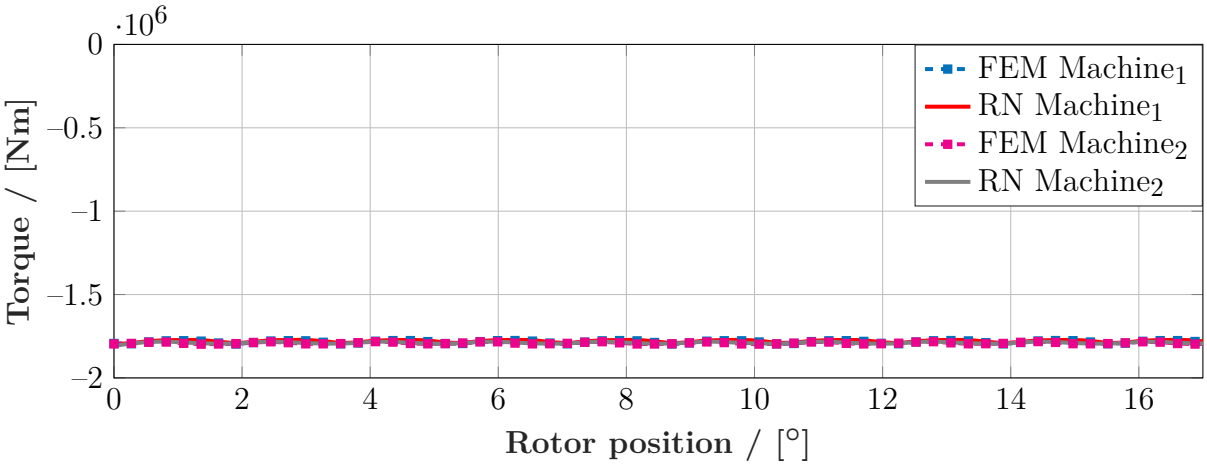

Fig. 3.17: Results validation (15MW)

Table 3.12: Comparison between FEM and the developed model results

	Γ_{mean} [MNm]	rms($\Gamma - \Gamma_{mean}$)[%Γ_{mean}]	T_{slot}	$Br_{corrected}$
$Machine_1$ RN	–1.77	0.41	124	1.11
$Machine_1$ FEM	–1.78	0.42	123	1.11
$Machine_2$ RN	–1.78	0.29	123	1.11
$Machine_2$ FEM	–1.79	0.27	123	1.11

Table 3.13: Active parts masses [kg]

	Copper Mass	Magnet Mass	Stator Iron Mass	Rotor Iron Mass
$Machine_1$	7775	2082	13397	5221
$Machine_2$	7080	2740	10721	4961

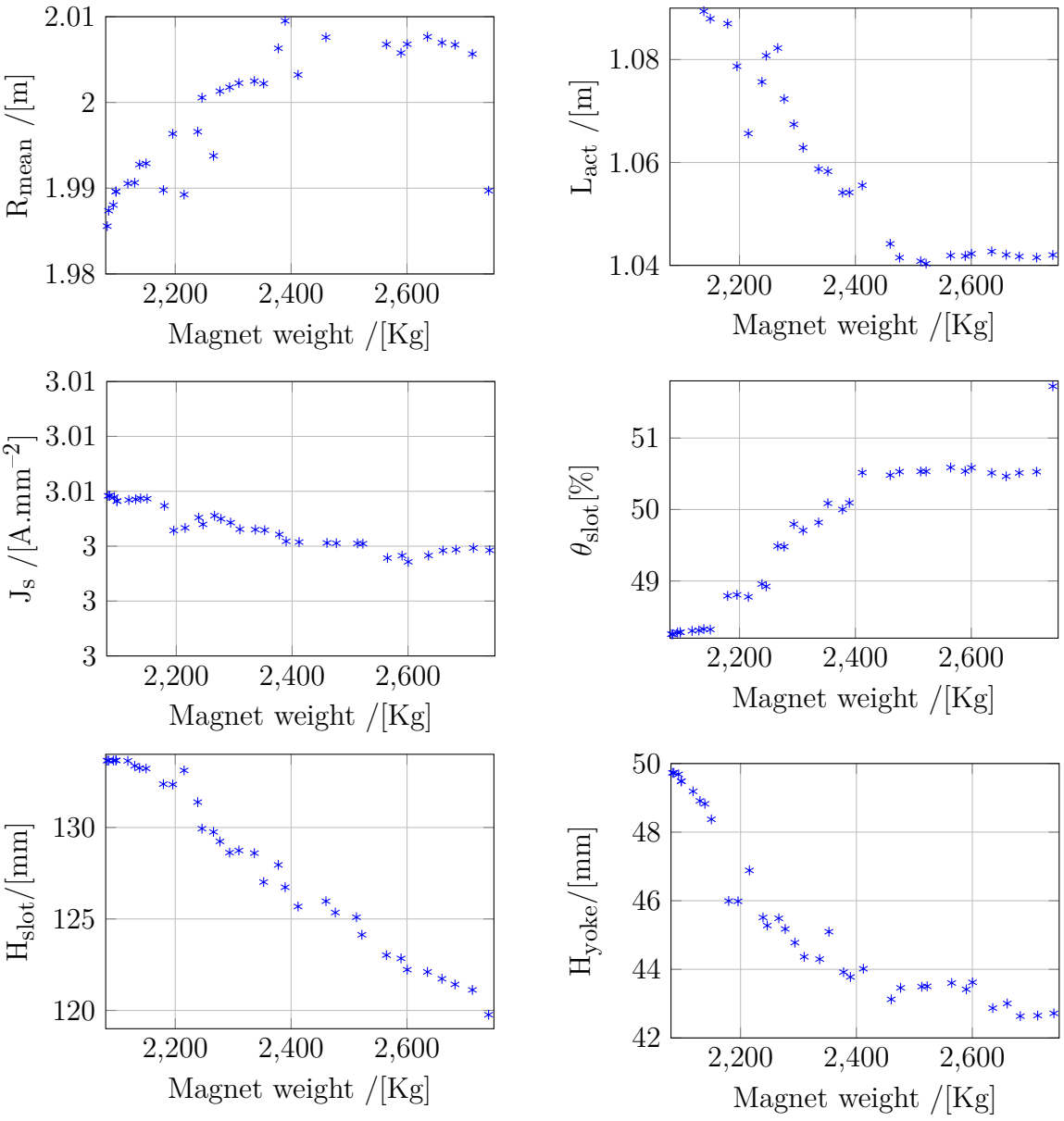

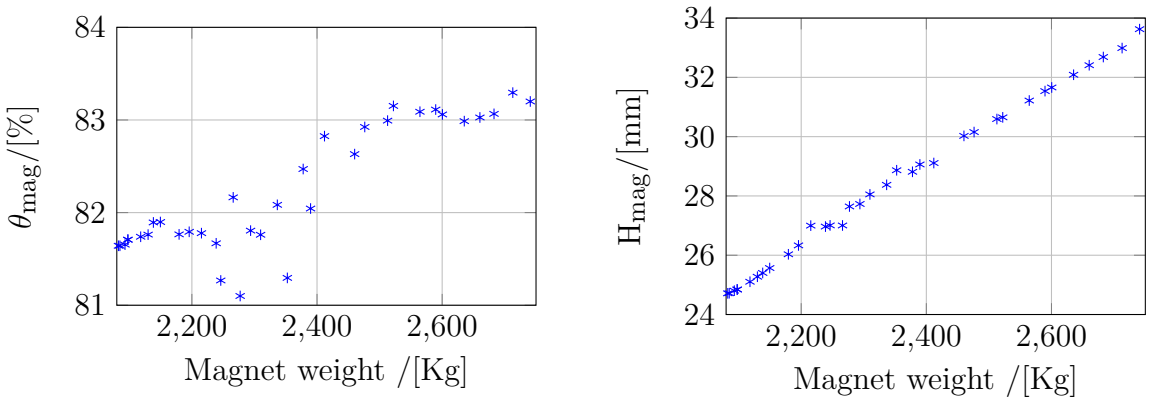

Fig. 3.18: Optimized machines parameters

3.7.2.2 8 MW optimization results

Table 3.14: Optimization parameters (8 MW)

Fixed parameters		**Constraints**	**Objective functions**
Nominal speed	350 [rpm]	$\Gamma_{max} \geq 2.7 \times 10^5$[Nm]	$f_1 = \min(Mass_{PM})$
Poles / Slots	24 / 240		
Winding topology	Penta-Distributed	$T_{max} \leq 125$[°C]	$f_2 = \min(Mass_{all})$
Remanent field of PM	1.2 [T]		
Airgap	10 [mm]		
Bounds			
[**0.8**; **0.5**; **2.5e6**; **0.6**; **0.1**; **0.04**; **12**; **0.02**; **0.03**]			
≤[R_{mean}[m]; L_{act}[m]; J_s[A.m^{-2}]; θ_{slot}[°]; H_{slot}[m]; $H_{y_{st}}$[m]; θ_{mag}[°]; H_{mag}[m]; $H_{y_{rt}}$[m]]≤			
[**2.5**; **2**; **5e6**; **0.9**; **0.2**; **0.1**; **13.5**; **0.06**; **0.07**]			

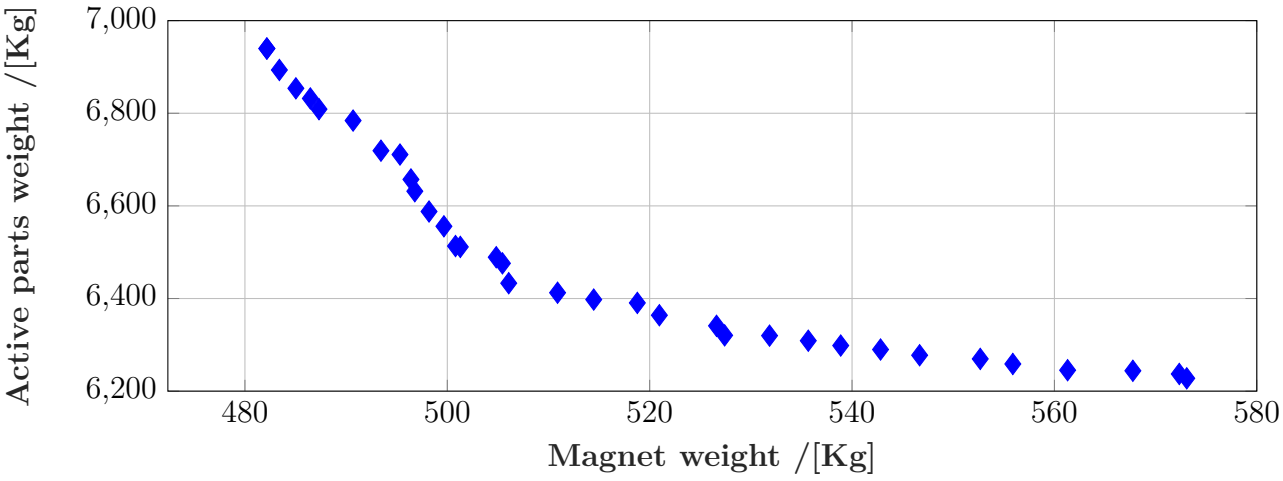

Fig. 3.19: Pareto optimality using NDFeB ($B_r = 1.2$[T])

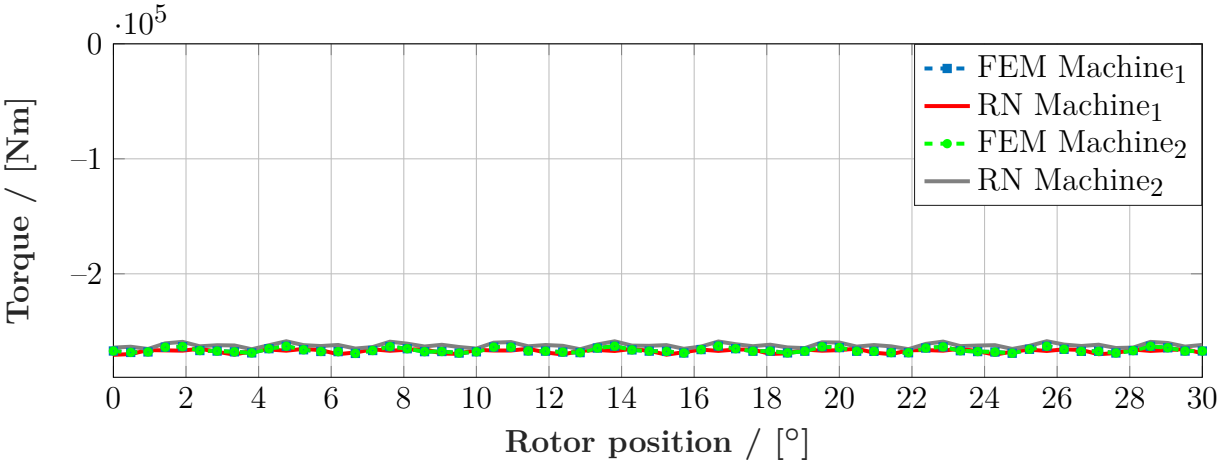

Fig. 3.20: Results validation (8MW)

Table 3.15: Comparison between FEM and the developed model results

	Γ_{mean} [kNm]	rms($\Gamma - \Gamma_{mean}$)[%Γ_{mean}]	T_{slot}	$B_{r_{corrected}}$
$Machine_1$ RN	−274	0.6144	121	1.12
$Machine_1$ FEM	−275	0.7557	120	1.12
$Machine_2$ RN	−272	0.7445	112	1.13
$Machine_2$ FEM	−276	0.7136	112	1.13

Table 3.16: Active parts masses [kg]

	Copper Mass	Magnet Mass	Stator Iron Mass	Rotor Iron Mass
$Machine_1$	1818	482	3422	1216
$Machine_2$	1743	573	2987	923

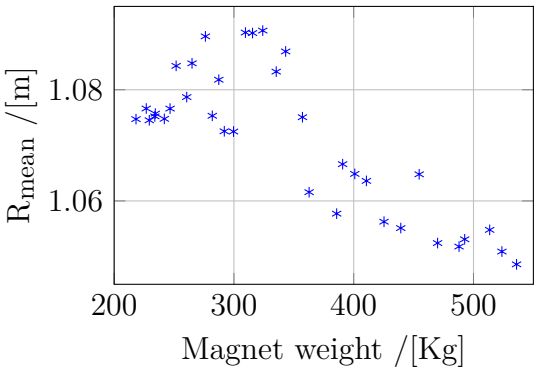

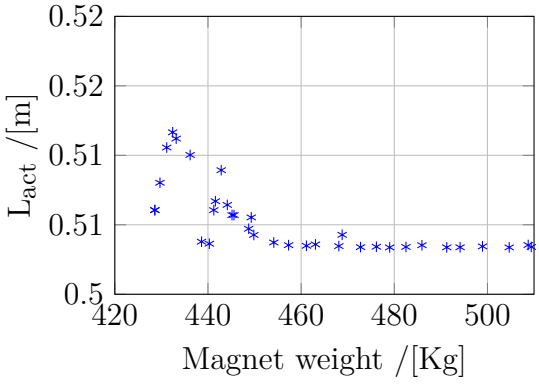

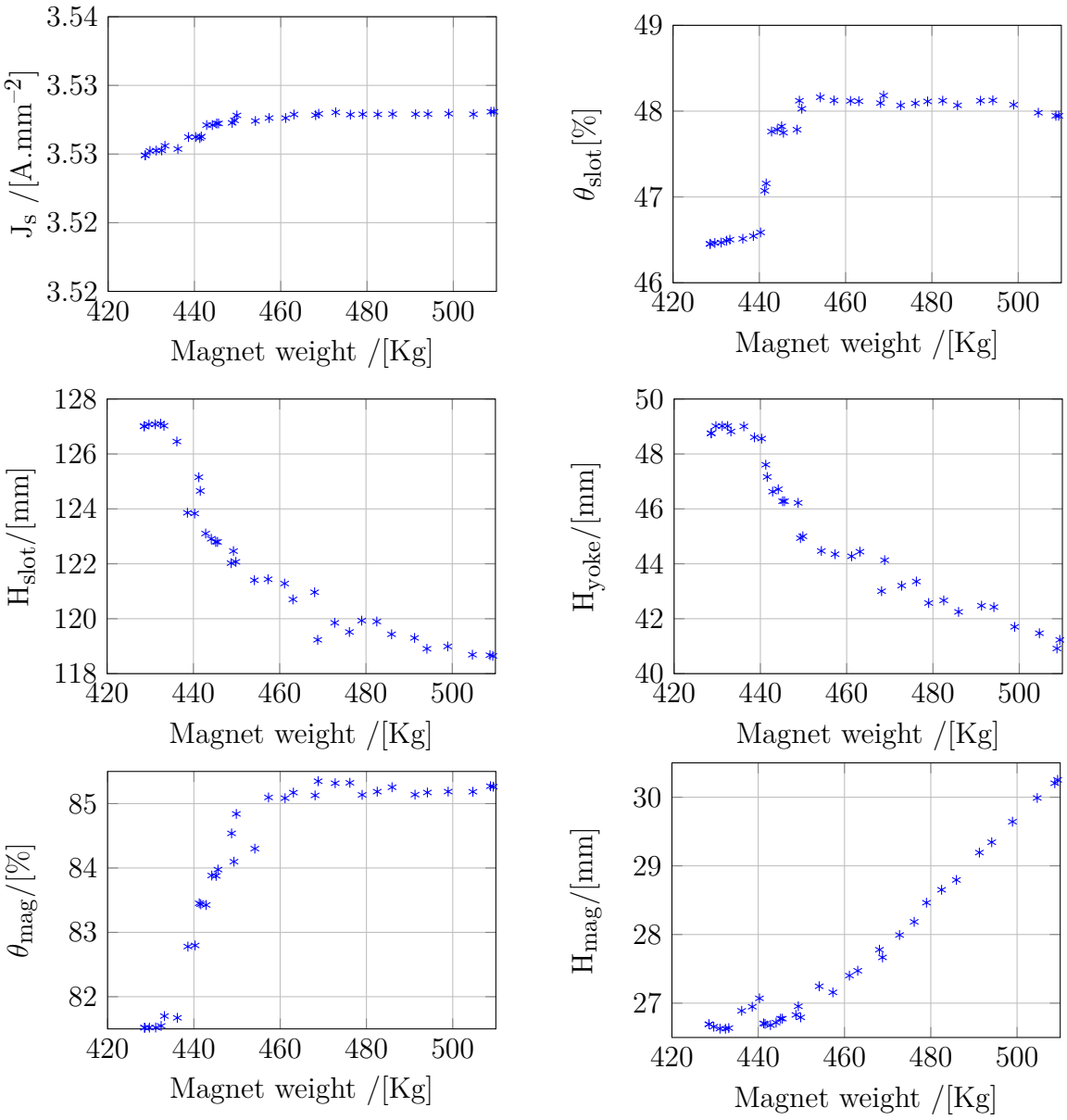

Fig. 3.21: Optimized machines parameters

3.7.2.3 5 MW optimization results

Table 3.17: Optimization parameters (5 MW)

Fixed parameters		**Constraints**	**Objective functions**
Nominal speed	135 [rpm]	$\Gamma_{max} \geq 4.2 \times 10^5$[Nm]	$f_1 = \min(Mass_{PM})$
Poles / Slots	24 / 240		
Winding topology	Penta-Distributed	$T_{max} \leq 125$[°C]	$f_2 = \min(Mass_{all})$
Remanent field of PM	1.2 [T]		
Airgap	8 [mm]		
Bounds			
[**0.8**; **0.5**; **2.5e6**; **0.6**; **0.1**; **0.04**; **12**; **0.02**; **0.03**]			
$\leq$[R_{mean}[m]; L_{act}[m]; J_s[A.m^{-2}]; θ_{slot}[°]; H_{slot}[m]; $H_{y_{st}}$[m]; θ_{mag}[°]; H_{mag}[m]; $H_{y_{rt}}$[m]]$\leq$			
[**2.5**; **2**; **5e6**; **0.9**; **0.2**; **0.1**; **13.5**; **0.06**; **0.07**]			

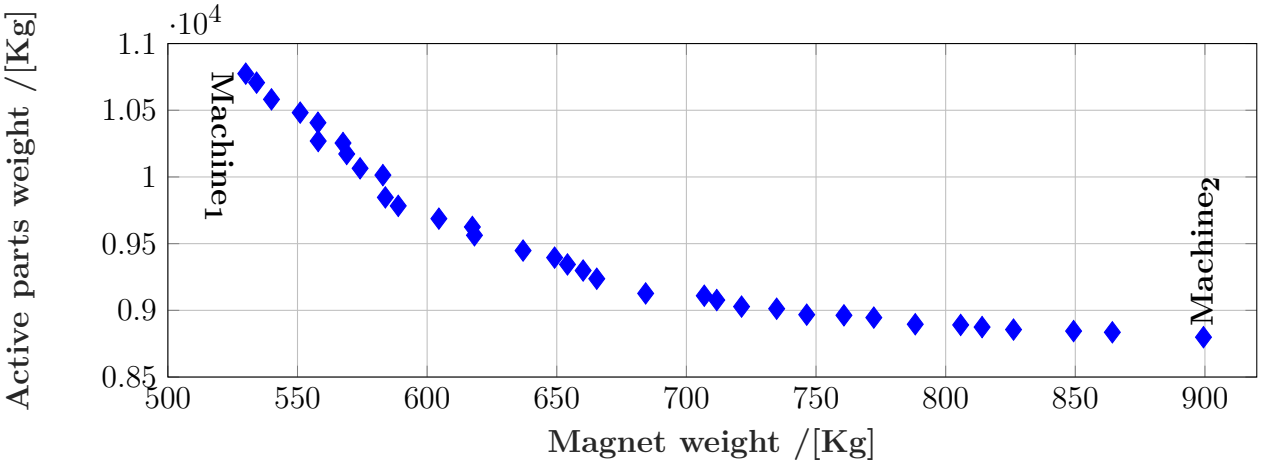

Fig. 3.22: Pareto optimality using NDFeB ($B_r = 1.2$[T])

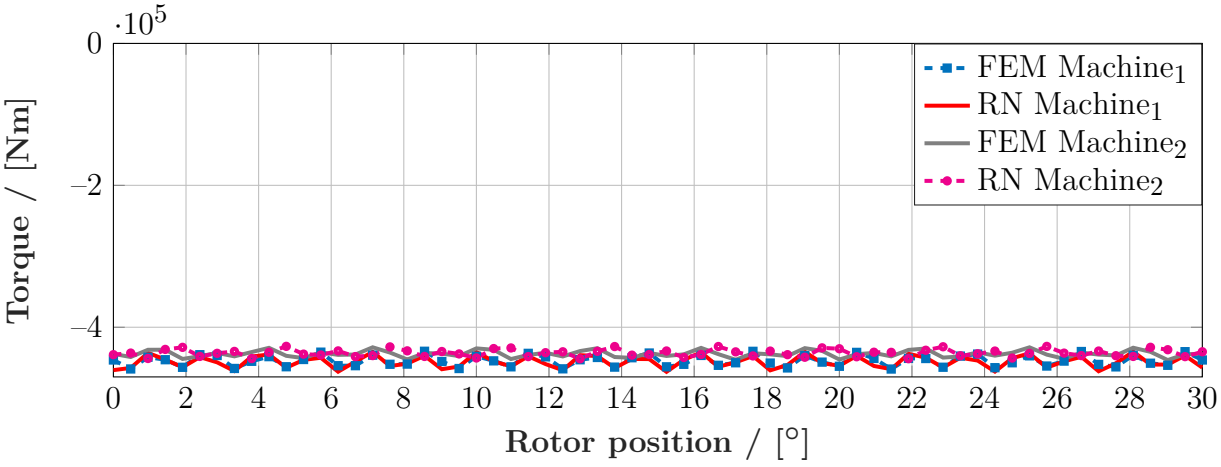

Fig. 3.23: Results validation (5MW)

Table 3.18: Comparison between FEM and the developed model results

	Γ_{mean} [kNm]	rms$(\Gamma - \Gamma_{mean})[\%\Gamma_{mean}]$	T_{slot}	$B_{r_{corrected}}$
$Machine_1$ using RN	–448	1.9	123	1.11
$Machine_1$ using FEM	–447	1.71	123	1.11
$Machine_2$ using RN	–436	1.16	112	1.12
$Machine_2$ using FEM	–437	1.11	113	1.12

Table 3.19: Active parts masses [kg]

	Copper Mass	Magnet Mass	Stator Iron Mass	Rotor Iron Mass
$Machine_1$	3033	530	5216	1985
$Machine_2$	2505	1025	3677	1356

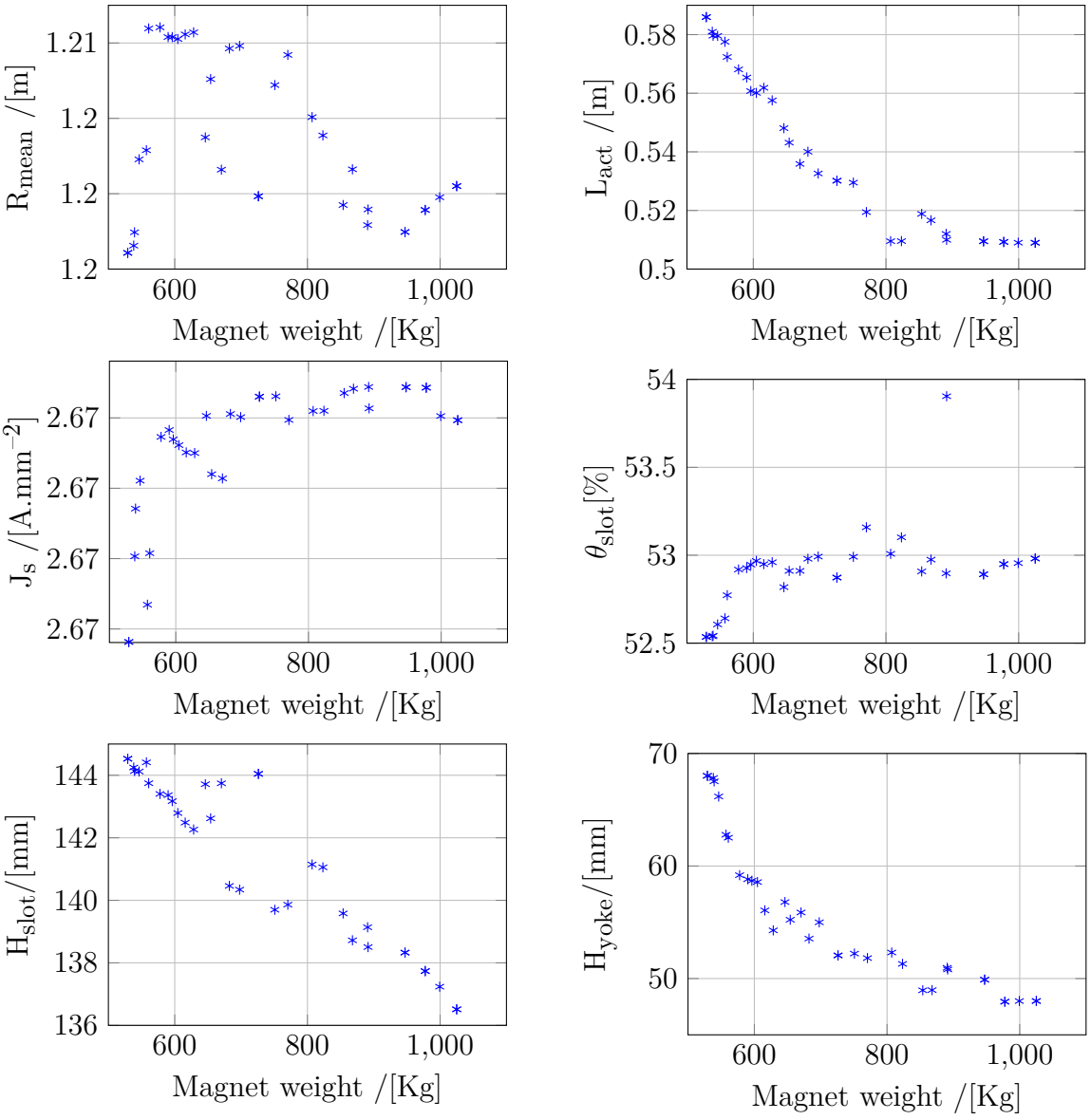

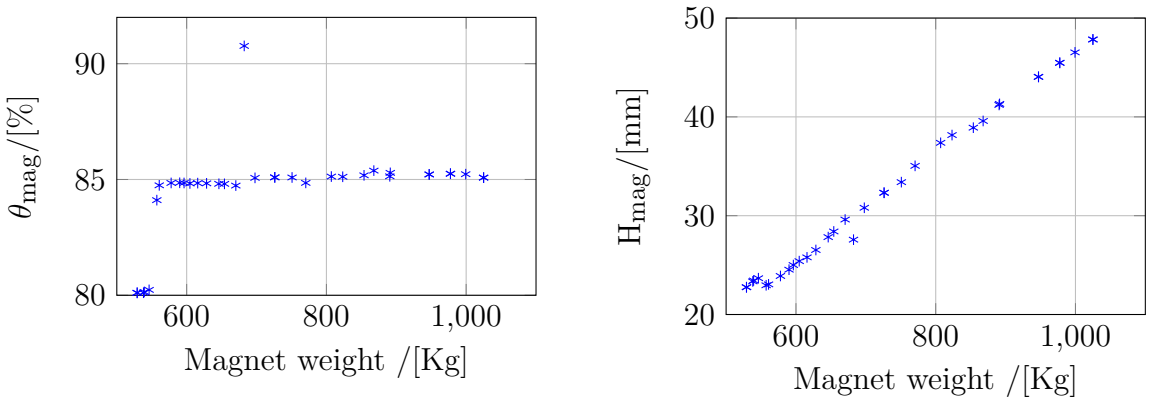

Fig. 3.24: Optimized machines parameters

Conclusion

This chapter presented an optimal design procedure for multi-megawatt generator. As first conclusion, there is no perfect optimization algorithm, it depends on the used model or software, stage of the design, available resources (computation machines) and complexity of the studied function. As can be seen in benchmark function, multiple problems can lead to a false minimum especially if gradient algorithm are used, which justify the use of evolutionary algorithms such as genetic one and particle swarm as can be seen in the listed previous optimization works on electrical machine.
The developed model allows a good comprise in computation time thanks to its fastness and parallel programing, which gives a respectable Pareto front in 48h hours knowing that for each machine a thermal step computation and sixteen magnetic one are performed for hundred machine among two-hundred generations, which results by 0.5 sec/step with all magneto-thermal non linearity.
One can notice that a compromise must be made between reducing magnets mass and total machine weight. Since magnets mass reduction must be compensated by increasing copper volume, which increases magneto-motive force (MMF), characterized by the heaviest mass density and resulting in a considerable increase of machine's active parts mass. In general matter, 500 [kg] of rare earth magnet are needed for each requested 1[MNm] of torque for the concentrated flux permanenet magnet machine, while this value increases near 1600 [kg] for the surface mounted one if the class H insulation and a cooling with a mean convection coefficient of 800 [$W.K^{-1}.m^{-2}$] are used
One must be careful interpreting optimization results since iron and eddy current losses are not taken into consideration. However, since the magnetic circuit is not highly saturated and operates at low frequency , around 31 [Hz] for both 5 and 15 [MW], and knowing losses are generated in the core, which is relatively good thermal conductor, iron losses are not expected to increase dramatically machine's temperature. Meanwhile, eddy current losses may increase the temperature in the case of rare earth magnet, this is caused by their relatively good electrical conductivity, which may decrease more their remanent flux density. Finally demagnetization effect must be also taken into consideration in more refined future study using 3D FEM, in order to protect magnets from eventual local or global demagnetization, which will affect final results and thus machines design. For all those reasons the design was over-sized, thermally leaving a gap of 40 [°C] for class H insulation and magnetically by adding 10% supplementary torque in order to overcome the listed previous phenomena.
It can be noticed that the studied topologies are geared and a look on the direct drive structures must be carried out, all of this with a quick estimation on the influence of poles number on the global weight, since concentrated flux machines should be beneficial at high poles number. A quick study on insulation class influence on machines characteristics may help the designer, in order to estimate the increase of weight for the same cooling characteristics, which will be done on the next chapter with a quick study on magnetic gear integration in this type of energy conversion.

Chapter 4

Magnetically geared or direct drive topology ?

Introduction

A large industrial applications extremely use gears and gearboxes for speed variation and torque transmissions. Thus a question remains: Magnetic gear integration investigation or direct drive structure which one to use? . In order to find its solution, first mechanical gear used in wind energy will be defined followed by a non-exhaustive list of their drawbacks, which most of them are avoided by magnetic gear solution. After that, magnetic gear will be explained with its operating mode accompanied by definition of main parameters such as poles number on high and low speed shaft and the number of ferromagnetic pieces. Second an optimal design will be performed on magnetic gear for three different ratios and for a power of 8 [MW], leading to an approximation of rare earth permanent magnets weight for each requested [MNm]. Finally, These torque densities will be compared with those of direct drive concentrated flux machines, obtained through the same optimal design carried in previous chapter allowing to identify the solution requesting less rare earth permanent magnet for each [MNm] of torque. Optimal magnetic gear results will be compared with commercial software ones, while the same will be done on randomly selected machine from each obtained Pareto front for direct drive results.

4.1 Mechanical gears used in wind energy : generalities

The main goal of this section is to briefly introduce mechanical gears used in wind turbine with their accompanied by expensive maintenance costs, which can be counted as an introduction to the next section dealing with magnetic gear. This can be a quick satisfying answer to the following question; why should we use magnetic gear instead of mechanical ones, what gain is added to wind energy conversion chain with such solution.
Unlike direct drive, indirect wind turbine conversion chain includes mechanical gear in order to increase generator speed and reduce requested torque and thus its volume and weight. However according to [131, 132] gearbox failure attracted industrial attention since it is accompanied by repair expensive costs since its downtime is relatively high, even though its failure rate is low, as illustrated in Fig. 4.1. As a result, the percentage of

electricity production lost due to gearbox downtime is the highest of all sub-assemblies. [133] confirms the previous statement affirming that gear oil pump has the highest failure rate in mechanical gear, while [134] stated that high speed shaft represents the highest failure rate, knowing that for offshore situation a specialized trained personal is needed for long stable weather window in order to repair the damaged component. For these reasons more models based on statistics or loads are used in order to predict gearbox failures, which can stop the wind turbine production up to 12 days [135]. Most of the listed failures are related to planetary gearbox and are not specific to one manufacture which make them generic and attract scientific researchers curiosity [136], this gear type is the most used in commercialized wind turbines[137] such in ; Adwen AD8-180 [138], MHI Vestas Offshore V164-8.0 MW, 9.0 MW, 9.5 MW [139]

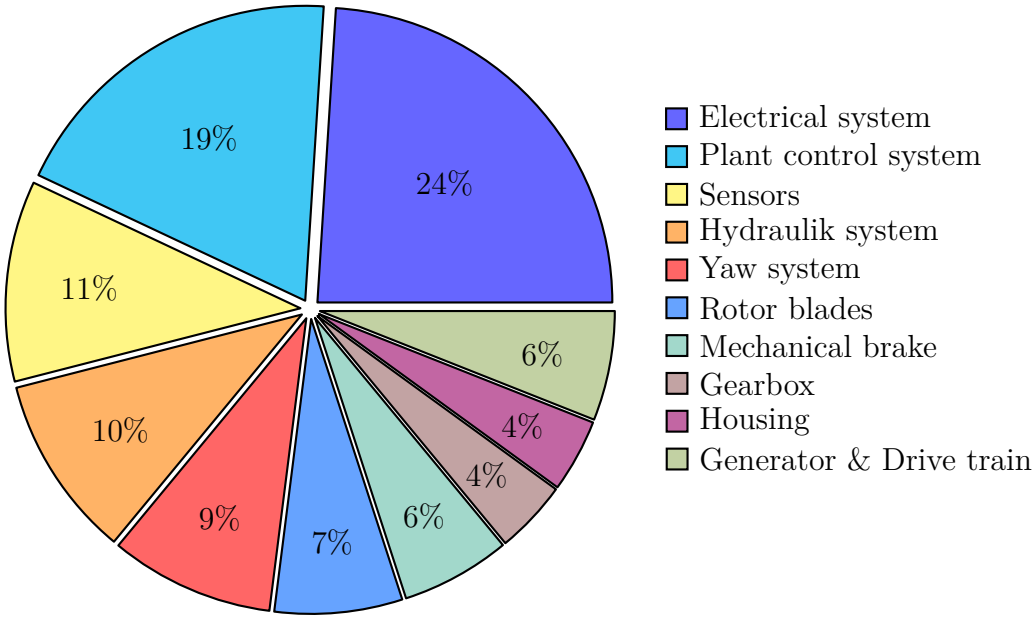

Fig. 4.1: Main components of the total number of failures for wind turbine subsystems

The epicyclic or planetary gearbox consists of a sun gear, planet gears supported by the carrier and a ring gear, as can be illustrated in Fig. 4.3. It offers several advantages compared to the parallel-shaft configuration [140], including a higher gear ratio in a smaller “package.” This compact configuration has the advantage of reducing the overall mass of the gearbox, which is an important requirement for wind turbine gearboxes, because the head mass of the turbine is kept to a minimum. Additionally, the planetary configuration has the capability of handling greater torque loads. This is because the load is distributed or shared by the number of planet gears, therefore more teeth always are in contact. Another advantage is its geometrical configuration. The input and output have a concentric axis and the same rotational direction; therefore, it is very simple to build multistage planetary boxes that maintain a streamlined and compact design.

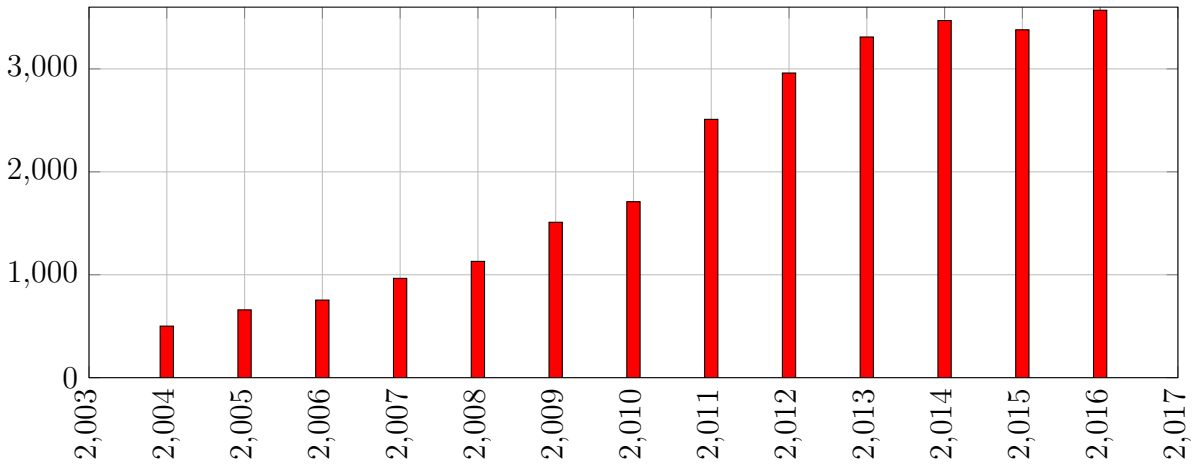

Fig. 4.2: Publication related to mechanical gear failures

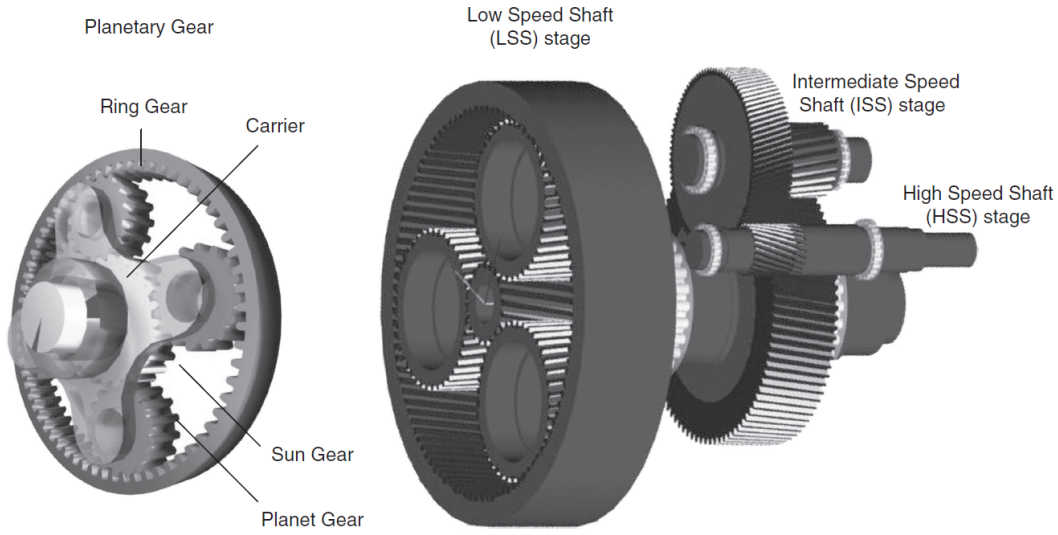

Fig. 4.3: Planetary gearbox illustration [141]

Fig. 4.2 illustrated the growth of interest in mechanical gear failures, according to google scholar, which are linked to the listed causes given in [142]. This leads us to magnetic gear solution since it proposes torque transmission and multiplication without contact, which will be introduced and explained next. These failures pushed wind turbine manufacturers to use direct drive solution, such as : SeaTitan 10 MW [53], Siemens SWT-7.0-154 [55], Enercon E-126 [29], in order to avoid mechanical gear box and its accompanied drawbacks and to reduce structural components.

4.2 Magnetic gears

Magnetic gear seems to be a good alternative to mechanic one since it offers an interesting amount of advantages, which are listed below, and provides contactless torque transmission; avoiding surface fatigue and natural protection to overloads. Many structures were

proposed in the literature since 1900 [143], which have been developed through the time and had a constant growth of interest by the scientific community, as can be seen in Fig. 4.5 according to google scholar search results. The structure proposed in [144] took most of the interest since it represents a high torque density up to 100 [kNm.m^{-3}]. This structure is composed from three main parts as illustrated in Fig. 4.4

1. An inner annular with permanent magnets, having n_1 pairs of poles.
2. An outer annular rotor with permanent magnets n_2 pairs of poles.
3. Ferromagnetic pieces sandwiched between the two annulars with n_3 poles.

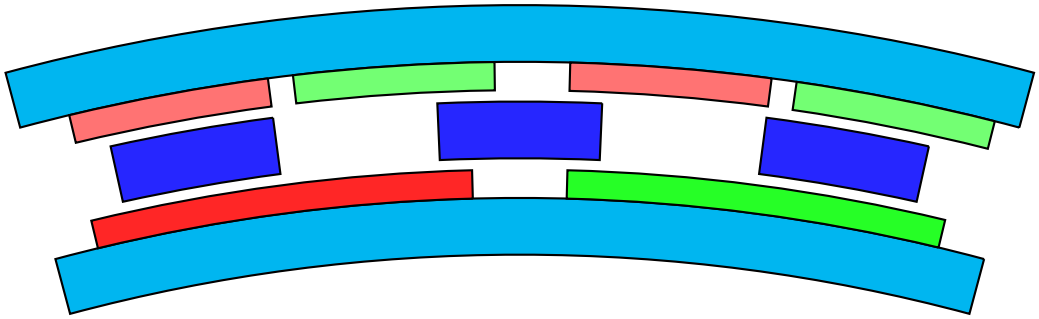

Fig. 4.4: Topology proposed in [144]

For this topology at least two of the three main parts must be in rotation, in general the Low Speed Shaft (LSS) is located at the outer annular which will provide more torque since it has the highest mean radius, where Hight Speed Shaft (HSS) can be either located at ferromagnetic pieces or at the inner annular. Gear ratio is dependent on which moving parts choice, As stated in [145] if the ferromagnetic parts are moving while the inner annular is static the gear ratio G_r is given in (4.1).

$$G_r = \frac{n_1 - n_3}{n_3} \tag{4.1}$$

While if the ferromagnetic pieces are static with a rotation of the inner annular, the ratio will be changed as given in (4.2). For maximum torque production in this case, the number of poles n_3 must be equal to sum of poles pairs number in inner and outer annulars, as expressed in 4.3.

$$G_r = \frac{n_1}{n_2} \tag{4.2}$$

$$n_3 = n_1 + n_2 \tag{4.3}$$

Most of the advantages offered by this magnetic gear topology [146] are as follows:

Frictionless torque transfer Since the process of transmuting torque is achieved through magnetic field, which eliminates wear and losses related to mechanical gear teeth

Low maintenance Comparing it to mechanical gear, only lubrication on its bearing is needed.

Overload protection When maximum torque is exceeded magnetic gear slips which constitutes a natural protection for itself and for other component in the drive train. On the contrary, mechanical gears transmits the overload, which can cause severe damages.

Reduced noise Theoretically, magnetic gears are expected to be less noisy due to the absence of tooth contact.

High-efficiency It is a consequence of contestable transfer which reduces losses and thus increases efficiency.

However the requirement of rare earth permanent magnets, immaturity of technologies, lack of stiffness and the relatively challenging construction and assembly since three parts must be assembled constitutes drawbacks of this magnetic gear. These drawbacks are more related to industry and the investment required for it, for which we are not well positioned to estimate and only technical aspect of magnetic gear will be studied. However, torque density may be a good indicator, which needs an optimal design study on the selected structure.

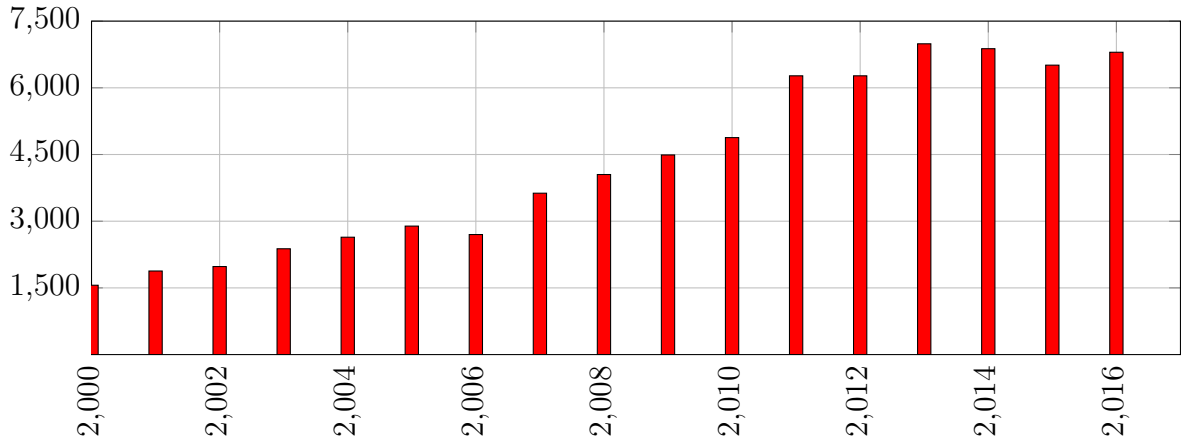

Fig. 4.5: Publication related to magnetic gear design

Table. 4.1 contains a non-exhaustive list of magnetic gear prototypes, where the use of rare earth magnets is directly linked to higher torque densities. Most of the listed authors found up to 40[%] difference between 2-D finite element study and measurement, which are related to end effect.

Table 4.1: Magnetic gear prototypes

Reference	External diameter [mm]	Gear ratio	Torque density [kNm.m^{-3}]
[145]	140	5.75	72
[147]	120	5.5	42
[148] (Ferrite)	112	4.25	33
[148] (Ferrite + NdFeB)	112	4.25	66
[149]	120	5.5	92

4.3 Simulation and results discussion

The goal of these simulations is to investigate the integration of permanent magnet gears usage in wind turbine drive. In order to achieve it, an optimal design for magnetic gear will be carried first, where the focus will be on the reduction of magnets weight, which requires only a mono-objective minimization. Second, torque density of optimally designed direct drive concentrated flux machine will be compared with magnetic gear one.

4.3.1 Magnetic gear

As said previously, Magnetic gear solution is quite attractive, especially when it comes to eliminating the most undesirable mechanical drawbacks. However, since magnets are the mos valuable component and expensive one in this structure, an idea of the required amount for a given ratio and power will be welcomed. This last information will either favorite the use of such structure and may open the doors for an integrated structures combining magnetic gear and the electrical generator, or prefer a direct drive structure. In order to do so, optimizations were carried out with a close look on magnets weight reduction on the structure represented in Fig. 4.6 (the magnetic gear has a ration of 1:2 only for illustration). Torques in both high and low speed shaft were computed thanks to the developped model in Chapter2. In this case three independent reluctance networks were used connected through interpolation procedure (Low speed shaft/ ferromagnetic parts and High speed shaft/ ferromagnetic parts). The fixed parameters for this study are given in Table. 4.2, assuming that airgaps values overcome the potential mechanical constraints.

Table 4.2: Fixed parameters during optimization

Low speed airgap	6 [mm]
High speed airgap	6 [mm]
Steel lamination	M440-50A
Magnets	NDFeB 1.2[T] @ 20[°]

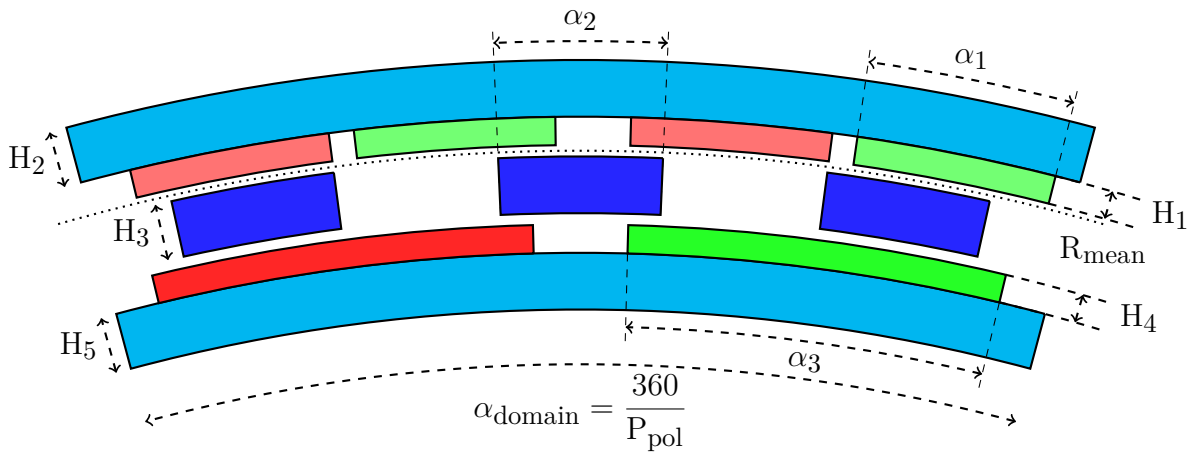

Fig. 4.6: Main parameter of the studied magnetic gear

Eleven variables given in Table. 4.3 were chosen with their respective boundaries. Where R_{mean} is the mean airgap radius of low speed shaft, while L_{act} is the active length among z axis.

Table 4.3: Optimizations variables and their ranges

Variable	Lower bound	Upper bound
General		
R_{mean}	2 [m]	4 [m]
L_{act}	1 [m]	3 [m]
P_{pol}	10	40
Low speed shaft		
α_1	70 [%]	90 [%]
H_1	10 [mm]	40 [mm]
H_2	20 [mm]	60 [mm]
Ferromagnetic parts		
α_2	35 [%]	75 [%]
H_3	30 [mm]	70 [mm]
High speed shaft		
α_3	70 [%]	90 [%]
H_4	10 [mm]	40 [mm]
H_5	20 [mm]	60 [mm]

Unlike electrical machines, where poles number (or the number of magnetic period repetition in one mechanical turn) is directly related to rotor speed and the imposed electrical frequency, magnetic gears must only respect the previously listed rules; which mean that a magnetic gear having 20 poles in the low speed shaft and 2 poles in the low one will have the same ratio compared to a one having the double amount of poles for both shafts. For this reason the variable P_{pol} is introduced, which represents the repetition of an elementary unit.

Three gear ration will be investigated for the same power input of 8[MW] at a rotational low speed shaft of 11[rpm], which needs a torque of 7[MNm]. However and as the previous optimization, required torque will be increased to 8[MNm] constituting the optimization constraint for all gear ratios detailed in Table. 4.4

Table 4.4: Poles number in elementary unit for each gear ratio

Gear ration	Low speed shaft poles	High speed shaft poles
1:5	10	2
1:10	20	2
1:20	40	2

Matlab genetic algorithm was used in order to achieve the requested goals and tuned as follow : mutation rate was set to 0.01 and crossover one to 0.8, while the optimization was performed for 100 generations with a population of 100 individuals, while non linear constraints were handled by penalty algorithm, where penalty factor was set to hundred.

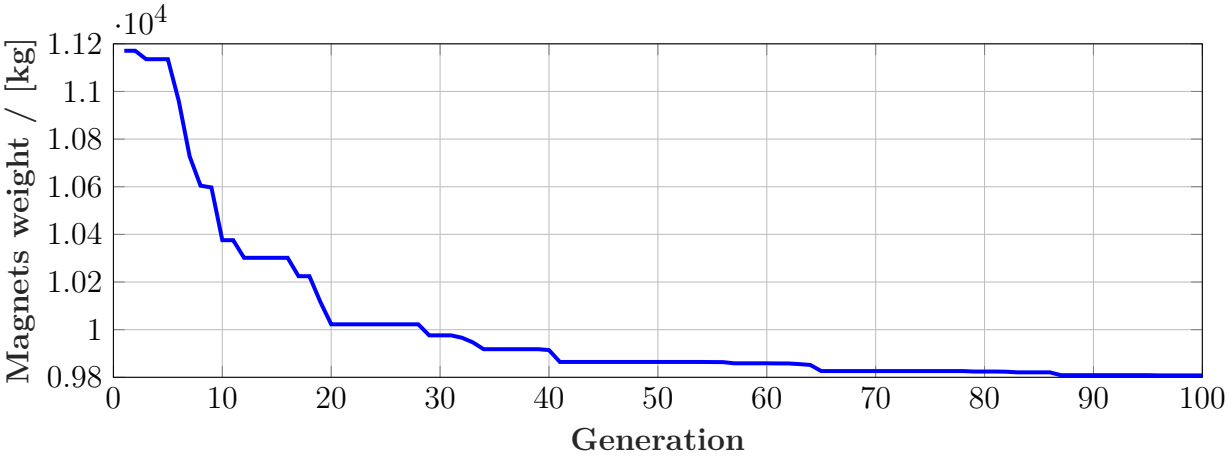

Fig. 4.7: Best individual for each generation evolution (ratio 1:5)

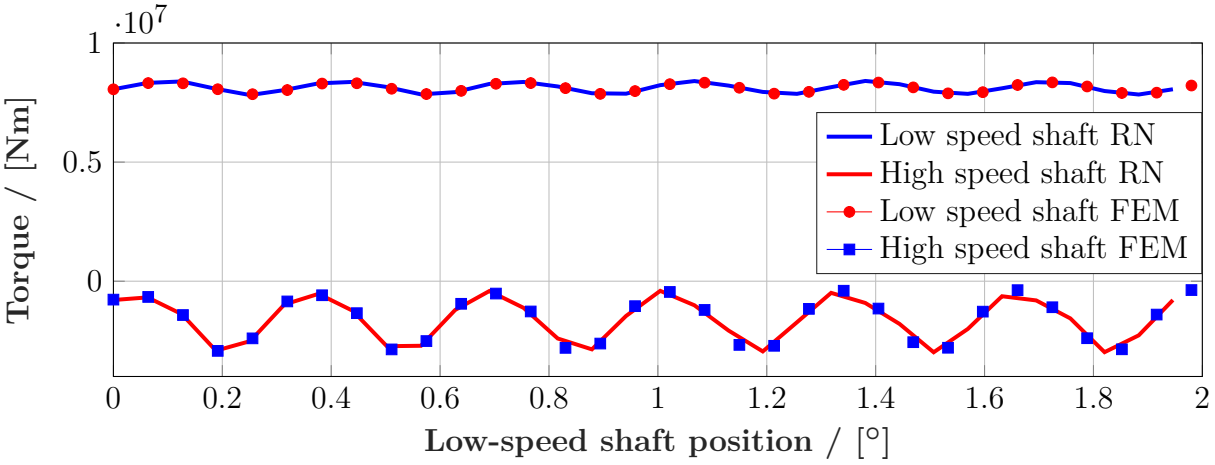

Fig. 4.8: Validation of the obtained results (ratio 1:5)

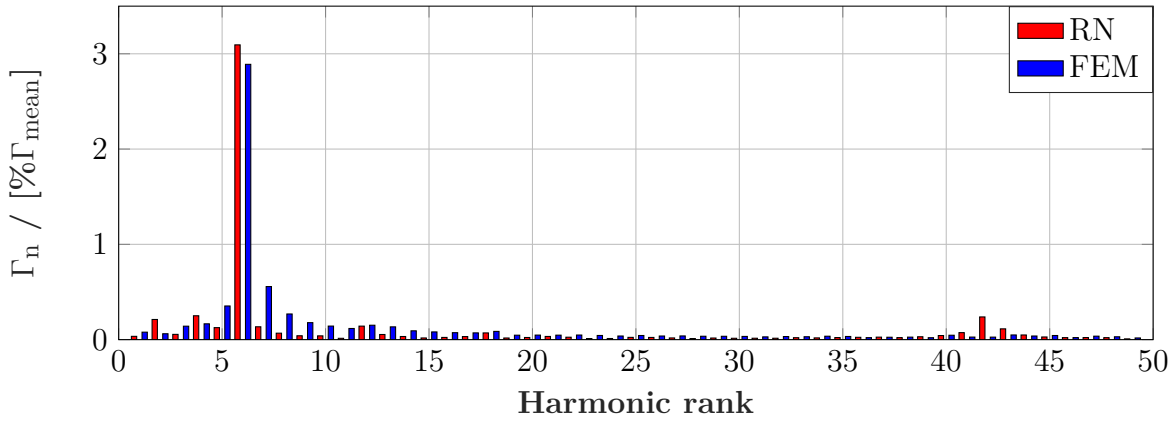

(a) Low speed shaft Torque

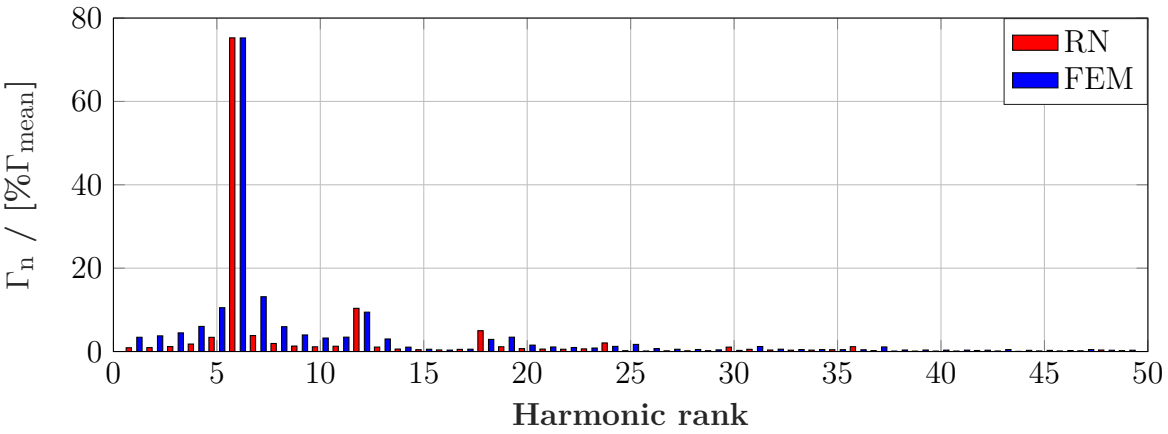

(b) High speed shaft Torque

Fig. 4.9: Fourier analyses

Table 4.5: Comparison between FEM and the developed model results (ratio 1:5)

	Γ_{mean} [MNm]	rms($\Gamma - \Gamma_{mean}$)[%Γ_{mean}]
High speed shaft RN	1.6	54.6
High speed shaft FEM	1.57	57.4
Low speed shaft RN	8.11	2.4
Low speed shaft FEM	8.11	2.12

Table 4.6: Best solution parameters (ratio 1:5)

R_{mean}[mm]		Lact[mm]	P_{pol}
3648		1763	37
H_1[mm]	H_2[mm]	H_3[mm]	H_4[mm]
17	40.5	56.2	26.8
H_5[mm]	α_1[%]	α_2[%]	α_3[%]
50	78	46	71.5

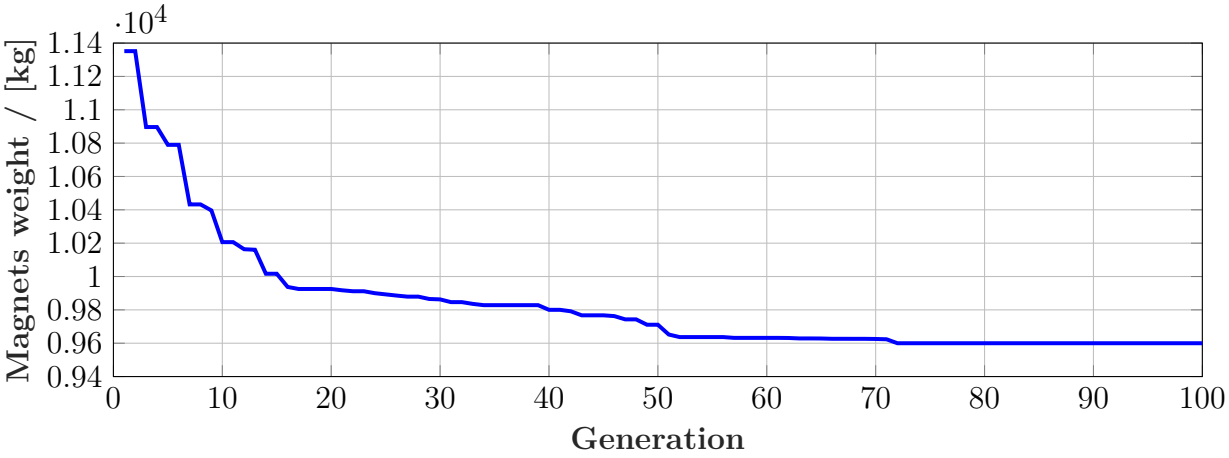

Fig. 4.10: Best individual for each generation evolution (ratio 1:10)

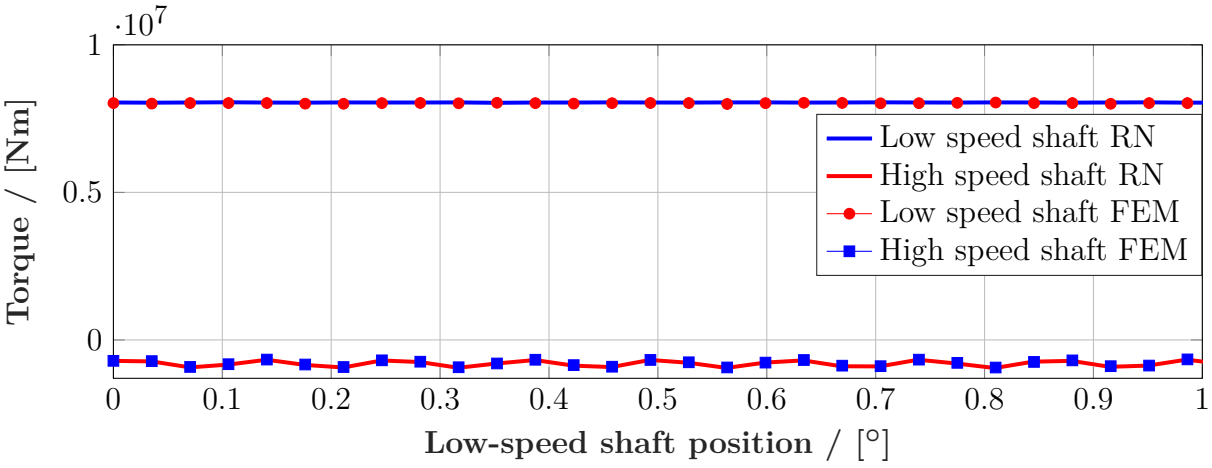

Fig. 4.11: Validation of the obtained results (ratio 1:10)

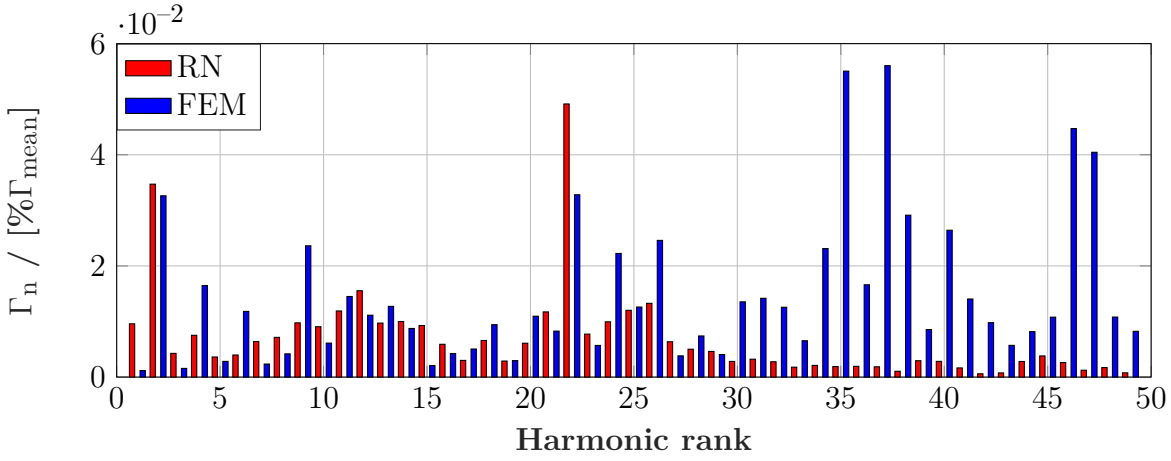

(a) Low speed shaft Torque

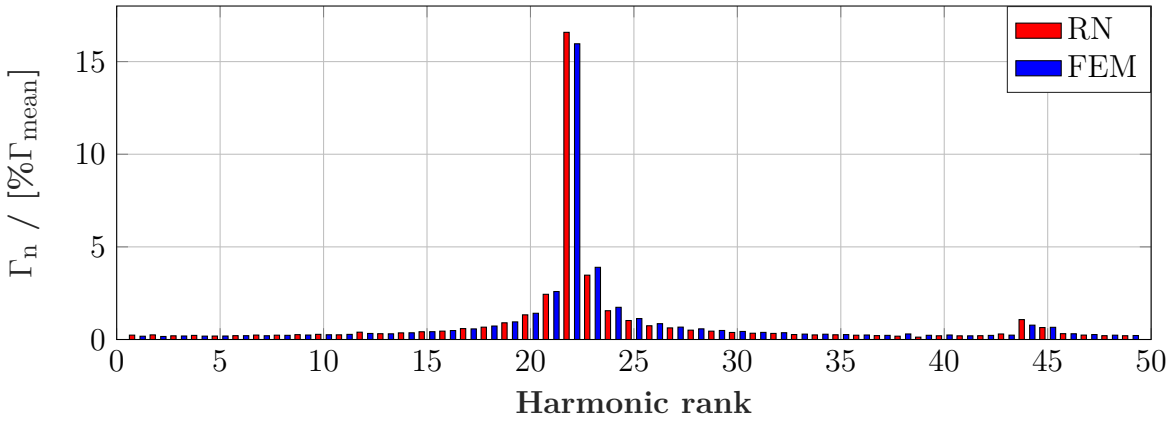

(b) High speed shaft Torque

Fig. 4.12: Fourier analyses (ratio 1:10)

Table 4.7: Comparison between FEM and the developed model results (ratio 1:10)

	Γ_{mean} [MNm]	rms($\Gamma - \Gamma_{mean}$)[%Γ_{mean}]
High speed shaft RN	0.804	12.42
High speed shaft FEM	0.794	12
Low speed shaft RN	8.04	0.08
Low speed shaft FEM	8.02	0.13

Table 4.8: Best solution parameters (ratio 1:10)

R_{mean}[mm]		Lact[mm]	P_{pol}
3723		2060	33
H_1[mm]	H_2[mm]	H_3[mm]	H_4[mm]
16.7	42.2	40.3	17.7
H_5[mm]	α_1[%]	α_2[%]	α_3[%]
46.7	79	45.6	74.1

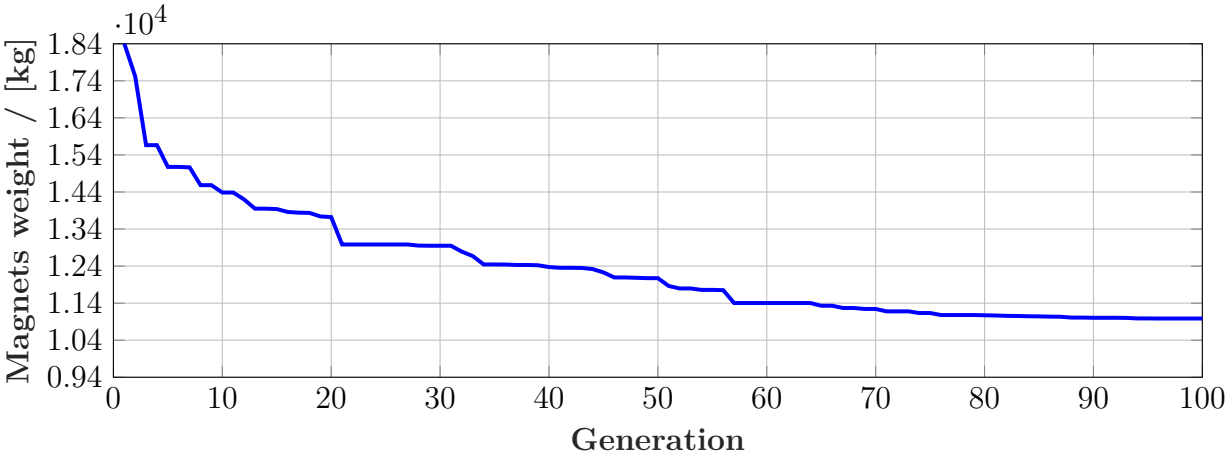

Fig. 4.13: Best individual for each generation evolution (ratio 1:20)

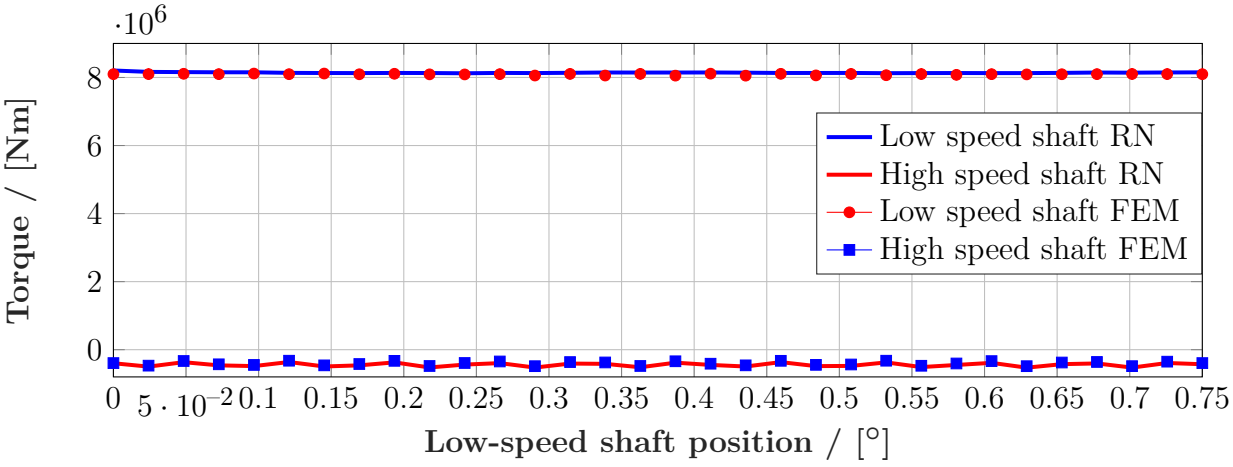

Fig. 4.14: Validation of the obtained results (ratio 1:20)

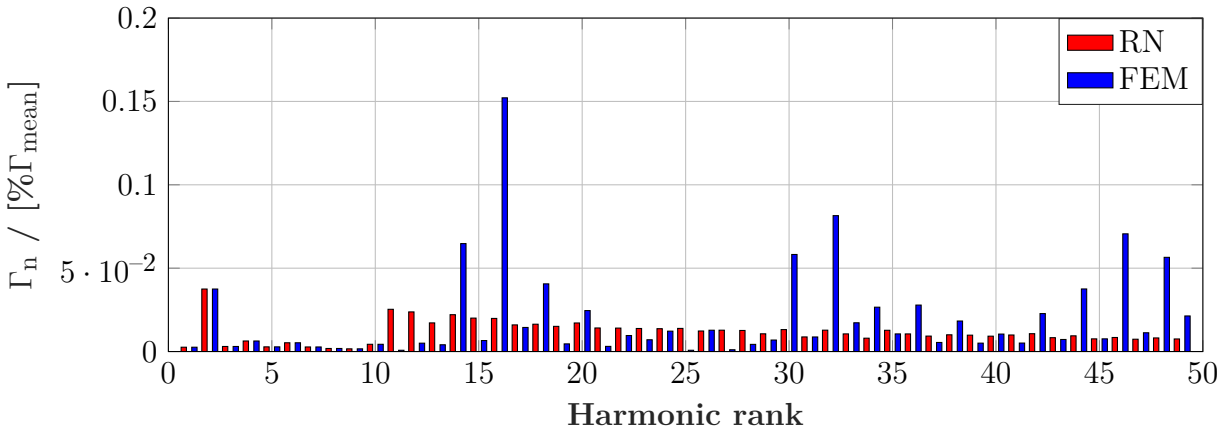

(a) Low speed shaft Torque

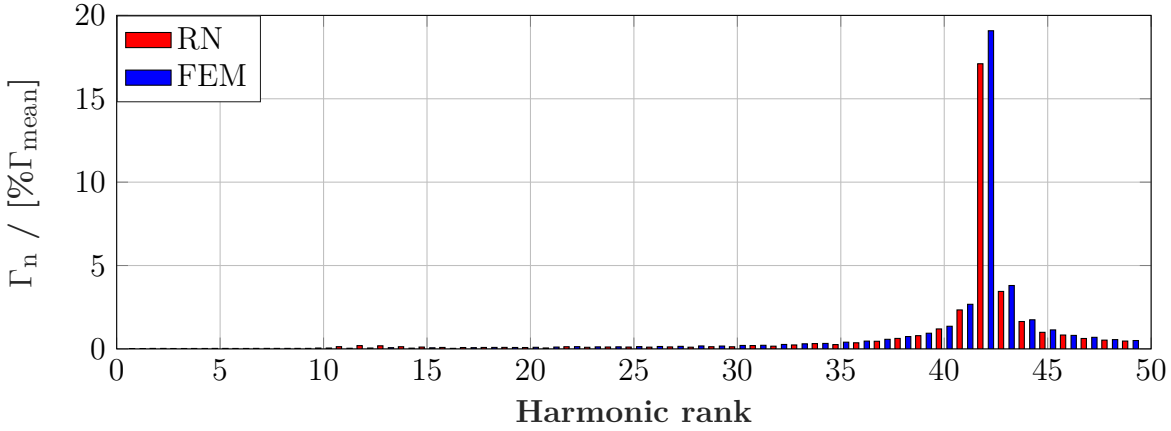

(b) High speed shaft Torque

Fig. 4.15: Fourier analyses (ratio 1:20)

Table 4.9: Comparison between FEM and the developed model results (ratio 1:20)

	Γ_{mean} [MNm]	rms($\Gamma - \Gamma_{mean}$)[%Γ_{mean}]
High speed shaft RN	0.437	12
High speed shaft FEM	0.404	13
Low speed shaft RN	8.03	0.19
Low speed shaft FEM	8.09	0.22

Table 4.10: Best solution parameters (ratio 1:20)

R_{mean}[mm]		Lact[mm]	P_{pol}
3810		2170	24
H_1[mm]	H_2[mm]	H_3[mm]	H_4[mm]
15	47.3	53.1	23.7
H_5[mm]	α_1[%]	α_2[%]	α_3[%]
58	78	43	71

From Fig. 4.7, Fig. 4.10 and Fig. 4.13, one may conclude that optimization reached a stable state where obtained results from last generation may be assumed optimal. 9.8,

9.6 and 10.9 [ton] are required respectively, in order to achieve 1:5, 1:10, 1:20 ratios respectively resulting by a mean value of 10.1 [ton] with a standard deviation of 0.7 [ton] representing 7 [%] of the mean value. This can be justified by the approximatively similar volumes for each ratio, where a mean airgap radius at low speed shaft of 3648, 3723 and 3810 [mm] are required respectively for the three ratios, leaving a mean value of 3727 [mm] and a standard deviation of 81 [mm] representing 2.2[%] of the mean value, as can be seen from Table. 4.6, Table. 4.8 and Table. 4.10. This indicates that gear ratio does not affect considerably the actuator volume, which is due to the relatively constant magnetic flux densities amplitudes as can be seen in Fig. 4.16 at the mean radius of airgap in low speed shaft , which will systematically impose a constant tangential magnetic pressure and thus demand a quasi-constant volume in order to achieve the requested low speed shaft torque.

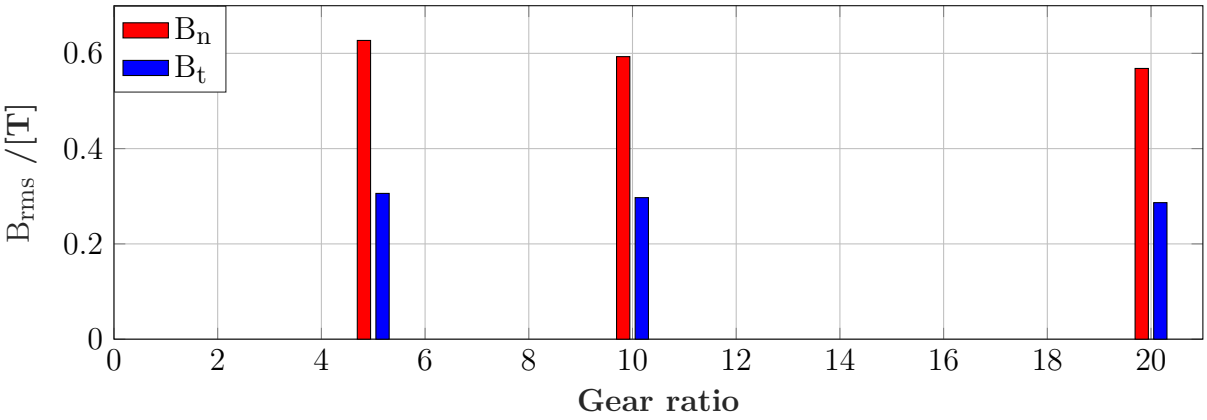

Fig. 4.16: Comparison of root mean square values of magnetic flux densities for different ratios

Table. 4.5, Table. 4.7 and Table. 4.9 strengthen the developed model accuracy, since relative error is less than 1 [%] for the low speed shaft torque and increases to maximum of 8 [%] for the high speed shaft one. One can remark that torque ripples rank is a multiple of the number of ferromagnetic pieces as can be seen in Fig. 4.9, Fig. 4.12 and Fig. 4.15, while it decreases by there increase due to the amplification of gear ratio. This explains high torque ripples (more than 50 [%] of the mean value) in the 1:5 ratio structure which is not acceptable for any kind of application, while ripples in the 1:10 and 1:20 topologies are acceptable ($\approx$ 12 [%] of mean value) and can be reduced using skewing technique.

Finally one can conclude a density of 1.26 [ton.MNm^{-1}] $\pm$ 7 [%] of magnets which is relatively enormous compared to the densities found in the previous chapter, knowing that only the magnetic gear is considered alone and this last value may increase if the machine is integrated. For these reasons a study on the required magnets weight for direct drive structures will be done next in order to identify which topology requires less noble materials per MNm.

4.3.2 Direct drive topology

As stated previously, 1.3 tons of rare magnet earth are required for each Mega Newton meter, which leads us to an interesting questions:

1. How much tons of magnets are needed for each Mega Newton meter using direct drives?.

2. Is there an optimal poles number, which increases torque density for this type of drives.

3. Seeing the densities obtained in the third chapter using class H insulation, what is its impact on magnets weight and global machine's one.

In order to investigate these questions, optimization studies will be held in order to have satisfying answer, however some assumption must be set :

1. As the previous chapter:

   (a) only Joules losses will be taken into consideration, leaving iron and eddy current losses out of study. However and as the previous chapter studies, a gap of 55 [°] is left in order to overcome the eventual temperature from the non-considered losses.

   (b) Demagnetization and hysterisis are ot taken into consideration.

   (c) The optimization will be held on a population of 100 individuals for 200 generations.

2. Airgap length is fixed to 10 [mm], assuming that this value will satisfy mechanical constraints.

3. The generator is coupled directly to the main wind turbine shaft and operates at a nominal speed of 11 [rpm], which is the same speed of the low speed shaft of the magnetic gear in order to have comparable studies. The electrical machine must develop a torque of 8 [MNm] in order to satisfy the 8 [MW] power constraints, as the previous chapter also 10 [%] of torque is added, which will help to compensate an eventual drop caused by 3D-effects.

Poles influence will be achieved through the optimization process on the structure illustrated in 4.17, since it represents an interesting torque to magnet weight ratio, where for each poles configuration, 240, 280, 320 and 400 corresponding to a voltage frequency of 22, 25 29 and 36 [Hz] respectively. Fixed parameters during the optimization process are given in Table. 4.11, while optimization parameter and their respective upper and lower boundaries are given in Table. 4.12 .

Table 4.11: Fixed parameter during poles influence optimization

Number of slots per phase and per pole	2
Rotor speed	11 [rpm]
Airgap length	10 [mm]
Cooling fluid temperature	30 [C°]
Iron conductivity	50 [$W.K^{-1}.m^{-1}$]
Aluminum conductivity	150 [$W.K^{-1}.m^{-1}$]
Magnets conductivity	9 [$W.K^{-1}.m^{-1}$]
Convection coefficient stator/cooling fluid	800 [$W.K^{-1}.m^{-2}$]
Filling factor	0.6
Iron density	7800 [$g.cm^{-3}$]
Magnet density	7600 [$g.cm^{-3}$]
Copper density	8500 [$g.cm^{-3}$]

Table 4.12: Optimizations variables and their ranges

Variable	Lower bound	Upper bound
General		
R_{mean}	1 [m]	5 [m]
L_{act}	1 [m]	4 [m]
Stator variables		
θ_{slot}	40 [%]	60 [%]
H_{slot}	100 [mm]	200 [mm]
H_{yoke}	50 [mm]	100 [mm]
J_s	2 [$A.mm^{-2}$]	5 [$A.mm^{-2}$]
Rotor variables		
α_{mag}	10 [%]	35 [%]
H_{mag}	50 [mm]	100 [mm]

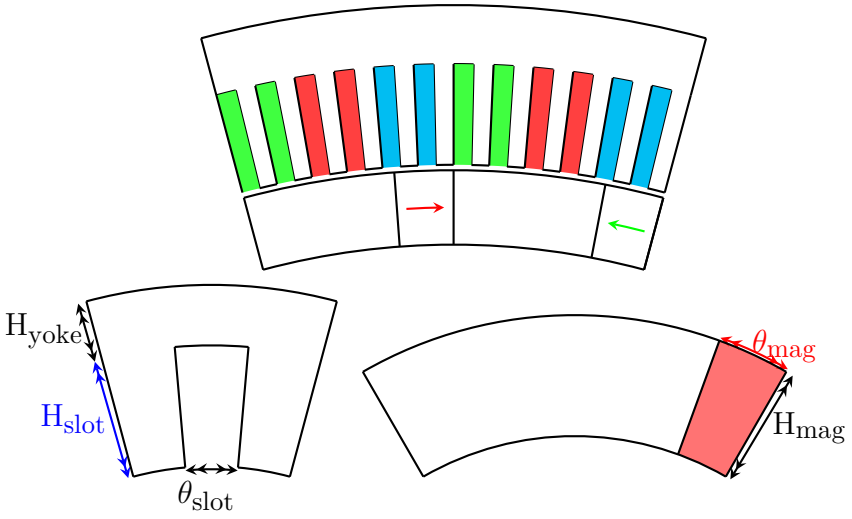

Fig. 4.17: Studied structure

The same optimization algorithm NSAG2 will be used in order to achieve the main goals, which are the reduction of total active parts mass and magnets one, while respecting constraints thermal: (temperature under 125 [°]) and torque (torque superior to 8 [MW]). These will be computed using the same model developed in chapter 2, with a consideration of the non-linear behavior of steel sheet (M400-50A) and magnet remanent field dependency on temperature. The same path of computation as the previous chapter will be taken, first temperature distribution will be estimated through Joule losses and two cases can be distinguished :

1. The machine does not respect the maximum allowed temperature in the slot and a penalty will be directly assigned to it, which will bypass torque estimation, in order to avoid unnecessary time computation.

2. The machine respects thermal constraints, thus magnet maximum temperature will be taken into account to correct remanent flux density and used after by magnetic model to compute the electromagnetic torque. In order to save more time, only static torque will be computed; which means that the electromagnetic field from the stator is static and rotor one is rotating through its movement. This means that for each phasing between stator and rotor fields torque will be computed for only one position; allowing to reduce computation steps and finding maximum torque delivered by the generator. It is clear that this method is efficient only with generators having a relative reduced torque ripples, otherwise the estimated electromagnetic torque by the last described method will be either over or underestimated compared to the mean one.

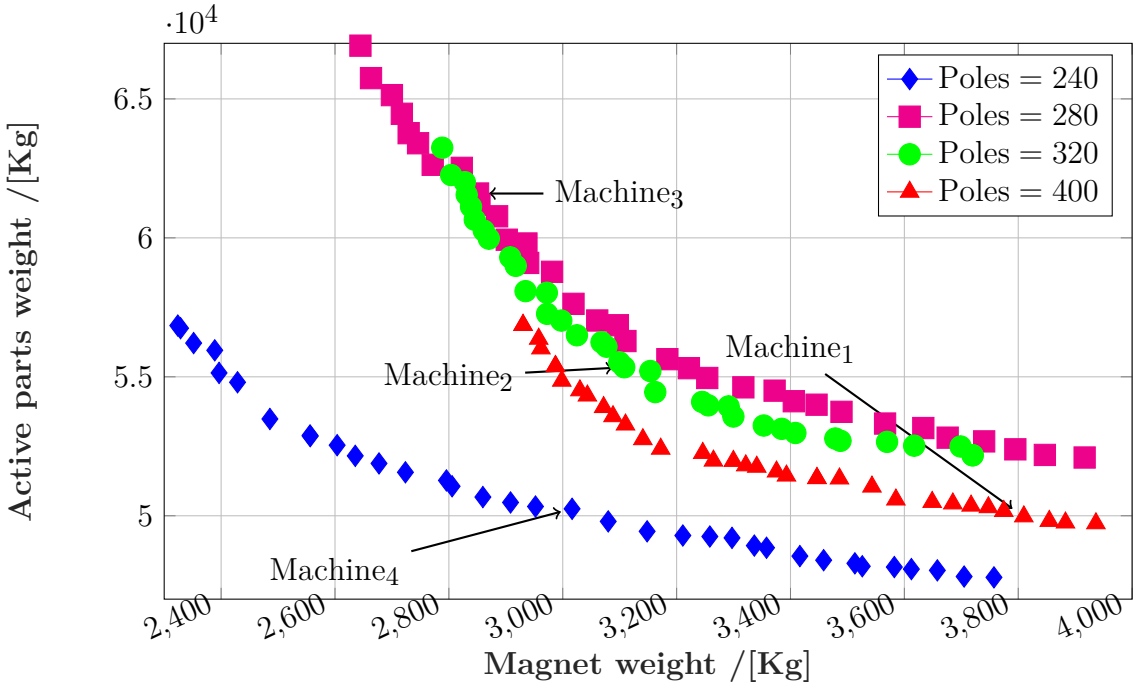

Fig. 4.18: Pareto optimality for different poles number

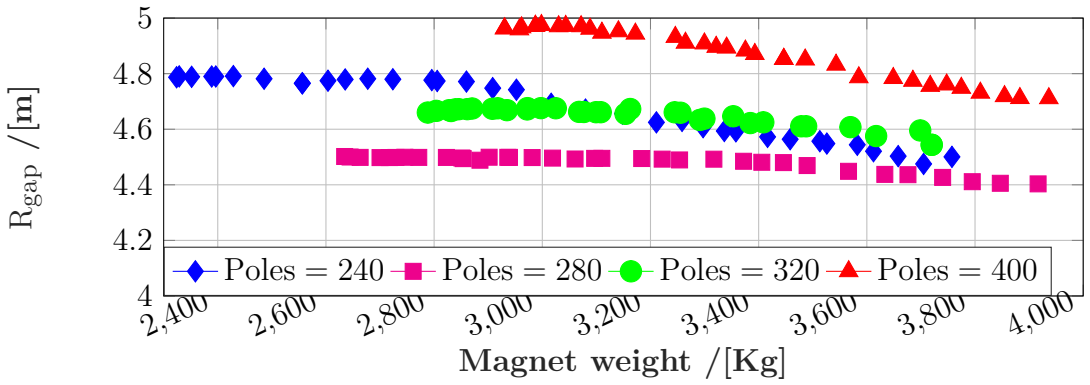

(a) Mean airgap radius

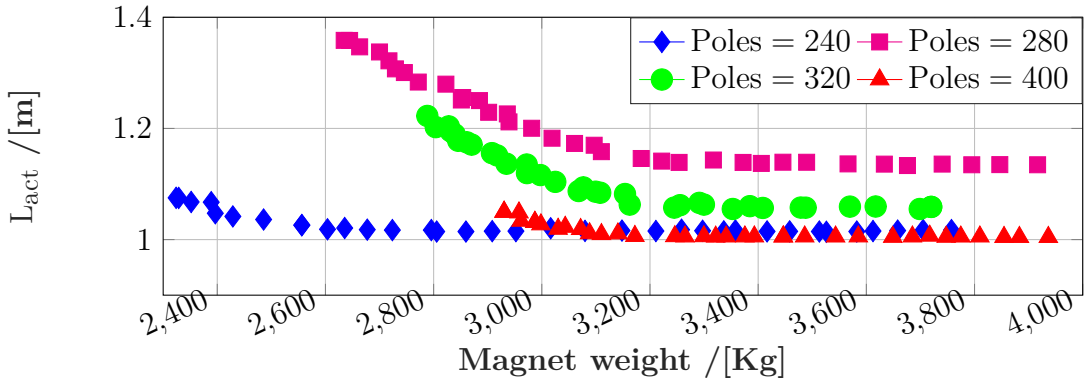

(b) Active length

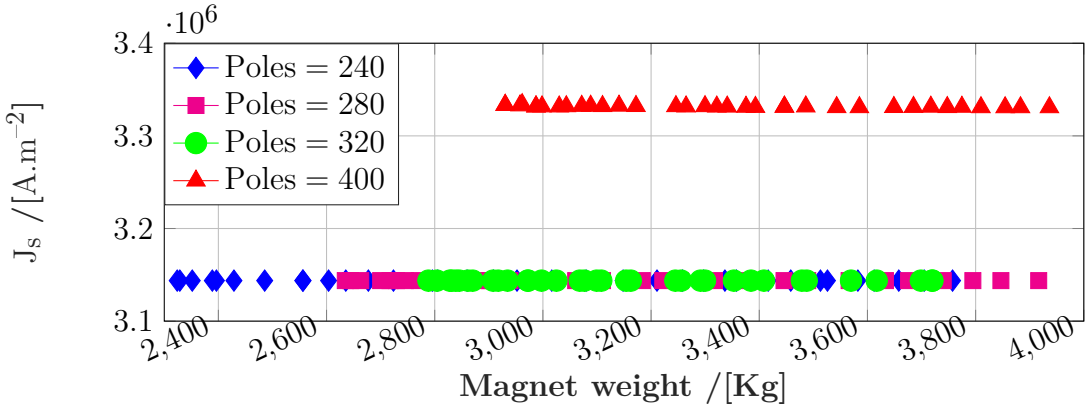

(c) Current density

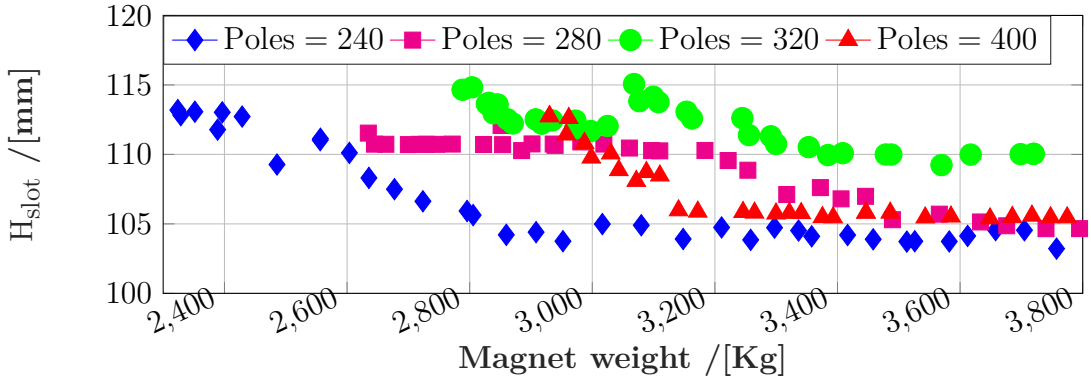

(d) Slot depth

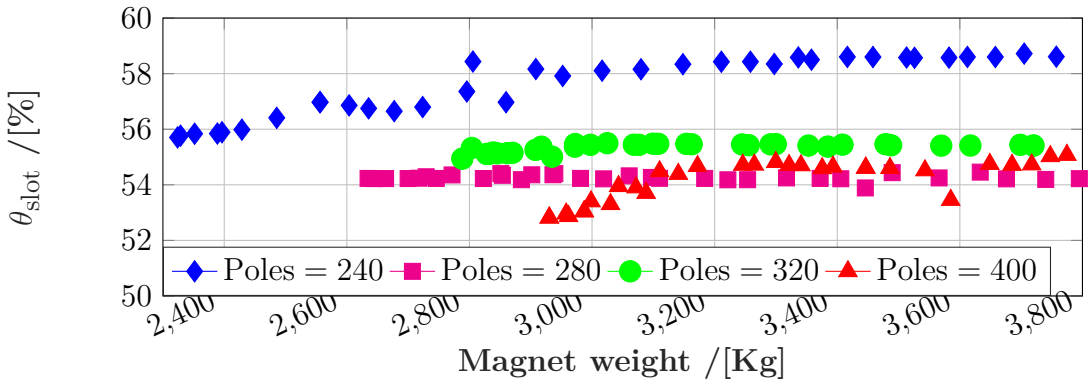

(e) Slot angular opening

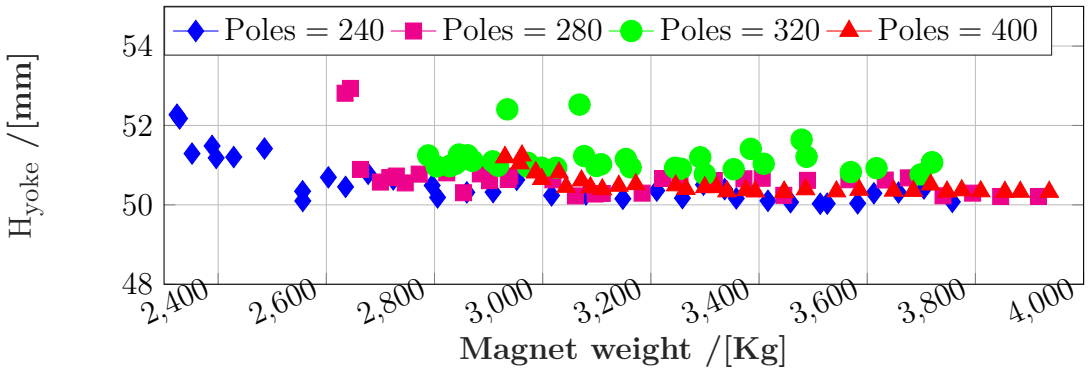

(f) Yoke thickness

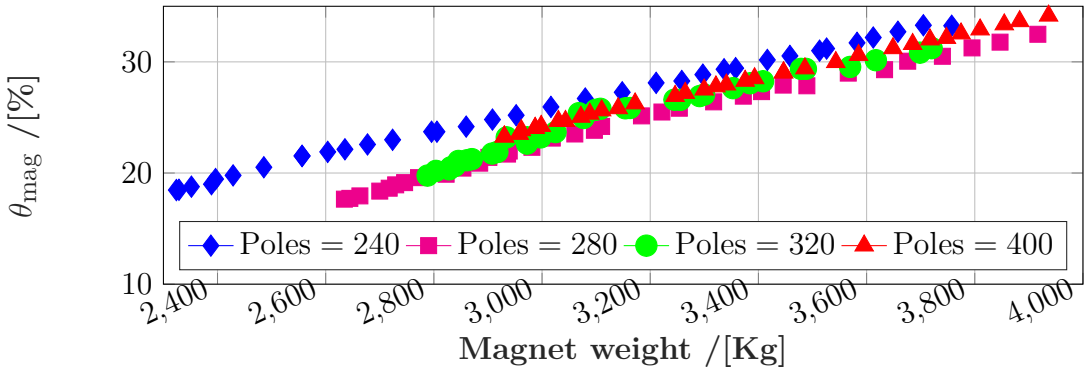

(g) Magnet angular opening

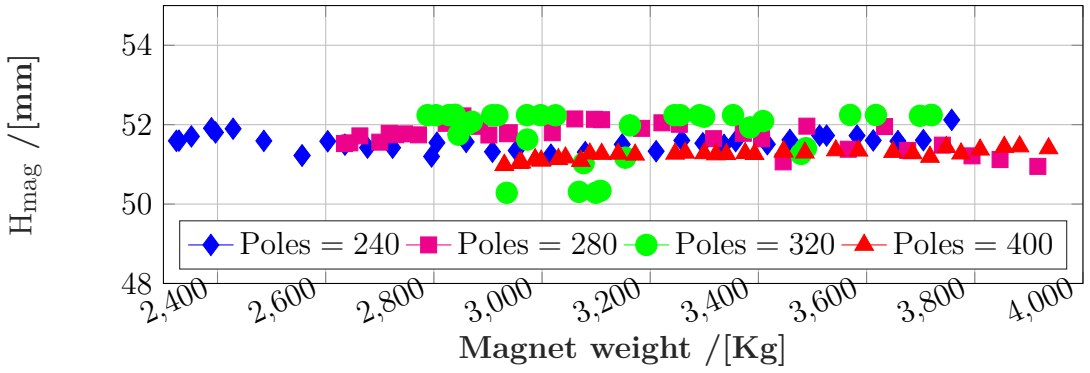

(h) Magnet thickness

Fig. 4.19: Poles number influence on optimization results

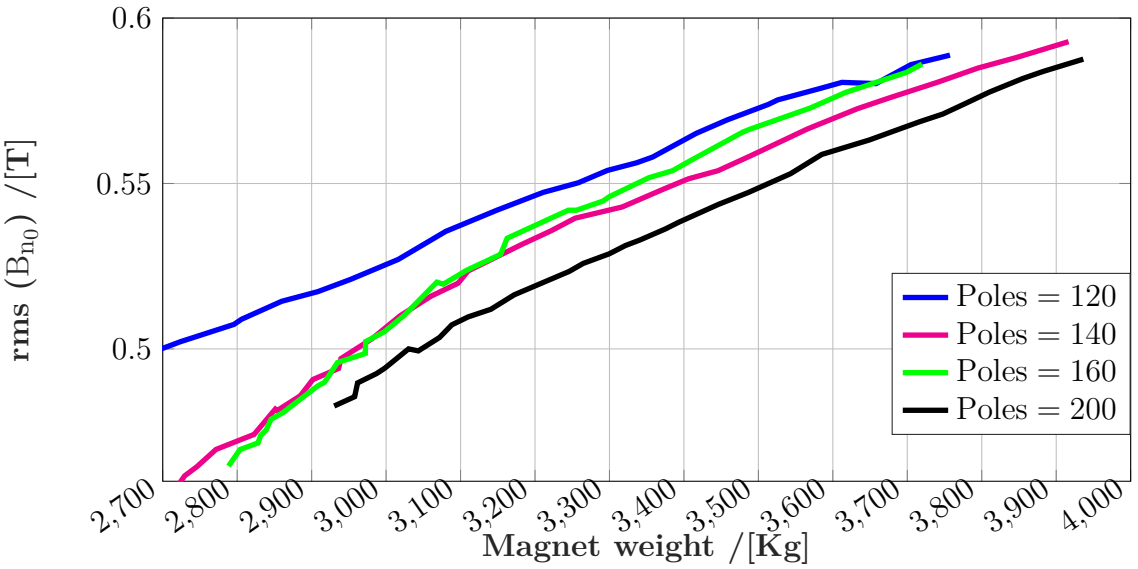

Fig. 4.20: No-load root mean square value of normal magnetic field density

Fig. 4.18 presents Pareto optimality with the considered objectives for different poles combination, what can be first noticed is that 240 poles structure request less active materials compared to rest. Second an increase of poles will be accompanied with an increase of active materials weight, this can be explained as follow: due to the amplification of poles and the constant number of slot per pole and per phase, the tooth saturation will be amplified and heat flux may find difficulties to evacuate from the slot, which will lead to an increase of the radius or active length in order to overcome the torque drop accompanied with it and improve heat dissipation. this can be noticed in Fig. 4.19, where either mean airgap radius or active length must be increased in order to overcome the listed phenomena. One must not forget that these disadvantageous aspect are accompanied with advantageous one, since increasing poles number will favorite flux concentration. One can note also that for the 400 poles configuration, the current density is increased, this can be explained by the increase of mean airgap radius with the relatively constant slot depth value, which favors heat dissipation and thus allows more current density.
Slot depth is barely the same for all the studied cases, since one of the main objective (reduction of active materials mass) is highly affected copper volume, which represents the heavier materials, and thus slots depth. In addition 50 [mm] of yoke seems sufficient for all studied pole combination, which is comprehensive since increasing poles number will lead to a slight reduction in yoke thickness.
Magnet weight depends highly on four main parameters, mean airgap, active length, magnet opening factor and their thickness. In a simplified matter, lets assume that mean airgap and active length values are constant, which will leave only two variable: optimization algorithm has three paths to modify magnet weight either by their opening factor, depth or both. However increasing depth will highly increase their mass since the studied machine is a radial flux one, and also will increase rotor iron mass and thus global machine weight, which is critical for both objectives. For these reasons the linear progression and constant value, which is equal to the lower bound, is observed in 4.19.
Fig. 4.20 justify the light weight of the 240 poles machines, since for approximatively the same weight of magnets a high normal magnetic flux densities is achieved at no-load.

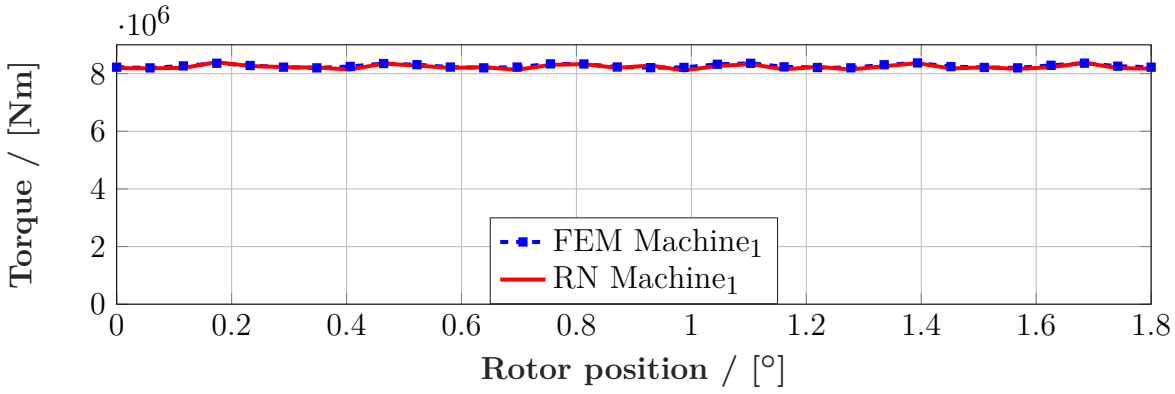

(a) Poles = 400

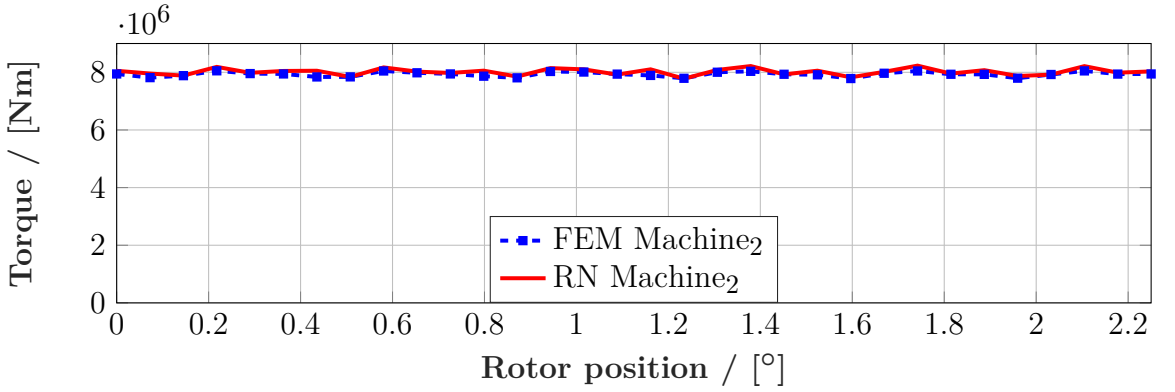

(b) Poles = 320

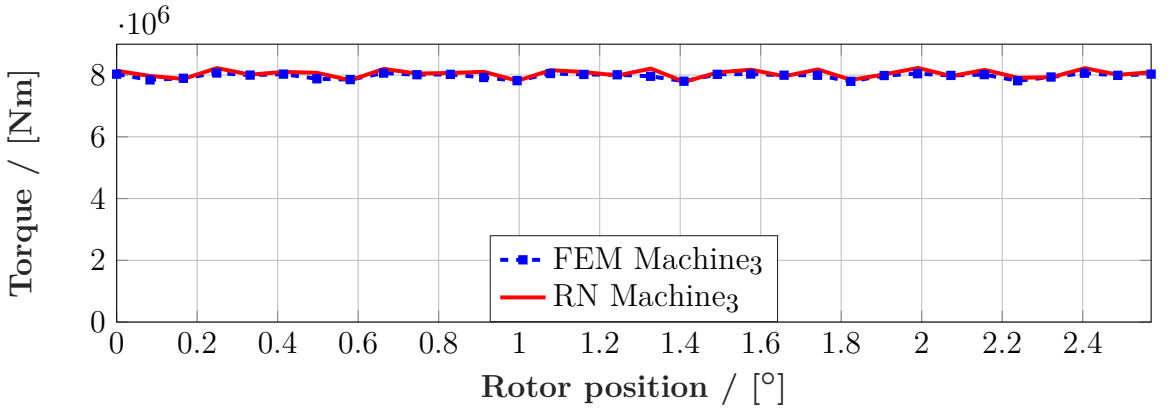

(c) Poles = 280

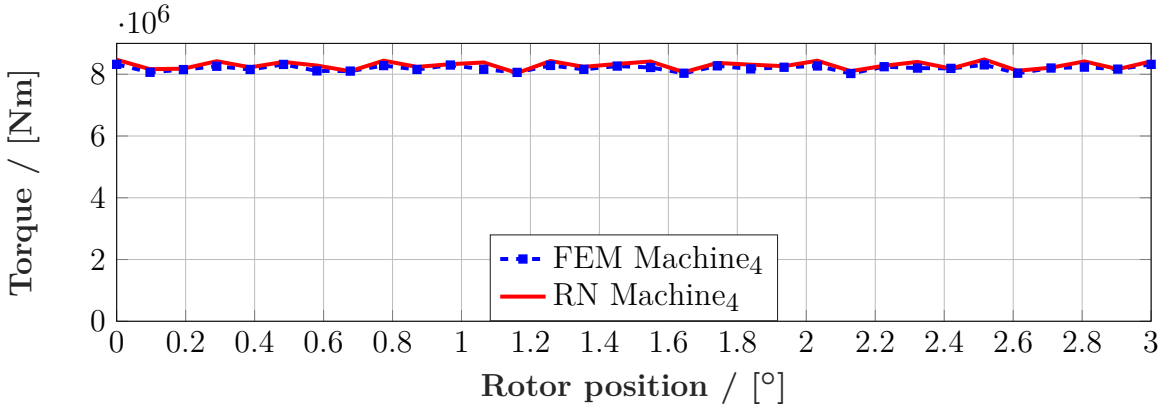

(d) Poles = 240

Fig. 4.21: Validation of the obtained results

Table 4.13: Comparison between FEM and the developed model results

	Γ_{mean} [MNm]	rms($\Gamma - \Gamma_{mean}$)[%Γ_{mean}]
$Machine_1$ RN	8.23	0.9
$Machine_1$ FEM	8.26	0.7
$Machine_2$ RN	8.01	1.5
$Machine_2$ FEM	7.93	1
$Machine_3$ RN	8.04	1.6
$Machine_3$ FEM	7.96	1.04
$Machine_4$ RN	8.29	1.5
$Machine_4$ FEM	8.19	1.08

Fig. 4.21 and Table. 4.13 validates the model results and strengthen optimization results accuracy, where torque ripples are under 1.5 [%] of the mean torque, which can be acceptable for wind turbine generators. In a mean matter 470 [kg] of magnets are required for each Mega-Newton-meter and 6.8 tons of active materials per [MNm], for the considered cooling and insulation class. Furthermore, these last values will be updated for class b insulation in order to estimate the increase of total mass under the same magnetic constraints using the same objectives.

To achieve a correct mass estimation when class B insulation is used and have a sharp look at its influence, optimization studies will be achieved under the same previous condition. Only thermal constraint will be changed allowing a maximum temperature of 75 [°C] leaving the same gap of 55 [°C] in order to avoid a probably rise caused from the neglected losses such as iron and eddy current ones or due to a variation of thermal coefficient such as slot's equivalent conductivity or/and convection coefficient.

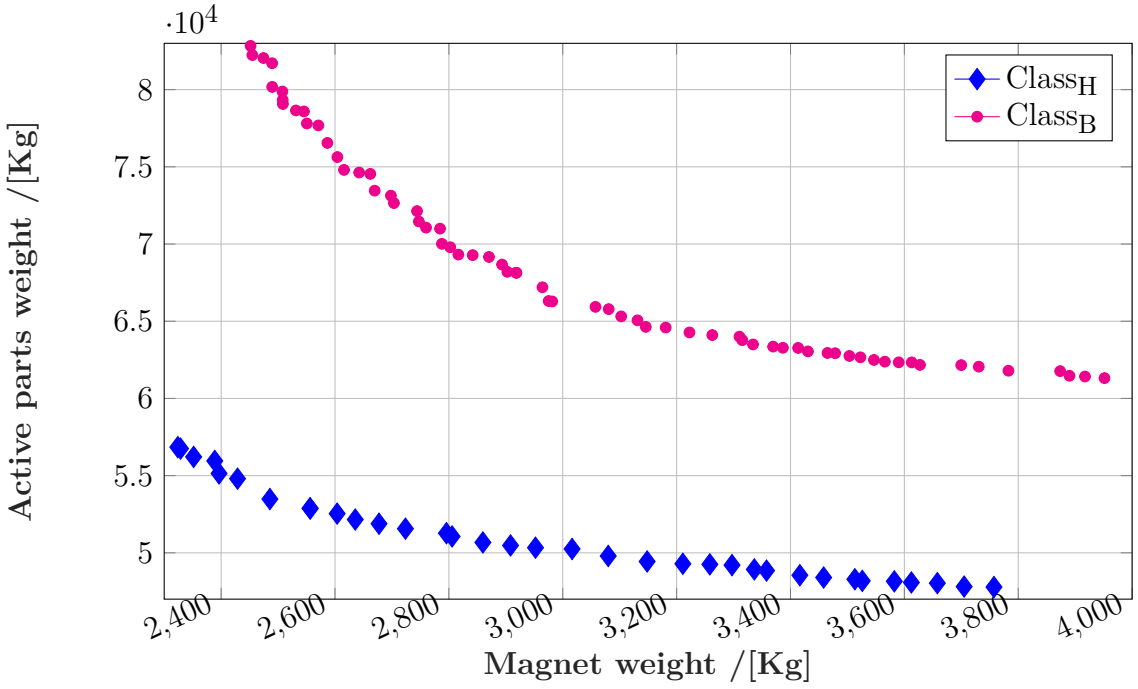

Fig. 4.22: Class insulation influence on Pareto optimality

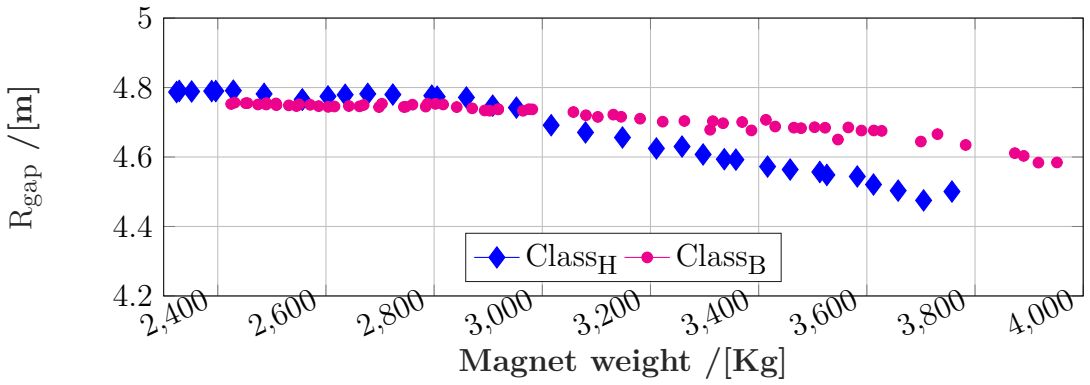

(a) Mean airgap radius

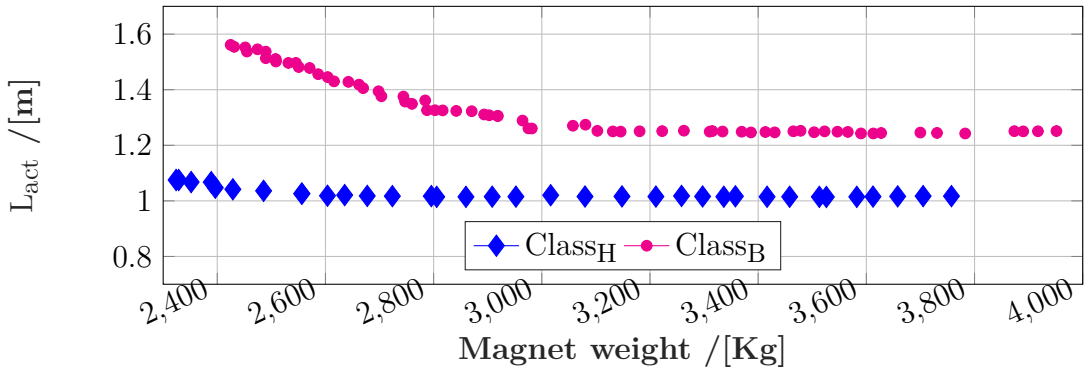

(b) Active length

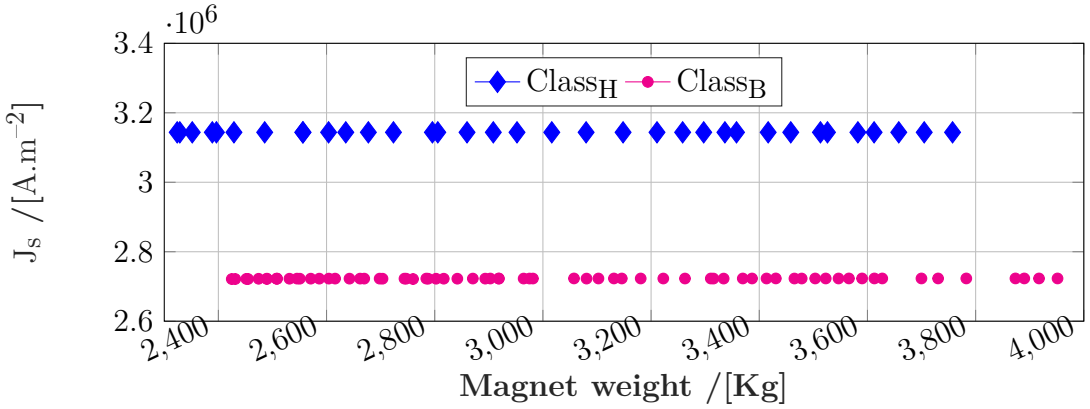

(c) Current density

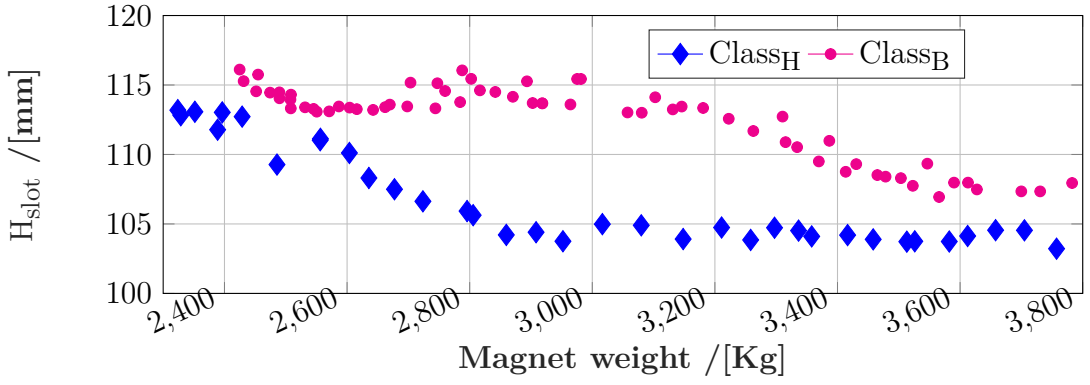

(d) Slot depth

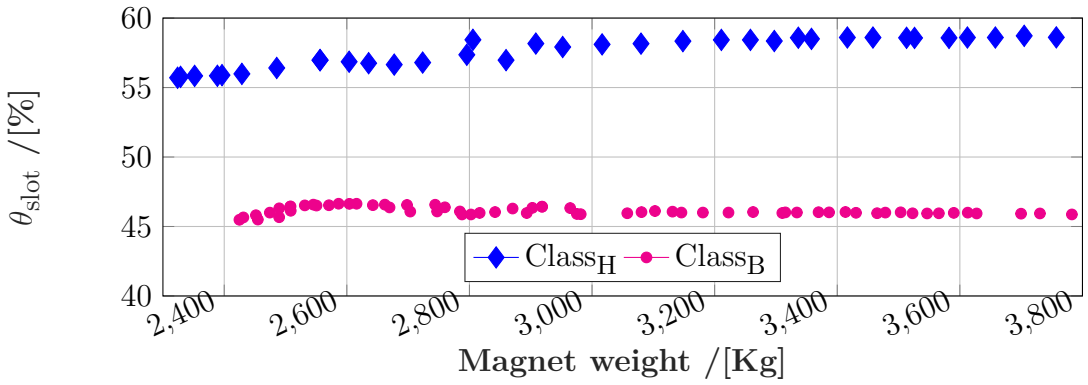

(e) Slot angular opening

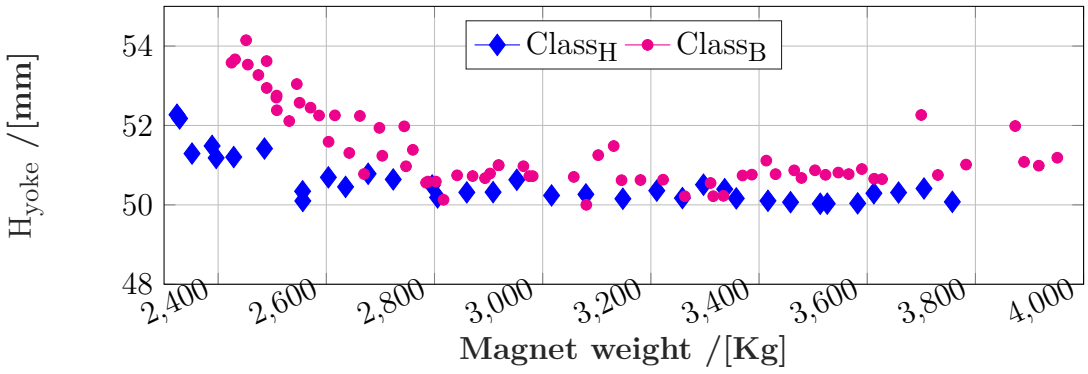

(f) Yoke thickness

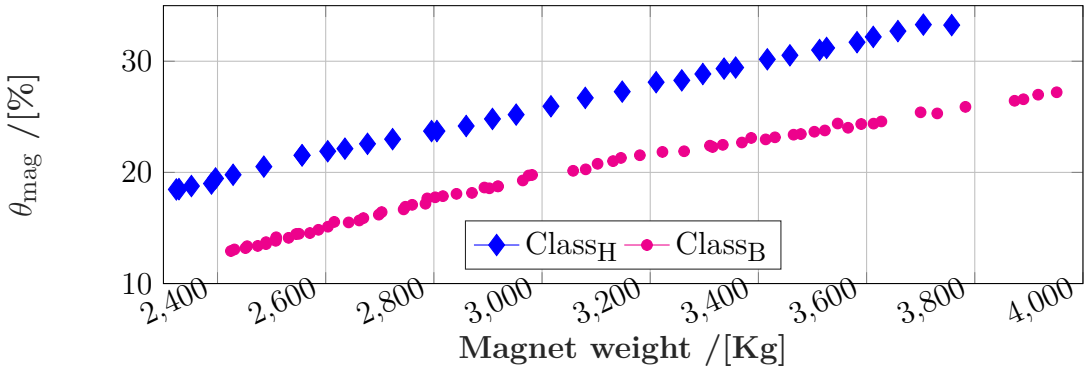

(g) Magnet angular opening

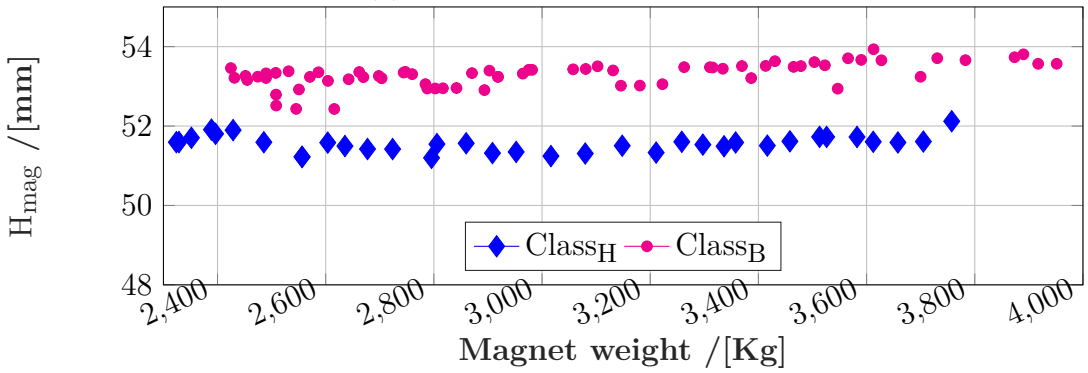

(h) Magnet thickness

Fig. 4.23: Insulation class influence on optimization results

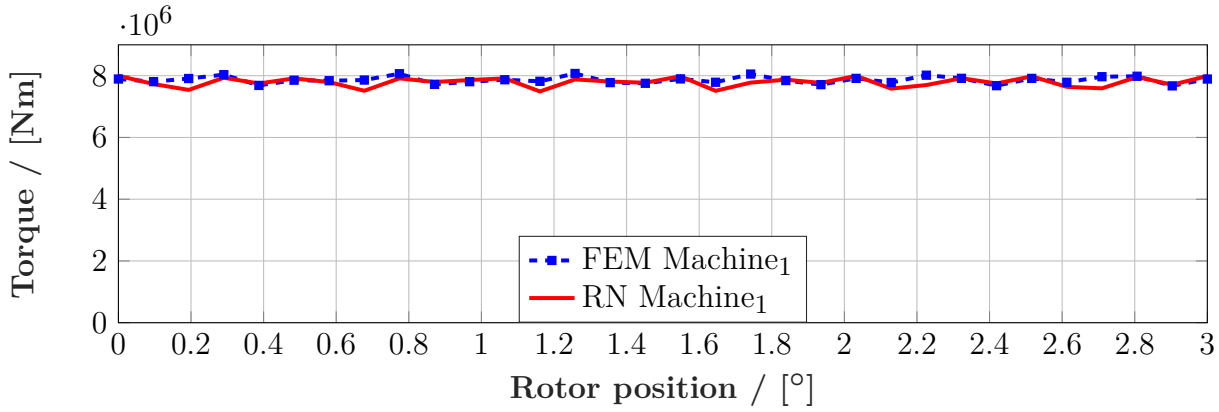

Fig. 4.24: Validation of the obtained results

Table 4.14: Comparison between FEM and the developed model results

	Γ_{mean} [MNm]	rms($\Gamma - \Gamma_{mean}$)[%Γ_{mean}]
Machine$_1$ RN	7.79	1.98
Machine$_1$ FEM	7.86	1.42

As expected, it can be seen in Fig. 4.23 an increase of active length between 20 [%] and 50 [%] when class B insulation is used compared to class H insulation.

While current density drops by 15 [%] for a quasi constant slot height. However, its angular opening was slightly reduced from 52[%] to 45[%], which increases tooth angular aperture and may help heat dissipation. Magnets height is approximatively the same, since their weight is highly impacted by it, while their angular opening has the same linear law as the class H insulation one.

For all these reason, Pareto front shape is modified as it is noticed in Fig. 4.22, while Table. 4.14 justifies once more model's accuracy and strengthen its capability of finding a correct Pareto front.

Conclusion

This chapter attempted to answer its main title formulated as a question : is it better to use magnetic gear instead of mechanical one? how much rare earth permanent magnet weight is needed to achieve the goal, or should one adapt direct drive topology which may demand less permanent magnet compared to the previous proposed solutions?

First, magnetic gear was defined with a close look to its main governing analytical equations for a proper operating point, which define poles number for both rotors and the number of ferromagnetic pieces. In parallel a brief look was given to mechanical gears, especially ones used in wind energy, with commune failures which are related to mechanical stress and fatigue applied on the structure. These last failures can be avoided using contactless gear, which is offered by the magnetic one.In order to properly estimate the amount of permanent magnets needed for this solution, an optimal design was done using the developed model, where each main parts (two rotors and the ferromagnetic pieces) were modeled using reluctances networks and linked via interpolation function, allowing the consideration of both rotor movement. Reducing permanent magnet mass and insuring the requested torque at low speed rotor constituted objective and constraint respectively. The gear ratio has a slight effect on torque density, since in the performed investigation on three different values 1:5, 1:10, and 1:20 torque density varied only by 7 [%] around a mean value of 1.26 tons of permanent magnet per [MNm], which is close to class H surface mounted permanent magnet machine one. However gear ratio impacts highly torques ripples for the considered structure, especially on high speed shaft, which may be reduced either by skewing or by modifying magnet and/or ferromagnetic pieces shape.

Second, an optimal design was performed on concentrated flux machines, since they offer good torque density, with a close look on poles and insulation class influence of optimization results and on Pareto front shape. through mutiple optimization, we can conclude that for class H insulation torque densities are in the intervals [300 – 500] [kg] of permanent magnets and [6.25 – 8.5] [tons] of active materials per [MNm] for class H insulation depending on poles number. For class B insulation, the intervals will be updated to [320 – 500] [kg] of permanent magnets and [7.75 – 10.5] [tons] of active materials per [MNm].

Through these results the answer to this chapter question is: concentrated flux structure may be a good candidate for wind energy chain conversion, even though surface mounted machine were not investigated since it is considered as a ”safe” solution. If the question was formulated from a technical and economic point it will be: should we ”gamble” on magnetic gear or on direct drive concentrated flux machine, the scientific answer would be : may be concentrated flux machine is a safer solution.

Finally, these results are only the visible part of the iceberg, since adding more constraints such as iron losses, eddy current losses, integration of converter, investment to develop and construct the new chosen technologies will change Pareto front. However the obtained dominant machines can serve as a good input parameters for more refined technical and/or economical studies, since a gap of 55 [°C] was left sided by an addition of 10[%] of requested torque value.

General Conclusion

Wind energy still has some improvement to do and some challenges to overcome in term of technology development. Indeed, in order to compete with its rough rival such as fossil and nuclear energy, where technology reached a mature state and mastered in order to achieve the cheapest cost of energy. In addition, natural resources can not be controlled such as lack of wind or its excesses.

For these reason and in order to propose an affordable clean energy, wind turbine manufacturer optimizing the conversion chain. Where this takes part by investigating the integration of concentrated flux permanent machine and/or magnetic gears in wind energy conversion chain. In order to achieve this goal , a fast accurate multi-physics model was developed and based on lumped models and interpolation function, which helps to overcome most of numerical problems proposed by conventional methods and does not mislead an optimization algorithm in its search pattern. Optimization algorithm must be chosen carefully, through the knowledge of the treated problem; mono or multi-objective, constrained or not, presence of analytical objective function and its derivatives...

The developed model showed good performance in time computation and accuracy by comparing its results with measurements and commercial software data. The optimization helped us to estimate the amount of rare earth permanent magnet weight for each requested mega-Newton-meter of torque.

As expected, concentrated flux permanent magnet generator requests less magnets than surface mounted one for the same requested torque as resulted in third chapter optimizations. While magnetic gear does not seem an affordable solution for wind energy conversion chain, since it request a considerable amount of rare earth permanent magnet, as seen in chapter four results.

One must not forget that the perfect objective is energy cost minimization, through logistics, transport, material and maintenance cost reduction. Which means that obtained results are not final from the economical point of view, which open new research opportunity on generator conception without rare earth permanent magnet, which will be the continuity of this PhD in [150] with a strong coupling between the magneto-thermal developed model and a vibro-acoustic one elaborated in [6], from which a small scal prototype construction will be helpful in order to wisely tune all the developed multi-physics models.

Appendix A

Scientific papers

1. H.ENNASSIRI, **M.A.BENHAMIDA**, M.DHIFLI, G.BARAKAT : *Vibro acoustic response of a discodal switching flux permanent magnet machine due to electromagnetic origin*, Elsevier journal, submitted november 2017.

2. H.ENNASSIRI, **M.A.BENHAMIDA**, M.DHIFLI, G.BARAKAT : *Slots & Poles combination influence on the vibro acoustic behavior of axial type flux switching permanent magnet machines*, Elsevier journal, submitted november 2017.

3. **M.A.BENHAMIDA**, H.ENNASSIRI, G.BARAKAT :*Reluctance Network Lumped Mechanical & Thermal Models for the modeling and predesign of concentrated Flux synchronous machine*, Open Physics journal, submitted november 2017.

4. **M.A.BENHAMIDA**, H.ENNASSIRI, M.DHIFLI, G.BARAKAT, Y.AMARA: *Slots & Poles combination influence on the vibro-acoustic behavior of axial type flux switching permanent magnet machines*, Electrimacs 2017, Toulouse, July, 2017.

5. H.ENNASSIRI, **M.A.BENHAMIDA**, M.DHIFLI, G.BARAKAT, Y.AMARA: *Vibro acoustic response of a discoidal switching flux permanent magnet machine due to electromagnetic origin*, Electrimacs 2017, Toulouse, July, 2017.

6. **M.A.BENHAMIDA**, H.ENNASSIRI, G.BARAKAT: *Reluctance Network Based Optimization of Large Concentrated Flux Permanent Magnet Wind Generator*, International Symposium on Applied Electromagnetics and Mechanics (ISEM) 2017 Chamonix Mont Blanc, September, 2017.

7. H.ENNASSIRI, **M.A.BENHAMIDA**, G.BARAKAT, Y.AMARA: *Influence of contact coefficients on vibrational behavior of PM machines using a new investigation approach*, ISEF 2017, Lodz, Poland, September, 2017.

8. **M.A.BENHAMIDA**, H.ENNASSIRI, G.BARAKAT, Y.AMARA: *Reluctance Network Lumped Mechanical & Thermal Models for the modeling of concentrated Flux synchronous machine*, ISEF 2017, Lodz, Poland, September, 2017.

9. H.ENNASSIRI, **M.A.BENHAMIDA**, Y.AMARA, G.BARAKAT : *Comparison between Axial type Surface Mounted & Switching Flux Permanent Magnet machines for wind turbine application*, Cistem 2016, Marrakech.

10. N.DEBBAH, **M.A.BENHAMIDA**, H.ENNASSIRI, Y.AMARA, G.BARAKAT :*Modélisation d'une Machine Synchrone à Double Excitation Série par un Circuit de Réluctances Maillé*, Cistem 2016, Marrakech.

11. **M.A.BENHAMIDA**, H.ENNASSIRI, Y.AMARA, G.BARAKAT :*Interpolation coupling for reluctance network models dedicated to the predesign of Switching Flux Permanent Magnet machines*,Cistem 2016, Marrakech.

12. S.OUAGUED, **M.A.BENHAMIDA**, Y.AMARA, G.BARAKAT : *Thermal modeling of tubular linear machines using a hybrid analytical method*, SMART 2015, Kuwait.

13. M.DHIFLI, **M.A.BENHAMIDA**, H.ENNASSIRI, F.CHABOUR, Y.AMARA, G.BARAKAT: *Modeling of axial flux switching permanent magnet machine using magnetic equivalent circuit*, International Symposium on Electromagnetic Fields (ISEF), Valencia, Spain, September, 2015.

Bibliography

[1] H. Tiegna, "Contribution à la modélisation analytique des machines synchrones à flux axial à aimants permanents à attaque directe en vue de leur dimensionnement. application aux éoliennes," Ph.D. dissertation, Thèse de doctorat de l'Université du Havre, 2013.

[2] A. Bellara, "Modélisation analytique par le formalisme de maxwell des machines synchrones à aimants permanents à flux axial en vue de leur dimensionnement," Ph.D. dissertation, Le Havre, 2011.

[3] M. DHIFLI, "Contribution au développement de structures discoïdes de machines électriques à aimants permanents à commutation de flux pour l'éolien," *Le Havre university*, 2016.

[4] N. Abdel-Karim, "Dimensionnement et optimisation d'un aérogénérateur à aimants permanents à flux axial de petite puissance," *Le Havre university*, 2008.

[5] J. Azzouzi, "Contribution à la modélisation et à l'optimisation des machines synchrones à aimants permanents à flux axial. application au cas de l'aérogénérateur," *Le Havre university*, 2007.

[6] H. Ennassiri, "Etude et diagnostic de défauts dans les machines synchrones à commutation de flux dédiées au véhicule électrique hybride," Ph.D. dissertation, Le Havre, 2018.

[7] W. Tong, *Wind power generation and wind turbine design*. WIT press, 2010.

[8] Z. Zhang, A. Matveev, S. Øvrebø, R. Nilssen, and A. Nysveen, "State of the art in generator technology for offshore wind energy conversion systems," in *2011 IEEE International Electric Machines Drives Conference (IEMDC)*, May 2011, pp. 1131–1136.

[9] REN21, "Renewables 2017 global status report."

[10] 2016 global energy trends: Is energy transition on the right path? [Online]. Available: https://www.enerdata.net/publications/reports-presentations/global-energy-trends-2017.html

[11] N. Goudarzi and W. D. Zhu, "A review on the development of wind turbine generators across the world," *International Journal of Dynamics and Control*, vol. 1, no. 2, pp. 192–202, Jun 2013. [Online]. Available: https://doi.org/10.1007/s40435-013-0016-y

[12] Your source for renewable energy information. [Online]. Available: http://resourceirena.irena.org/gateway/

[13] Global wind report 2016. [Online]. Available: http://gwec.net/publications/global-wind-report-2/

[14] 2016 european statistics. [Online]. Available: https://windeurope.org/wp-content/uploads/files/about-wind/statistics/WindEurope-Annual-Statistics-2016.pdf

[15] 2016 wind technologies market report. [Online]. Available: https://emp.lbl.gov/sites/default/files/2016_wind_technologies_market_report_final_optimized.pdf

[16] H. Link, W. LaCava, J. van Dam, B. McNiff, S. Sheng, R. Wallen, M. McDade, S. Lambert, S. Butterfield, and F. Oyague, "Gearbox reliability collaborative project report: findings from phase 1 and phase 2 testing," National Renewable Energy Laboratory (NREL), Golden, CO., Tech. Rep., 2011.

[17] Fast v8 offers new modeling and analysis features. [Online]. Available: https://energy.gov/eere/wind/articles/fast-v8-offers-new-modeling-and-analysis-features

[18] Latest news middle east and africa. [Online]. Available: http://www.indepthnrg.com/company-news/middle-east-and-africa/

[19] H. A. Khazdozian, "Improved design of permanent magnet generators for large scale wind turbines," Ph.D. dissertation, Iowa State University, 2016.

[20] Top ten turbine makers of 2017. [Online]. Available: https://www.windpowermonthly.com/article/1445638/top-ten-turbine-makers-2017

[21] Global wind market update 2016 - demand side analysis. [Online]. Available: https://fti-intelligencestore.com/index.php?route=download/main&download_id=151

[22] E. de Vries, "6 - wind turbine drive systems: a commercial overview," in *Electrical Drives for Direct Drive Renewable Energy Systems*, ser. Woodhead Publishing Series in Energy, M. Mueller, , and H. Polinder, Eds. Woodhead Publishing, 2013, pp. 139 – 157. [Online]. Available: https://www.sciencedirect.com/science/article/pii/B9781845697839500067

[23] T. Wang, F. Chu, and Q. Han, "Fault diagnosis for wind turbine planetary ring gear via a meshing resonance based filtering algorithm," *ISA Transactions*, vol. 67, no. Supplement C, pp. 173 – 182, 2017. [Online]. Available: http://www.sciencedirect.com/science/article/pii/S0019057816306814

[24] Powerful analysis of wind turbine gearboxes. [Online]. Available: http://www.powertransmissionworld.com/powerful-analysis-of-wind-turbine-gearboxes/

[25] Modular bearing system for planetary wind turbine gearboxes. [Online]. Available: http://www.nke.at/en/news-events/news-single/article/modularsystem-von-nke-fuer-planetenlager-in-getrieben-fuer-windenergieanlagen/

[26] R. Lateb, "Modélisation des machines asynchrones et synchrones a aimants avec prise en compte des harmoniques d'espace et de temps: application à la propulsion marine par pod," Ph.D. dissertation, Institut National Polytechnique de Lorraine-INPL, 2006.

[27] C. Belalahy, "Dimensionnement d'une machine synchro-réluctante à excitation homopolaire par réseaux de perméances," Ph.D. dissertation, Vandoeuvre-les-Nancy, INPL, 2008.

[28] G. Bywaters, V. John, J. Lynch, P. Mattila, G. Norton, J. Stowell, M. Salata, O. Labath, A. Chertok, and D. Hablanian, "Northern power systems windpact drive train alternative design study report," *National Renewable Energy Laboratory, Golden, CO, Report No. NREL/SR-500-35524*, 2004.

[29] E-126 wind turbine technical data. [Online]. Available: https://www.enercon.de/en/products/ep-8/e-126/

[30] Siemens d3 platform – 3.0-mw and 3.2-mw direct drive wind turbines. [Online]. Available: https://www.energy.siemens.com/br/pool/hq/power-generation/renewables/wind-power/platform%20brochures/D3%20Onshore%20brochure_ENGLISH_Apr2014_WEB.pdf

[31] Siemens industry presents new gearless direct drive wind generator. [Online]. Available: https://www.siemens.com/press/en/pressrelease/?press=/en/pressrelease/2012/industry/drive-technologies/idt2012094045.htm

[32] L. Soderlund, J. T. Eriksson, J. Salonen, H. Vihriala, and R. Perala, "A permanent-magnet generator for wind power applications," *IEEE Transactions on Magnetics*, vol. 32, no. 4, pp. 2389–2392, Jul 1996.

[33] E. Muljadi, C. P. Butterfield, and Y.-H. Wan, "Axial-flux modular permanent-magnet generator with a toroidal winding for wind-turbine applications," *IEEE Transactions on Industry Applications*, vol. 35, no. 4, pp. 831–836, Jul 1999.

[34] M. Dubois, H. Polinder, and J. Ferreira, "Comparison of generator topologies for direct-drive wind turbines," *Proceedings of NORPIE'00*, pp. 22–26, 2000.

[35] J. Legranger, "Contribution à l'étude des machines brushless à haut rendement dans les applications de moteurs-générateurs embarqués," Ph.D. dissertation, Compiègne, 2009.

[36] A. Daanoune, "Contribution à l'etude et à l'optimisation d'une machine synchrone à double excitation pour véhicules hybrides," Ph.D. dissertation, Université de Grenoble, 2012.

[37] P. Monjean, "Optimisation de l'architecture et des flux énergétiques de centrales à énergies renouvelables offshore et onshore équipées de liaisons en continu," Ph.D. dissertation, Arts et Métiers ParisTech, 2012.

[38] Components and services. [Online]. Available: https://en.partzsch.de/stator-windings

[39] Applications. [Online]. Available: https://www.hoganas.com/en/business-areas/soft-magnetic-composites/applications/

[40] fast curing metal adhesive for elevated temperatures. [Online]. Available: http://www.dpaonthenet.net/article/89096/A-fast-curing-metal-adhesive-for-elevated-temperatures.aspx

[41] H. Bali, "Etude des alternateurs à double excitation," Ph.D. dissertation, Ecole nationale supérieure polytechnique, 2011.

[42] Share of different turbine capacitys on the cumulative number of turbines. [Online]. Available: http://www.windmonitor.de/windmonitor_en/bilder_javascript.html?db_communicate=%27Windenergieeinspeisung.daten%27&p_lang=eng&img_id=433

[43] Gode wind 1 and 2 wind farm. [Online]. Available: http://www.4coffshore.com/windfarms/gode-wind-1-and-2-de-de13.html

[44] Dudgeon offshore wind farm. [Online]. Available: http://dudgeonoffshorewind.co.uk/about/facts-and-figures

[45] vejamate offshore wind farm. [Online]. Available: http://www.vejamate.net/#aboutus

[46] Bard offshore 1 wind farm. [Online]. Available: http://www.4coffshore.com/windfarms/bard-offshore-1-germany-de23.html

[47] Global tech 1 wind farm. [Online]. Available: http://www.4coffshore.com/windfarms/global-tech-i-germany-de09.html

[48] Adwen offshore. [Online]. Available: http://www.adwenoffshore.com/portfolio-item/alpha-ventus/

[49] Adwen offshore. [Online]. Available: http://www.adwenoffshore.com/portfolio-item/trianel-windpark-borkum/

[50] Adwen offshore. [Online]. Available: http://www.adwenoffshore.com/portfolio-item/wikinger/

[51] Nordseeone wind farm. [Online]. Available: http://www.nordseeone.com/engineering-construction/wind-turbines/general.html

[52] Thorntonbank wind farm. [Online]. Available: https://www.thewindpower.net/windfarm_fr_428_thorntonbank.php

[53] Seatitan 10mw wind turbine : technical specification. [Online]. Available: http://www.amsc.com/documents/seatitan-10-mw-wind-turbine-data-sheet/

[54] Haliade* 150-6mw offshore wind turbine. [Online]. Available: https://www.gerenewableenergy.com/wind-energy/turbines/offshore-turbine-haliade

[55] Swt-7.0-154 wind turbine : technical specification. [Online]. Available: https://www.siemens.com/content/dam/internet/siemens-com/global/market-specific-solutions/wind/data_sheets/data-sheet-wind-turbine-swt-7.0-154.pdf

[56] Siemens 6.0 mw offshore wind turbine. [Online]. Available: https://www.siemens.com/content/dam/webassetpool/mam/tag-siemens-com/smdb/wind-power-and-renewables/offshore-wind-power/documents/brochures/data-sheet-wind-turbine-swt-6-0-154-en.pdf

[57] 8 mw platform. [Online]. Available: http://www.adwenoffshore.com/products-services/products/8-mw-turbines/

[58] Ae 5.0-68. [Online]. Available: http://www.aerodyn.de/fileadmin/Media/Data_sheets/aerodyn_Energiesysteme_GmbH_data_sheet_ae5.0-68.0.pdf

[59] Leading edge technology, turbines & innovations. [Online]. Available: http://www.mhivestasoffshore.com/innovations/

[60] 6.x: technical data. [Online]. Available: https://www.senvion.com/senvion-france/fr/les-solutions-eoliennes/les-eoliennes/gamme-6xm/

[61] catalogo plataformas. [Online]. Available: http://www.siemensgamesa.com/recursos/doc/productos-servicios/aerogeneradores/nuevas-fichas/catalogo-plataformas-eng.pdf

[62] A. Boglietti, A. Cavagnino, D. Staton, M. Shanel, M. Mueller, and C. Mejuto, "Evolution and modern approaches for thermal analysis of electrical machines," *IEEE Transactions on industrial electronics*, vol. 56, no. 3, pp. 871–882, 2009.

[63] R. Lateb, N. Takorabet, and F. Meibody-Tabar, "Effect of magnet segmentation on the cogging torque in surface-mounted permanent-magnet motors," *IEEE Transactions on Magnetics*, vol. 42, no. 3, pp. 442–445, March 2006.

[64] J. Perho *et al.*, *Reluctance network for analysing induction machines*. Helsinki University of Technology, 2002.

[65] J. Sykulski, *Computational magnetics*. Springer Science & Business Media, 2012.

[66] C. J. Carpenter, "Magnetic equivalent circuits," *Electrical Engineers, Proceedings of the Institution of*, vol. 115, no. 10, pp. 1503–1511, October 1968.

[67] C. Chillet and J. Y. Voyant, "Design-oriented analytical study of a linear electromagnetic actuator by means of a reluctance network," *IEEE Transactions on Magnetics*, vol. 37, no. 4, pp. 3004–3011, Jul 2001.

[68] S. Ouagued, Y. Amara, and G. Barakat, "Cogging force analysis of linear permanent magnet machines using a hybrid analytical model," *IEEE Transactions on Magnetics*, vol. PP, no. 99, pp. 1–1, 2016.

[69] J. de Boeij, E. Lomonova, and A. Vandenput, "Modeling ironless permanent-magnet planar actuator structures," *IEEE Transactions on Magnetics*, vol. 42, no. 8, pp. 2009–2016, Aug 2006.

[70] K. J. Meessen, B. L. J. Gysen, J. J. H. Paulides, and E. A. Lomonova, "Halbach permanent magnet shape selection for slotless tubular actuators," *IEEE Transactions on Magnetics*, vol. 44, no. 11, pp. 4305–4308, Nov 2008.

[71] S. Williamson and C. I. McClay, "Optimisation of the geometry of closed rotor slots for cage induction motors," in *Industry Applications Conference, 1995. Thirtieth IAS Annual Meeting, IAS '95., Conference Record of the 1995 IEEE*, vol. 1, Oct 1995, pp. 507–514 vol.1.

[72] C. B. Rasmussen and E. Ritchie, "A magnetic equivalent circuit approach for predicting pm motor performance," in *Industry Applications Conference, 1997. Thirty-Second IAS Annual Meeting, IAS '97., Conference Record of the 1997 IEEE*, vol. 1, Oct 1997, pp. 10–17 vol.1.

[73] B. L. J. Gysen, E. Ilhan, K. J. Meessen, J. J. H. Paulides, and E. A. Lomonova, "Modeling of flux switching permanent magnet machines with fourier analysis," *IEEE Transactions on Magnetics*, vol. 46, no. 6, pp. 1499–1502, June 2010.

[74] S. Bazhar, J. Fontchastagner, N. Takorabet, and N. Labbe, "Hybrid analytical model coupling laplace x2019;s equation and reluctance network for electrical machines," *IEEE Transactions on Magnetics*, vol. 53, no. 6, pp. 1–4, June 2017.

[75] A. Mahyob, "Modélisation des machines électriques tournantes défectueuses par la méthode des réseaux de perméances : Application à la machine asynchrone," *Le Havre university*, 2009.

[76] B. Nedjar, "Modélisation basée sur la méthode des réseaux de perméances en vue de l'optimisation de machines synchrones à simple et à double excitation," Ph.D. dissertation, École normale supérieure de Cachan-ENS Cachan, 2011.

[77] S. Ouagued, A. Diriyé, Y. Amara, and G. Barakat, "Consideration of magnetic saturation in a new hybrid semi-numerical model," in *Proc. COMPUMAG*, 2015, pp. 1–2.

[78] M. Chiampi, D. Chiarabaglio, and M. Repetto, "An accurate investigation on numerical methods for nonlinear magnetic field problems," *Journal of magnetism and magnetic materials*, vol. 133, no. 1-3, pp. 591–595, 1994.

[79] G. Verez, "Contribution à l'étude des émissions vibro-acoustiques des machines électriques. cas des machines synchrones à aimants dans un contexte automobile." Ph.D. dissertation, Université du Havre; Normandie Université, France, 2014.

[80] G. C. Stone, "Advancements during the past quarter century in on-line monitoring of motor and generator winding insulation," *IEEE Transactions on Dielectrics and Electrical Insulation*, vol. 9, no. 5, pp. 746–751, Oct 2002.

[81] F. Magnussen, "On design and analysis of synchronous permanent magnet machines for field-weakening operation in hybrid electric vehicles," Ph.D. dissertation, Elektrotekniska system, 2004.

[82] G. Li, "Contribution à la conception des machines electriques à rotor passif pour des applications critiques: Modélisations electromagnétiques et thermiques sur cycle de fonctionnement, etude du fonctionnement en mode dégradé." Ph.D. dissertation, École normale supérieure de Cachan-ENS Cachan, 2011.

[83] A. Boglietti, A. Cavagnino, and D. Staton, "Determination of critical parameters in electrical machine thermal models," *IEEE Transactions on Industry Applications*, vol. 44, no. 4, pp. 1150–1159, 2008.

[84] S. Mezani, N. Takorabet, and B. Laporte, "A combined electromagnetic and thermal analysis of induction motors," *IEEE Transactions on Magnetics*, vol. 41, no. 5, pp. 1572–1575, May 2005.

[85] P. Romanazzi and D. A. Howey, "Air-gap convection in a switched reluctance machine," in *Ecological Vehicles and Renewable Energies (EVER), 2015 Tenth International Conference on*. IEEE, 2015, pp. 1–7.

[86] C. Gazley, "Heat transfer characteristics of the rotational and axial flow between concentric cylinders," *Trans. ASME*, vol. 80, no. 1, pp. 79–90, 1958.

[87] K. M. Becker and J. Kaye, *Measurement of diabatic flow in an annulus with an inner rotating cylinder*. MIT Research Laboratory of Heat Transfer in Electronics, 1960.

[88] I. Bjorklund and W. Kays, "Heat transfer between concentric rotating cylinders," *Journal of Heat Transfer*, vol. 80, pp. 79–90, 1959.

[89] M. Bouafia, Y. Bertin, J. Saulnier, and P. Ropert, "Analyse expérimentale des transferts de chaleur en espace annulaire étroit et rainuré avec cylindre intérieur tournant," *International journal of heat and mass transfer*, vol. 41, no. 10, pp. 1279–1291, 1998.

[90] G. I. Taylor, "Stability of a viscous liquid contained between two rotating cylinders," *Philosophical Transactions of the Royal Society of London. Series A, Containing Papers of a Mathematical or Physical Character*, vol. 223, pp. 289–343, 1923.

[91] D. Staton, A. Boglietti, and A. Cavagnino, "Solving the more difficult aspects of electric motor thermal analysis in small and medium size industrial induction motors," *IEEE Transactions on Energy Conversion*, vol. 20, no. 3, pp. 620–628, 2005.

[92] R. A. Matula, "Electrical resistivity of copper, gold, palladium, and silver," *Journal of Physical and Chemical Reference Data*, vol. 8, no. 4, pp. 1147–1298, 1979.

[93] H. Dogan, L. Garbuio, H. Nguyen-Xuan, B. Delinchant, A. Foggia, and F. Wurtz, "Multistatic reluctance network modeling for the design of permanent-magnet synchronous machines," *Magnetics, IEEE Transactions on*, vol. 49, no. 5, pp. 2347–2350, 2013.

[94] D. M. Araujo, J.-L. Coulomb, O. Chadebec, and L. Rondot, "A hybrid boundary element method-reluctance network method for open boundary 3-d nonlinear problems," *Magnetics, IEEE Transactions on*, vol. 50, no. 2, pp. 77–80, 2014.

[95] H. Nguyen-Xuan, H. Dogan, S. Perez, L. Gerbaud, L. Garbuio, and F. Wurtz, "Efficient reluctance network formulation for electrical machine design using optimization," *Magnetics, IEEE Transactions on*, vol. 50, no. 2, pp. 869–872, 2014.

[96] Q. Yu, X. Wang, and Y. Cheng, "Magnetic modeling of saliency effect for saturated electrical machines with a new calculation method."

[97] M. Jamil and X.-S. Yang, "A literature survey of benchmark functions for global optimisation problems," *International Journal of Mathematical Modelling and Numerical Optimisation*, vol. 4, no. 2, pp. 150–194, 2013.

[98] X. Yao and Y. Liu, "Fast evolutionary programming." *Evolutionary Programming*, vol. 3, pp. 451–460, 1996.

[99] M. J. D. Powell, "An efficient method for finding the minimum of a function of several variables without calculating derivatives," *The Computer Journal*, vol. 7, no. 2, pp. 155–162, 1964. [Online]. Available: +http://dx.doi.org/10.1093/comjnl/7.2.155

[100] H. Rosenbrock, "An automatic method for finding the greatest or least value of a function," *The Computer Journal*, vol. 3, no. 3, pp. 175–184, 1960.

[101] M. F. Møller, "A scaled conjugate gradient algorithm for fast supervised learning," *Neural Networks*, vol. 6, no. 4, pp. 525 – 533, 1993. [Online]. Available: http://www.sciencedirect.com/science/article/pii/S0893608005800565

[102] R. Eberhart and J. Kennedy, "A new optimizer using particle swarm theory," in *Micro Machine and Human Science, 1995. MHS'95., Proceedings of the Sixth International Symposium on.* IEEE, 1995, pp. 39–43.

[103] D. Wang, D. Tan, and L. Liu, "Particle swarm optimization algorithm: an overview," *Soft Computing*, pp. 1–22, 2017.

[104] Y. Shi and R. Eberhart, "A modified particle swarm optimizer," in *Evolutionary Computation Proceedings, 1998. IEEE World Congress on Computational Intelligence., The 1998 IEEE International Conference on.* IEEE, 1998, pp. 69–73.

[105] M. Clerc and J. Kennedy, "The particle swarm-explosion, stability, and convergence in a multidimensional complex space," *IEEE transactions on Evolutionary Computation*, vol. 6, no. 1, pp. 58–73, 2002.

[106] C. Darwin and G. Beer, *The origin of species.* Dent, 1951.

[107] D. Beasley, D. R. Bull, and R. R. Martin, "An overview of genetic algorithms: Part 1, fundamentals," *University computing*, vol. 15, no. 2, pp. 56–69, 1993.

[108] L. Davis, "Genetic algorithms and simulated annealing," 1987.

[109] J. J. Grefenstette, "Optimization of control parameters for genetic algorithms," *IEEE Transactions on systems, man, and cybernetics*, vol. 16, no. 1, pp. 122–128, 1986.

[110] L. Daviis, "Handbook of genetic algorithms," 1991.

[111] Z. Michalewicz, "Genetic algorithms+ data structures= evolution program," *Artificial Intelligence, Berlin: Springer, 1992*, 1992.

[112] D. E. Goldberg and K. Deb, "A comparative analysis of selection schemes used in genetic algorithms," *Foundations of genetic algorithms*, vol. 1, pp. 69–93, 1991.

[113] P. Ngatchou, A. Zarei, and A. El-Sharkawi, "Pareto multi objective optimization," in *Proceedings of the 13th International Conference on, Intelligent Systems Application to Power Systems*, Nov 2005, pp. 84–91.

[114] K. Deb, A. Pratap, S. Agarwal, and T. Meyarivan, "A fast and elitist multiobjective genetic algorithm: Nsga-ii," *IEEE Transactions on Evolutionary Computation*, vol. 6, no. 2, pp. 182–197, Apr 2002.

[115] N. Srinivas and K. Deb, "Muiltiobjective optimization using nondominated sorting in genetic algorithms," *Evolutionary Computation*, vol. 2, no. 3, pp. 221–248, Sept 1994.

[116] E. Zitzler, M. Laumanns, and L. Thiele, "Spea2: Improving the strength pareto evolutionary algorithm," 2001.

[117] E. Zitzler, "Evolutionary algorithms for multiobjective optimization: Methods and applications," 1999.

[118] S. Mostaghim and J. Teich, "Strategies for finding good local guides in multi-objective particle swarm optimization (mopso)," in *Swarm Intelligence Symposium, 2003. SIS'03. Proceedings of the 2003 IEEE.* IEEE, 2003, pp. 26–33.

[119] J. Alvarez-Benitez, R. Everson, and J. Fieldsend, "A mopso algorithm based exclusively on pareto dominance concepts," in *Evolutionary Multi-Criterion Optimization.* Springer, 2005, pp. 459–473.

[120] M. J. D. Powell, "Algorithms for nonlinear constraints that use lagrangian functions," *Mathematical Programming*, vol. 14, no. 1, pp. 224–248, Dec 1978. [Online]. Available: https://doi.org/10.1007/BF01588967

[121] D. P. Bertsekas, *Nonlinear programming.* Athena scientific Belmont, 1999.

[122] X. Wang, H. Polinder, D. Lahaye, and J. A. Ferreira, "Fe based multi-objective optimization of a 3.2mw brushless doubly-fed induction machine," in *2017 IEEE Workshop on Electrical Machines Design, Control and Diagnosis (WEMDCD)*, April 2017, pp. 89–94.

[123] X. Wang, T. D. Strous, D. Lahaye, H. Polinder, and J. A. Ferreira, "Modeling and optimization of brushless doubly-fed induction machines using computationally efficient finite-element analysis," *IEEE Transactions on Industry Applications*, vol. 52, no. 6, pp. 4525–4534, Nov 2016.

[124] A. Daghigh, H. Javadi, and H. Torkaman, "Design optimization of direct-coupled ironless axial flux permanent magnet synchronous wind generator with low cost and high annual energy yield," *IEEE Transactions on Magnetics*, vol. 52, no. 9, pp. 1–11, Sept 2016.

[125] P. Akiki, M. Hage-Hassan, P. Dessante, J. C. Vannier, M. Bensetti, D. Prieto, and M. McClelland, "Multi-physics modeling and optimization of a multi-v-shape ipm with concentrated winding," in *2017 IEEE International Electric Machines and Drives Conference (IEMDC)*, May 2017, pp. 1–7.

[126] M. Desvaux, B. Multon, H. B. Ahmed, S. Sire, A. Fasquelle, and D. Laloy, "Gear ratio optimization of a full magnetic indirect drive chain for wind turbine applications," in *2017 Twelfth International Conference on Ecological Vehicles and Renewable Energies (EVER)*, April 2017, pp. 1–9.

[127] X. Jannot, J. C. Vannier, C. Marchand, M. Gabsi, J. Saint-Michel, and D. Sadarnac, "Multiphysic modeling of a high-speed interior permanent-magnet synchronous machine for a multiobjective optimal design," *IEEE Transactions on Energy Conversion*, vol. 26, no. 2, pp. 457–467, June 2011.

[128] H. Li, Z. Chen, and H. Polinder, "Optimization of multibrid permanent-magnet wind generator systems," *IEEE Transactions on Energy Conversion*, vol. 24, no. 1, pp. 82–92, March 2009.

[129] A. Grauers, "Design of direct-driven permanent-magnet generators for wind turbines," Ph.D. dissertation, Chalmers University of Technology, 1996.

[130] Find pareto front of multiple fitness functions using genetic algorithm. [Online]. Available: https://fr.mathworks.com/help/gads/gamultiobj.html#inputarg_options

[131] P. Tchakoua, R. Wamkeue, M. Ouhrouche, F. Slaoui-Hasnaoui, T. A. Tameghe, and G. Ekemb, "Wind turbine condition monitoring: State-of-the-art review, new trends, and future challenges," *Energies*, vol. 7, no. 4, pp. 2595–2630, 2014. [Online]. Available: http://www.mdpi.com/1996-1073/7/4/2595

[132] F. Spinato, P. J. Tavner, G. Van Bussel, and E. Koutoulakos, "Reliability of wind turbine subassemblies," *IET Renewable Power Generation*, vol. 3, no. 4, pp. 387–401, 2009.

[133] D. Chan and J. Mo, "Life cycle reliability and maintenance analyses of wind turbines," *Energy Procedia*, vol. 110, no. Supplement C, pp. 328 – 333, 2017, 1st International Conference on Energy and Power, ICEP2016, 14-16 December 2016, RMIT University, Melbourne, Australia. [Online]. Available: http://www.sciencedirect.com/science/article/pii/S1876610217301789

[134] M. Sepulveda, J. Shek, P. R. Thies, E. Oterkus, P. Davies, and M. Spring, "Physics-based gearbox failure model for multi-mw offshore wind turbines," in *ASME 2017 36th International Conference on Ocean, Offshore and Arctic Engineering*. American Society of Mechanical Engineers, 2017, pp. V03BT02A011–V03BT02A011.

[135] P. Tavner, "Offshore wind turbines: Reliability," *Availability and Maintenance, The Institution of Engineering and Technology, London, UK*, 2012.

[136] W. Musial, S. Butterfield, and B. McNiff, "Improving wind turbine gearbox reliability," in *European Wind Energy Conference, Milan, Italy*, 2007, pp. 7–10.

[137] A. Ragheb and M. Ragheb, "Wind turbine gearbox technologies," in *2010 1st International Nuclear Renewable Energy Conference (INREC)*, March 2010, pp. 1–8.

[138] Adwen and winergy present the world's biggest wind turbine gearbox. [Online]. Available: http://www.adwenoffshore.com/adwen-and-winergy-present-the-worlds-biggest-wind-turbine-gearbox/

[139] wind-turbine-models website. [Online]. Available: https://en.wind-turbine-models.com

[140] F. Oyague, "Gearbox modeling and load simulation of a baseline 750-kw wind turbine using state-of-the-art simulation codes," National Renewable Energy Laboratory (NREL), Golden, CO., Tech. Rep., 2009.

[141] Y. Feng, Y. Qiu, C. J. Crabtree, H. Long, and P. J. Tavner, "Monitoring wind turbine gearboxes," *Wind Energy*, vol. 16, no. 5, pp. 728–740, 2013.

[142] B. Lu, Y. Li, X. Wu, and Z. Yang, "A review of recent advances in wind turbine condition monitoring and fault diagnosis," in *2009 IEEE Power Electronics and Machines in Wind Applications*, June 2009, pp. 1–7.

[143] C. Armstrong, "Power-transmitting device." Nov. 26 1901, uS Patent 687,292. [Online]. Available: https://www.google.com/patents/US687292

[144] K. Atallah and D. Howe, "A novel high-performance magnetic gear," *IEEE Transactions on Magnetics*, vol. 37, no. 4, pp. 2844–2846, Jul 2001.

[145] K. Atallah, S. D. Calverley, and D. Howe, "Design, analysis and realisation of a high-performance magnetic gear," *IEE Proceedings - Electric Power Applications*, vol. 151, no. 2, pp. 135–143, Mar 2004.

[146] S. Gerber, "Evaluation and design aspects of magnetic gears and magnetically geared electrical machines," Ph.D. dissertation, Stellenbosch: Stellenbosch University, 2015.

[147] N. W. Frank and H. A. Toliyat, "Analysis of the concentric planetary magnetic gear with strengthened stator and interior permanent magnet (ipm) inner rotor," in *2010 IEEE Energy Conversion Congress and Exposition*, Sept 2010, pp. 2977–2984.

[148] K. K. Uppalapati, W. Bomela, J. Z. Bird, M. Calvin, and J. Wright, "Construction of a low speed flux focusing magnetic gear," in *2013 IEEE Energy Conversion Congress and Exposition*, Sept 2013, pp. 2178–2184.

[149] P. O. Rasmussen, T. O. Andersen, F. T. Joergensen, and O. Nielsen, "Development of a high performance magnetic gear," in *38th IAS Annual Meeting on Conference Record of the Industry Applications Conference, 2003.*, vol. 3, Oct 2003, pp. 1696–1702 vol.3.

[150] A. Bensalah, "Conception d'aérogénérateurs et hydrogénérateurs à concentration de flux sans aimants terres rare," Ph.D. dissertation, Le Havre, 2020.

Abstract

The aim of this PhD report is the investigation of electrical generators dedicated to an offshore wind turbine application. The main goal is to find optimal solutions in a vast research domain containing between eight and eleven optimization variables, while respecting a the imposed constraints. In order to achieve this goal, a multi-physics model was developed allowing the determination of the electromagnetic and temperature fields distributions in the selected topologies. Lumped models coupled to the interpolation functions were chosen as a solution offering a good computation time / precision ratio, thus taking into consideration the characteristics of the materials (thermal and magnetic). The developed model was coupled to a genetic optimization algorithm, NSGAII, allowing at first; the investigation of the necessary permanent magnets weight and the active parts one of two permanent magnet synchronous generator topologies where in the first the magnets are mounted in surfaces and in the second inserted in order to have flux concentration, three different powers have been investigated 5, 8 and 15 [MW]. Second, the integration of a magnetic gear in the wind energy conversion chain was studied using the same optimal approach previously used, while comparing the weight required of permanent magnets for this type of training with that of direct drive topologies (without gearbox).

Keywords: Reluctance network – Lumped thermal model – Optimization – Electrical machines – Magnetic gearbox – Offshore wind turbine.

Résumé

Ce mémoire de thèse constitue une contribution à l'investigation des génératrices destinées à une application éolienne en mer. Le but est de rechercher les solutions optimales dans un domaine de recherche vaste contenant entre huit et onze variables d'optimisation, tout en respectant un cahier de charge bien précis. Afin d'y parvenir, un modèle multi-physique a été développé permettant la détermination des distributions du champ électromagnétique et de température dans les topologies de génératrices choisies avec prise en considération des non-linéarités des matériaux. La méthode des constantes localisées couplée aux fonctions d'interpolations a été choisie comme solution offrant un bon rapport temps de calculs/précision, prenant ainsi en considération les caractéristiques des matériaux (thermiques et magnétiques). Le modèle développé a été couplé à un algorithme d'optimisation génétique, NSGAII, permettant dans un premier temps ; d'investiguer le poids nécessaire des aimants permanents et des parties actives de deux topologies de génératrices synchrones à aimant permanent où dans la première les aimants sont montés en surfaces et dans la seconde insérés en concentration de flux, trois puissances différentes ont été investiguées 5, 8 et 15 [MW]. Dans un second temps, l'intégration d'un multiplicateur de vitesse magnétique dans la chaîne de conversion éolienne a été étudiée à travers la même approche optimale utilisée précédemment tout en comparant le poids nécessaires des aimants permanents pour ce type d'entrainement avec celle des topologies à attaque directe (sans multiplicateur de vitesse).

Mots clés : Réseaux de reluctances - Réseaux de conductances thermique - Optimisation - Génératrice éolienne – Multiplicateur de vitesse magnétique- Dimensionnement - Constantes localisées.